

DIRECT MEASUREMENT OF THE
HYPERFINE TRANSITION OF POSITRONIUM
USING HIGH POWER SUB-THZ RADIATION

PH. D. THESIS

Takayuki Yamazaki

Department of Physics
Faculty of Science, University of Tokyo

December 2011

Abstract

This thesis reports the first measurement of the direct hyperfine transition of the ground state of positronium using high power sub-THz radiation. We developed a new optical system to accumulate sub-THz radiation of 11 kW (peak intensity of $I = 8.3 \times 10^7$ W/m², peak energy density of $\epsilon = 0.28$ J/m³) in a Fabry-Pérot resonant cavity and to cause hyperfine transition of the ground state of positronium. We have observed clear transition signals at 5.4σ level after 4.3 days of on-resonance data taking. The transition probability is consistent with the QED calculation and no excess was observed in off-resonance data.

Contents

1	Introduction	1
1.1	Motivation	1
1.2	Properties of Positronium	3
1.3	Hyperfine Structure of the Ground State of Positronium	4
1.4	Previous Measurements of Ps-HFS	6
1.5	Hyperfine Transition of the Ground State of Positronium	8
2	Experiment	15
2.1	Method of Our Experiment	15
2.2	Optical System	15
2.2.1	Gyrotron	16
2.2.2	Mode Converter	22
2.2.3	Fabry-Pérot Resonant Cavity	31
2.2.4	Power Estimation	39
2.2.5	Stabilization	44
2.3	Positronium Assembly and γ -ray Detectors	48
2.3.1	Positronium Formation Assembly	49
2.3.2	Characteristics of Mixed Gas	51
2.3.3	γ -ray Detectors	53
2.4	Electronics and Data Acquisition	54
2.5	Monte Carlo Simulation	58
3	Analysis	65
3.1	Data Sets	65
3.2	Calibration and Basic Cut	66
3.2.1	Energy Spectrum of the Plastic Scintillator	67
3.2.2	Energy Spectrum of the LaBr ₃ (Ce) Scintillator	67
3.2.3	Time Walk Correction of the LaBr ₃ (Ce) Scintillator	68
3.2.4	Time Walk Correction of the Plastic Scintillator	69
3.2.5	Offline Trigger Cuts	69
3.3	Event Selection	72
3.3.1	Signatures of the Transition Signal	74
3.3.2	Background	74

3.3.3	Delayed Coincidence	75
3.3.4	Accidental Rejection	76
3.3.5	γ -ray Energy Cut	76
3.4	Systematic Errors	78
3.4.1	Energy Scale and Energy Resolution	78
3.4.2	Ps Formation Probability and Pick-off Annihilation Probability	80
3.4.3	Accidental Rejection Efficiency	80
3.4.4	Background Normalization	82
3.4.5	Summary of the Systematic Errors	82
3.5	Result	82
4	Discussion	85
4.1	Various Checks	85
4.1.1	Accidental Rejection	85
4.1.2	Energy Selection	85
4.1.3	Time Spectrum of the Transition Signal	86
4.2	Comparison with QED Calculation	86
4.3	Future Prospect	87
5	Conclusion	95
	Acknowledgements	97

List of Figures

1.1	Historical plot of the Ps-HFS value.	2
1.2	The decay modes of Ps.	4
1.3	Feynman diagram of positronium.	5
1.4	Zeeman splitting of Ps.	7
1.5	Plot of the X -electron coupling constant which can explain the Ps-HFS discrepancy vs. mass of X	8
1.6	Level diagram of the hyperfine structure of positronium	9
1.7	Lineshape functions without Doppler broadening (black) and with Doppler broadening of 7 % (red).	11
1.8	Fraction of 2γ decays per o-Ps vs. radiation intensity.	12
2.1	A schematic of a gyrotron.	17
2.2	A schematic of an annular electron beam.	19
2.3	A picture of the Gyrotron FU CW V.	20
2.4	(left) TE_{03} mode, (right) TE_{02} mode.	21
2.5	Space distribution of the gyrotron output (TE_{03} mode).	22
2.6	A Gaussian beam.	23
2.7	The schematic view and the picture of the mode converter.	24
2.8	Cross-sectional view of the step-cut waveguide and the Vlasov mirror	25
2.9	Side view of the step-cut waveguide and the Vlasov mirror	26
2.10	Calculated intensity distributions at various distances from the Vlasov mirror	28
2.11	Measured intensity distributions at various distances from the Vlasov mirror	29
2.12	Polarization of the converted beam.	30
2.13	Beam shape after the mode converter.	30
2.14	A schematic of a Fabry-Pérot resonant cavity.	32
2.15	Basic performance of Fabry-Pérot resonant cavity (calculation).	34
2.16	The beam shape in the Fabry-Pérot cavity.	35
2.17	Pictures of the gold mesh mirror.	36
2.18	The reflectance (black) and the transmittance (red) of the Au plain mesh mirror simulated using CST MICROWAVE STUDIO.	37
2.19	Principal of operation of an SIDM TM (Smooth Impact Drive Mechanism) actuator.	38

2.20	Structural drawing of the X-axis stage and its controller.	38
2.21	Pyroelectric detectors (Spectrum Detector Inc. SPH-49).	39
2.22	The accumulated power (left) and the reflected power (right) of the Fabry-Pérot resonant cavity measured while changing cavity length.	40
2.23	Temperature of water measured while the water is exposed to the Gaussian beam during 120 s.	41
2.24	The transmitted power of the Cu concave mirror V_{tr} normalized by the input beam power V_{in} while changing the cavity length L by $\lambda/2$	42
2.25	A picture of the PVC sheet taken by IR camera to estimate P_{hole}/P_{in}	43
2.26	Schematic diagram of the feedback stabilization system.	45
2.27	Time variation of the gyrotron output power.	46
2.28	Stabilization of the input beam power by controlling heater AC voltage.	47
2.29	Schematic of the rescan procedure.	47
2.30	Control of the cavity length to keep resonance of the Fabry-Pérot cavity.	48
2.31	A schematic and a picture of the positronium assembly chamber and γ -ray detectors	49
2.32	A schematic of the positronium formation assembly	50
2.33	The decay scheme of the ^{22}Na isotope	50
2.34	The lifetime of the slow positron as a function of the partial pressure of isobutane.	52
2.35	Absorption of sub-THz radiation by isobutane.	53
2.36	Four γ -ray detectors are arranged to make four back-to-back pairs.	54
2.37	The schematic view of the whole DAQ system.	55
2.38	Schematic diagram of electronics for plastic scintillator system.	57
2.39	Schematic diagram of electronics for γ -ray detector system.	59
2.40	Schematic diagram of electronics for trigger system.	60
2.41	Geometry of the Monte Carlo simulation.	63
3.1	The timing diagram of the gyrotron output.	66
3.2	Plastic scintillator energy with long-gate vs that with short-gate	67
3.3	Energy spectrum of one of the $\text{LaBr}_3(\text{Ce})$ scintillators (la-0)	68
3.4	The left and the right figure show the scatter plot of timing vs energy deposited on one of the $\text{LaBr}_3(\text{Ce})$ scintillators (la-0) before and after time walk correction, respectively.	69
3.5	The left and the right figure show the scatter plot of timing vs energy deposited on the plastic scintillator before and after time walk correction, respectively.	70
3.6	ps-1 energy (short-gate) vs. ps-0 energy (short-gate)	71
3.7	Time difference between the ps-1 signal and the ps-0 signal	72
3.8	Time difference between the back-to-back signals from the $\text{LaBr}_3(\text{Ce})$ scintillators.	73
3.9	Time difference between the plastic scintillator and the coincidence signal of the $\text{LaBr}_3(\text{Ce})$ scintillators.	75

3.10	Time chart of the normal event (upper) and the accidental event (lower).	77
3.11	Energy difference between long-gate and short-gate of the ps-0 signal.	77
3.12	Time spectrum before and after accidental rejection.	78
3.13	Energy spectrum of on-resonance data (RUN I) when the delayed coincidence and the accidental rejection are applied and a 511 keV γ ray is observed at the opposite side of the LaBr ₃ (Ce) scintillator.	79
3.14	The difference of the slow positron annihilation rate.	81
3.15	The difference of the Ps formation probabilities.	81
3.16	The fraction of the transition signals vs. the accumulated power in the Fabry-Pérot resonant cavity.	83
4.1	Fitted time spectrum of the transition signals.	87
4.2	The fraction of the transition signals is consistent with QED calculation.	88
4.3	Fitted decay rate (RUN I).	89
4.4	A picture of a melted mesh mirror.	90
4.5	Interference between input power and reflected power around resonance peak.	90
4.6	A schematic of a grating ring cavity.	91
4.7	Transition curve assuming $I = 10^8$ W/m ²	92
4.8	Simulation of Ps-HFS measurement assuming statistical accuracy of 10 % and power accuracy of 10 %.	92
4.9	A schematic of an experimental setup with a slow positron beam.	93

List of Tables

1.1	The classification of Ps according to its quantum numbers.	3
2.1	Parameters and operational conditions of Gyrotron FU CW V	19
2.2	Operating modes of Gyrotron FU CW V	19
2.3	Parameters of the step-cut waveguide and the Vlasov mirror	27
2.4	Properties of NE-102 (plastic) scintillator.	50
2.5	Properties of the PMT (HAMAMATSU R5924-70).	51
2.6	Properties of LaBr ₃ (Ce) scintillator	54
2.7	Quantities recorded at the main trigger timing.	61
2.8	Quantities recorded in synchronization with the gyrotron output pulse.	61
3.1	Properties of the RUNs	66
3.2	Energy resolutions of the LaBr ₃ (Ce) scintillators	68
3.3	Summary of the event rates until the offline trigger cut.	73
3.4	Event rates after the delayed coincidence.	76
3.5	Event rates after the accidental rejection.	76
3.6	The positions and the widths of the 511 keV peaks of “beam ON” events and “beam OFF” events.	80
3.7	Summary of the systematic errors.	82
3.8	Results of the four RUNs.	83
4.1	Check dependency on the upper limit of the accidental rejection cut.	85
4.2	Check dependency on the lower limit of the energy selection.	86

Chapter 1

Introduction

This thesis reports the first measurement of the hyperfine transition of the ground state of positronium using high power sub-THz radiation. In the first section, we describe the physics motivation of this experiment at the beginning. Next, we introduce the properties of positronium. Then the theory and the previous measurements of the hyperfine structure of the ground state of positronium are summarized. Finally, the hyperfine transition of the ground state of positronium are described.

1.1 Motivation

Positronium (Ps), a bound state of an electron and a positron, is a purely leptonic system and is a good target to study Quantum Electrodynamics (QED). The triplet (1^3S_1) state of Ps is called ortho-positronium (o-Ps) and mainly decays into three γ rays with long lifetime of 142 ns. On the other hand, the singlet (1^1S_0) state of Ps is called para-positronium (p-Ps) and mainly decays into two γ rays promptly (lifetime is 125 ps). The energy level of the ground state o-Ps is higher than that of the ground state p-Ps because of the spin-spin interaction. The difference is called the hyperfine structure of the ground state of positronium (Ps-HFS). The Ps-HFS is significantly large (about 203 GHz) compared to the hyperfine structure of the hydrogen atom (about 1.4 GHz).

Precise measurement of Ps-HFS gives the direct information on QED, especially in the bound state. The precise measurements have been performed in 1970's and 1980's, whose results are shown in Fig. 1.1 with the theoretical value. All previous measurements of the Ps-HFS employed static magnetic field (about 1 T) and the Ps-HFS has been measured indirectly using Zeeman splitting (about 3 GHz). These results are consistent with each other, and the combined value of the most accurate two results [1, 2] is 203.388 65(67) GHz (3.3 ppm). This combined value is shown with the green band.

New method to calculate the higher order corrections up to $O(\alpha^3 \log \alpha^{-1})$ for the bound state is established in 2000 [3]. The QED prediction is 203.391 69(41)

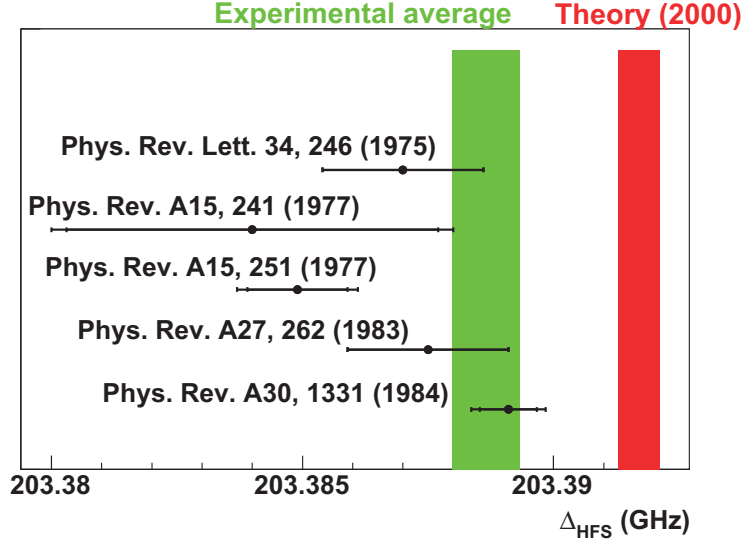


Figure 1.1: Historical plot of the Ps-HFS value. Points with error bars show the experimental results with references. The green and red bands show the average of the measured values (the average of the latest two results) and the theoretical calculation up to $O(\alpha^3 \log \alpha^{-1})$, respectively.

GHz (2 ppm) shown with the red band. There is a large discrepancy (3.9σ , 15 ppm) between the measured and the theoretical value. It is very important to measure the Ps-HFS again with a method totally different from the previous experiments since non-uniformity of the static magnetic field is the most significant systematic error in the previous experiments.

Direct measurement of the Ps-HFS is free from systematic uncertainty of the static magnetic field, which is one of the possible common uncertainties in the previous experiments. The direct measurement has never been performed because the rate of spontaneous emission (or Einstein's A coefficient $A = 3.37 \times 10^{-8} [\text{s}^{-1}]$) is 14 orders of magnitude smaller than the decay rate of o-Ps ($\lambda_{\text{o-Ps}} = 7.0401(7) \times 10^6 [\text{s}^{-1}]$ [4]). High power sub-THz radiation is necessary to cause enough stimulated emission but there was no high power radiation source so far, therefore even the hyperfine transition itself has not yet been observed. However, the recent development of the gyrotron, which is a novel high power radiation source for sub-THz to THz region, changes the situation. Its output is monochromatic, the power is high (100 W - 1 kW), and it can operate in continuous wave (CW) or long pulse wave. Although the direct output power of the gyrotron is not enough high to cause sufficient amount of the hyperfine transition of the ground state of Ps, we can achieve it (~ 10 kW) by accumulating the output radiation in an optical resonator (Fabry-Pérot resonant cavity). The first target of our experiment is to observe the hyperfine transition for the first time using the new optical system,

which is described in this thesis.

1.2 Properties of Positronium

Positronium (Ps), the bound state of an electron (e^-) and a positron (e^+), is the lightest hydrogen-like atom bound by the electromagnetic interaction. Since Ps is a purely leptonic system and effectively free from hadronic and weak interaction effects, precise measurements of decay rate and energy levels give us direct information on bound state QED.

Positronium consists of two fermions as hydrogen atom, and its wave functions are classified according to the principal quantum number n , a sum of the orbital angular momentum l and the spin angular momentum s , and its projection on a quantization axis m . Basically, the energy levels of positronium are given by

$$E_n = -\frac{m_e c^2 \alpha^2}{4n^2}, \quad (1.1)$$

where m_e is the electron mass, c is the speed of light, and $\alpha = e^2/(4\pi\epsilon_0\hbar c)$ is the fine structure constant. The fine structure due to the spin-orbit interaction and the hyperfine structure due to the spin-spin interaction make shifts from the above equation. $E_0 = -6.8$ eV and there is no fine structure in the case of the ground state ($n = 1$) because the orbital angular momentum $l = 0$. However, the energy level of the ground state is split by the total spin s of positronium, which is called hyperfine structure. The detail of the hyperfine structure is described in the next section. The singlet state with antiparallel spins (total spin $s = 0$, its projection $m = 0$) is called para-positronium (p-Ps), and the triplet state with parallel spins ($s = 1$, $m = 0, \pm 1$) is called ortho-positronium (o-Ps).

name	total spin s	projection m	C	P	decay mode	lifetime
p-Ps	0	0	+	-	2γ (, 4γ , 6γ , ...)	125 ps
o-Ps	1	$0, \pm 1$	-	-	3γ (, 5γ , 7γ , ...)	142 ns

Table 1.1: The classification of Ps according to its quantum numbers.

A fermion-antifermion system with orbital angular momentum l and spin angular momentum s has a C -parity of $(-1)^{l+s}$ under a charge-conjugation transformation and a parity (P) of $(-1)^{l+1}$. Thus o-Ps and p-Ps have odd and even C parities respectively. Due to the C -invariance of the electromagnetic interaction, this difference plays a crucial role on the decay modes. In fact, o-Ps decays only into odd γ 's and p-Ps decays only into even γ 's since the system consisting of n photons has a C parity of $(-1)^n$. In addition, single photon decay in vacuum is prohibited by energy-momentum conservation. Then, the decay modes of o-Ps and p-Ps are as follows.

$$o - \text{Ps} \rightarrow n\gamma, \quad n = 3, 5, 7, 9, \dots \quad (1.2)$$

$$p - \text{Ps} \rightarrow n\gamma, \quad n = 2, 4, 6, 8, \dots \quad (1.3)$$

As a number of photons increases, the width of the decay mode decreases by a factor of α . Furthermore, phase space of the final state is getting smaller as the number of the final state photons increases. Thus, decay modes into many photons are highly suppressed. As a result, p-Ps mainly decays into two γ rays and o-Ps mainly decays into three γ rays. The Feynman diagrams of 2γ decay of p-Ps and 3γ decay of o-Ps are shown in Fig. 1.2. The experimental values of the decay rate of p-Ps and o-Ps are

$$\lambda_{p-\text{Ps}} = 7.990\ 9(17) \times 10^9 \text{ s}^{-1} [5], \quad (1.4)$$

$$\lambda_{o-\text{Ps}} = 7.040\ 1(7) \times 10^6 \text{ s}^{-1} [4]. \quad (1.5)$$

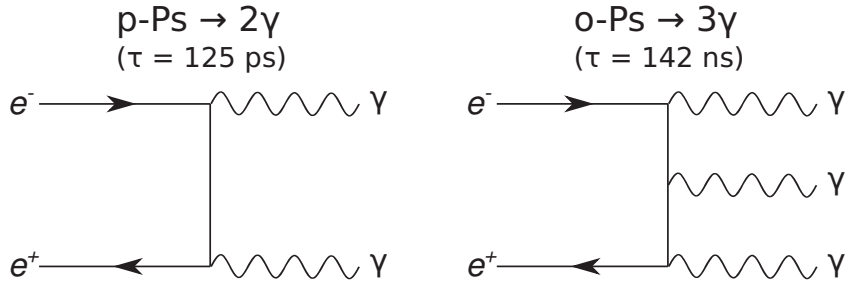


Figure 1.2: The decay modes of Ps.

1.3 Hyperfine Structure of the Ground State of Positronium

Since positronium is a particle-antiparticle system, not only scattering process (t -channel) but also annihilation process (s -channel) contribute to the energy levels as shown in Fig. 1.3. The total Hamiltonian for positronium to $O(1/c^2)$ is expressed

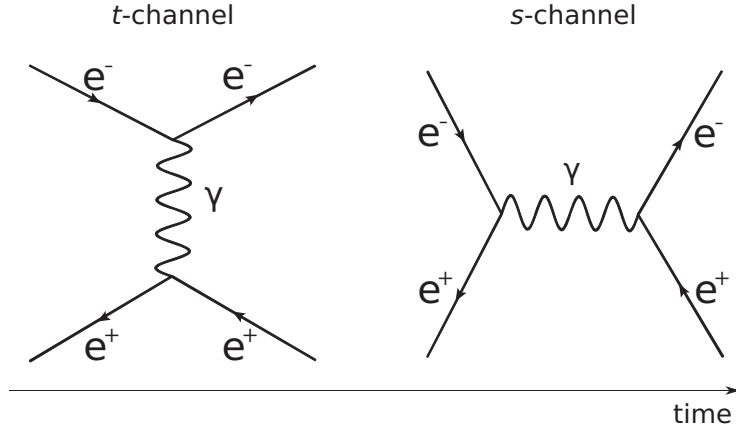


Figure 1.3: Feynman diagram of positronium. The left diagram is scattering process (t -channel) and the right diagram shows annihilation process (s -channel)

as

$$\mathcal{H} = \frac{\mathbf{p}^2}{m_e} - \frac{e^2}{4\pi\epsilon_0 r} + V_1 + V_2 + V_3 + V_4 \quad (1.6)$$

$$V_1 = -\frac{\mathbf{p}^4}{4m_e^3 c^2} + \frac{\mu_B^2}{\epsilon_0 c^2} \delta(\mathbf{r}) - \frac{e^2}{8\pi\epsilon_0 m_e^2 c^2 r} \left[\mathbf{p}^2 + \frac{\mathbf{r} \cdot (\mathbf{r} \cdot \mathbf{p}) \mathbf{p}}{r^2} \right] \quad (1.7)$$

$$V_2 = \frac{3\mu_B^2}{2\pi\epsilon_0 c^2} \frac{\mathbf{l} \cdot \mathbf{s}}{r^3} \quad (1.8)$$

$$V_3 = \frac{3\mu_B^2}{2\pi\epsilon_0 c^2} \left[\frac{(\mathbf{s} \cdot \mathbf{r})(\mathbf{s} \cdot \mathbf{r})}{r^5} - \frac{\mathbf{s}^2}{3r^3} \right] + \frac{\mu_B^2}{\epsilon_0 c^2} \left(\frac{4}{3} \mathbf{s}^2 - 2 \right) \delta(\mathbf{r}) \quad (1.9)$$

$$V_4 = \frac{\mu_B^2}{\epsilon_0 c^2} \mathbf{s}^2 \delta(\mathbf{r}), \quad (1.10)$$

where $\mu_B = e\hbar/(2m_e)$ is the Bohr magneton, ϵ_0 is the vacuum permittivity. V_1 is orbital correction terms. V_2 is the spin-orbit interaction, which causes fine structure splitting. V_3 and V_4 are the spin-spin interactions of t -channel and s -channel, respectively. The spin-spin interaction causes hyperfine structure splitting.

Now we consider the ground state ($n = 1, l = 0$) of positronium. There is no fine structure since the orbital angular momentum l is zero. The energy difference between the energies of the ground states of o-Ps and p-Ps (Ps-HFS) derives from V_3 and V_4 . In the lowest order of α , Ps-HFS is

$$\Delta_0^{\text{th}} = \frac{1}{3} m_e c^2 \alpha^4 + \frac{1}{4} m_e c^2 \alpha^4 = \frac{7}{12} m_e c^2 \alpha^4 \quad (1.11)$$

$$= 0.85 \text{ meV} = 204 \text{ GHz}. \quad (1.12)$$

The first term is the t -channel contribution and the second term is the s -channel contribution.

Higher order contribution is calculated in the framework of dimensionally regularized nonrelativistic QED.

$$\Delta^{\text{th}} = \Delta_0^{\text{th}} \left\{ 1 - \frac{\alpha}{\pi} \left(\frac{32}{21} + \frac{6}{7} \ln 2 \right) + \frac{5}{14} \alpha^2 \ln \frac{1}{\alpha} \right. \quad (1.13)$$

$$\left. + \left(\frac{\alpha}{\pi} \right)^2 \left[\frac{1367}{378} - \frac{5197}{2016} \pi^2 + \left(\frac{6}{7} + \frac{221}{84} \pi^2 \right) \ln 2 - \frac{159}{56} \zeta(3) \right] \right. \\ \left. - \frac{3}{2} \frac{\alpha^3}{\pi} \ln^2 \frac{1}{\alpha} + \left(\frac{62}{15} - \frac{68}{7} \ln 2 \right) \frac{\alpha^3}{\pi} \ln \frac{1}{\alpha} + \dots \right\} \\ = 203.391\ 69(41)\ \text{GHz} [3]. \quad (1.14)$$

1.4 Previous Measurements of Ps-HFS

Ps-HFS has been measured precisely in 1970's and 1980's as shown in Fig. 1.1, but all of the previous measurements are indirect measurements using Zeeman effect, because it was impossible to prepare high power (~ 10 kW) sub-THz radiation to cause direct hyperfine transition at that time.

In a static magnetic field, the o-Ps state with $m = 0$ and the p-Ps state mix, and the resultant states have different energies (Zeeman effect) as shown in Fig. 1.4. On the other hand, the o-Ps states with $m = \pm 1$ are not affected at all. The mixture depends on the strength of the static magnetic field, and the energy difference between the perturbed o-Ps state ($|+\rangle$) and the unperturbed o-Ps states ($|1, +1\rangle$, $|1, -1\rangle$) is related to the Ps-HFS by the following equation,

$$\Delta_{\text{mix}} = \frac{\Delta_{\text{HFS}}}{2} \left(\sqrt{1 + x^2} - 1 \right) \quad (1.15)$$

$$x = \frac{2g'\mu_B B}{h\Delta_{\text{HFS}}}, \quad (1.16)$$

where g' is the bound state electron g -factor in Ps, B is the strength of the static magnetic field, and h is the Planck constant. Therefore Δ_{HFS} can be obtained from Δ_{mix} and B . Δ_{mix} becomes about 3 GHz when we apply a static magnetic field of about 1 T.

In the previous experiment, the strong static magnetic field was produced by a resistive electromagnet and the microwave of about 500 W was produced by a magnetron [1] and a klystron [2]. Zeeman transition from the unperturbed o-Ps states ($|1, +1\rangle$, $|1, -1\rangle$) to the perturbed o-Ps state ($|+\rangle$) occurs when the microwave frequency matches Δ_{mix} . The number of the 2γ decays increases on resonance since the $|+\rangle$ state mainly decays into 2γ rays. The transition curve is obtained by measuring the increase of 2γ decays while changing the strength of the static magnetic field whereas the microwave frequency is fixed. The combined value of the most precise two independent experiments [1, 2] is

$$\Delta^{\text{exp.}} = 203.388\ 65(67)\ \text{GHz}. \quad (1.17)$$

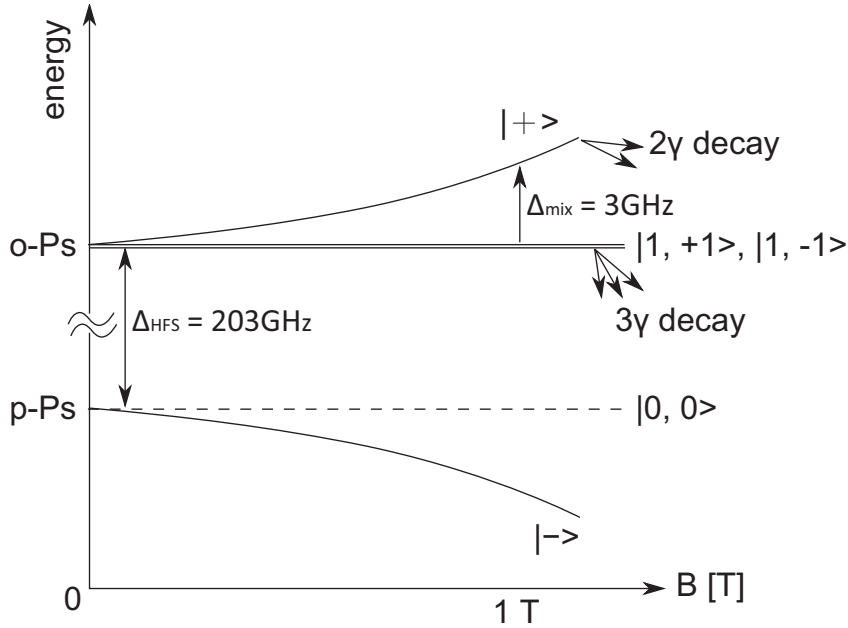


Figure 1.4: All previous measurements of the Ps-HFS employed static magnetic field (about 1T) and the Ps-HFS has been measured indirectly using Zeeman splitting (about 3GHz).

There is a 3.9σ (15ppm) discrepancy between the experimental value and the theoretical calculation. Verification of the discrepancy with a different method is necessary. Possible reasons of the discrepancy are as follows:

1. common systematic error in the previous experiments (e.g. non-uniformity of the static magnetic field, slow thermalization of Ps)
2. new physics beyond the Standard Model
3. miscalculation of the theoretical value

The non-uniformity of the static magnetic field is the most significant systematic error in the previous experiments. It is difficult to prepare uniform magnetic field in the region where Ps is formed, whereas the uncertainty of the magnetic field strength contributes to the Ps-HFS directly by Eq. (1.15). The other possible common systematic uncertainty is the unthermalized Ps contribution, which is indicated in [6, 7]. The previous experiments used all positroniums although the Ps thermalization process is slow and the contribution from unthermalized o-Ps gives rise to an underestimation of the material effect, therefore the extrapolation to Ps-HFS in vacuum can be wrong.

On the other hand, if the discrepancy is real, it indicates the existence of an unknown particle [8]. Assume that there exists a neutral particle X whose mass is m_X and the coupling constant between X and electron is g_{Xee} . Figure 1.5 shows

a plot of g_{Xee} vs. m_X which can explain the discrepancy between the measured and the theoretical value of Ps-HFS. Excluded regions from positronium decay [9], reactor axion [10], electron beam dump [11, 12, 13], and electron g-2 [14, 15, 16] are also shown. If the discrepancy between the measured and the theoretical value of Ps-HFS is real, it indicates the existence of a pseudoscalar, a vector, or an axial vector particle with a mass of ~ 1 MeV or an axial vector particle with a mass of < 1 keV.

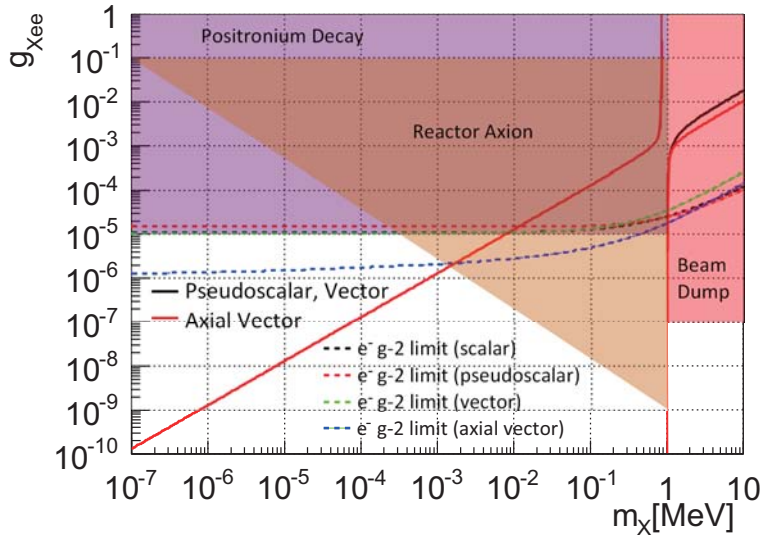


Figure 1.5: Plot of the X -electron coupling constant which can explain the Ps-HFS discrepancy vs. mass of X . The black line shows the case that X is a pseudoscalar or a vector particle. The red line corresponds to an axial vector particle. Excluded regions from positronium decay [9], reactor axion [10], electron beam dump [11, 12, 13], and electron g-2 [14, 15, 16] are also shown.

1.5 Hyperfine Transition of the Ground State of Positronium

Figure 1.6 is a level diagram for the hyperfine transition of the ground state of positronium with a linearly polarized radiation of energy density $\rho(\omega)$ per unit angular frequency. Only $|1,0\rangle$ and $|0,0\rangle$ states are affected by the linearly polarized radiation, which has a spin $|1,0\rangle$, due to the conservation law of the angular momentum. If we denote the population of $|i,j\rangle$ state of Ps as $N_{i,j}$, then the

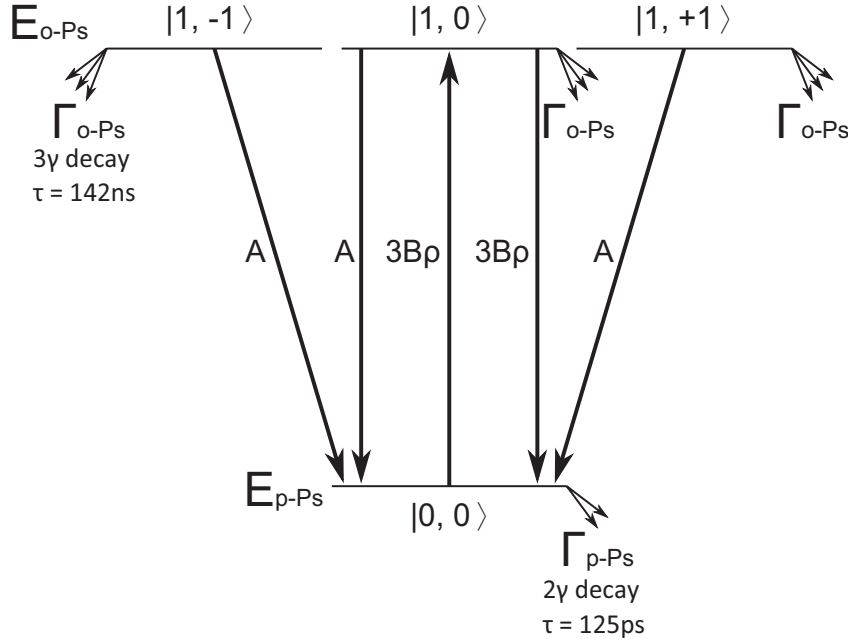


Figure 1.6: Level diagram of the hyperfine structure of positronium

rate equations for the hyperfine transition of the ground state of positronium are expressed as

$$\begin{aligned} \frac{dN_{0,0}(\omega, t)}{dt} &= -3B(\omega)\rho(\omega)N_{0,0}(\omega, t) + 3B(\omega)\rho(\omega)N_{1,0}(\omega, t) \\ &\quad + A(N_{1,0}(\omega, t) + N_{1,+1}(t) + N_{1,-1}(t)) - \lambda_{p-Ps}N_{0,0}(\omega, t) \end{aligned} \quad (1.18)$$

$$\begin{aligned} \frac{dN_{1,0}(\omega, t)}{dt} &= 3B(\omega)\rho(\omega)N_{0,0}(\omega, t) - 3B(\omega)\rho(\omega)N_{1,0}(\omega, t) \\ &\quad - AN_{1,0}(\omega, t) - \lambda_{o-Ps}N_{1,0}(\omega, t) \end{aligned} \quad (1.19)$$

$$\frac{dN_{1,+1}(t)}{dt} = -AN_{1,+1}(t) - \lambda_{o-Ps}N_{1,+1}(t) \quad (1.20)$$

$$\frac{dN_{1,-1}(t)}{dt} = -AN_{1,-1}(t) - \lambda_{o-Ps}N_{1,-1}(t). \quad (1.21)$$

where A and $B(\omega)$ are the Einstein's coefficients of Ps-HFS. A is the spontaneous emission rate of Ps-HFS. The reason of the pre-factor 3 in the term of $3B(\omega)\rho(\omega)$ is as follows. The Einstein's coefficients are defined in the case of unpolarized radiation where the absorption and the stimulated emission occur in all substates of o-Ps ($|1, -1\rangle$, $|1, 0\rangle$, and $|1, +1\rangle$) with equal rate of $B(\omega)\rho(\omega)$. In the case, the energy density in one space direction is 1/3 of the total energy density of the unpolarized beam. On the other hand, the energy density of the linearly polarized radiation in the polarization direction is the same as the total energy density of the radiation.

The hyperfine transition of the ground state of Ps is $M1$ transition since $E1$ transition is forbidden since the parity of o-Ps and p-Ps is the same, therefore the transition probability is about α^2 times smaller than $E1$ transition. $E2$ transition is about $(\Delta_{\text{HFS}}/E_0)^2$ times smaller than $M1$ transition, which is negligible in the case of the hyperfine transition of the ground state of Ps. Therefore, the transition probability can be expressed as

$$A = \frac{\omega^3}{3\pi\epsilon_0\hbar c^5} |\boldsymbol{\mu}|^2 = \frac{g^2 \hbar^2 \omega^3 \alpha}{3m_e^2 c^4} = 3.37 \times 10^{-8} \text{ s}^{-1}, \quad (1.22)$$

where $\boldsymbol{\mu}$ is the magnetic dipole moment of the electron of positronium, which is twice as large as that of hydrogen atom since the reduced mass of the electron of positronium is $m_e/2$. $B(\omega)$ is related to A by the following equation,

$$B(\omega) = A \frac{\pi^2 c^3}{\hbar \omega^3} g(\omega), \quad (1.23)$$

where $g(\omega)$ is the lineshape function which satisfies

$$\int g(\omega) d\omega = 1. \quad (1.24)$$

The spectrum lineshape is never strictly monochromatic because the states of Ps have finite lifetimes. The finite lifetimes lead to a Lorentzian lineshape expressed as

$$g_n(\omega) = \frac{1}{\pi} \frac{\Delta\omega_n/2}{(\omega - \omega_0)^2 + (\Delta\omega_n/2)^2}, \quad (1.25)$$

where $\Delta\omega_n$ is the natural linewidth (FWHM) because of the finite lifetimes of the states of Ps, and

$$\Delta\omega_n = A + \lambda_{\text{p-Ps}} + \lambda_{\text{o-Ps}} \quad (1.26)$$

In the above equation, the decay rate of p-Ps is dominant and the natural linewidth is 1.3 GHz in frequency. The effect of so-called pressure broadening can be included in the above equation by replacing the decay rates of Ps in vacuum with those in gas.

In addition, the Doppler broadening also affects the lineshape. The normalized Gaussian lineshape function due to the Doppler broadening is

$$g_{\text{D}}(\omega) = \frac{c}{\omega_0} \sqrt{\frac{m}{2\pi k_{\text{B}} T}} \exp\left(-\frac{mc^2(\omega - \omega_0)^2}{2k_{\text{B}} T \omega_0^2}\right) \quad (1.27)$$

and the FWHM of the Doppler broadening is

$$\Delta\omega_{\text{D}} = 2\omega_0 \sqrt{\frac{(2 \ln 2) k_{\text{B}} T}{mc^2}} \quad (1.28)$$

where m is the positronium mass, k_{B} is the Boltzmann constant and T is its temperature. T is the same as room temperature (about 300 K) after positronium is fully thermalized. Then the width of the Doppler broadening is about 0.08 GHz.

The lineshape function $g(\omega)$ in the Einstein's B coefficient $B(\omega)$ is the convolution of $g_n(\omega)$ and $g_D(\omega)$ (Voigt function). Figure 1.7 shows the lineshape functions with and without Doppler broadening. In the case of this measurement, the effect of the Doppler broadening is small as shown in red line.

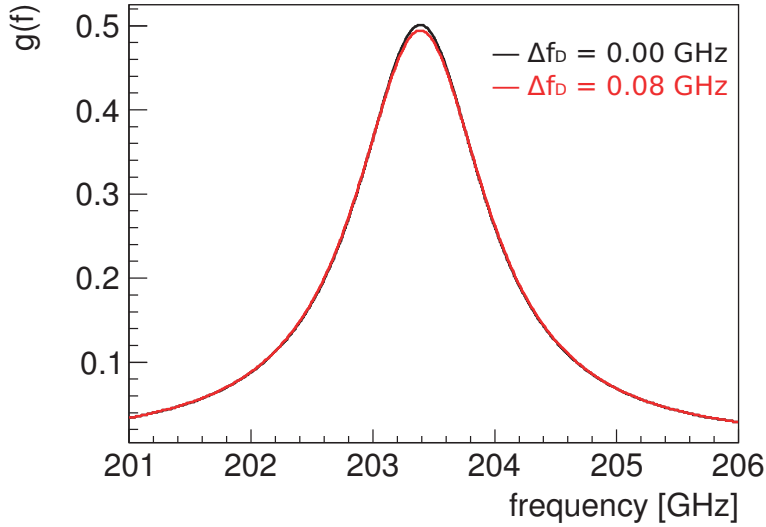


Figure 1.7: Lineshape functions without Doppler broadening (black) and with Doppler broadening of 7 % (red). Pressure broadening is assumed to be 5 %.

$N_{0,0}(\omega, t)$, $N_{1,0}(\omega, t)$, $N_{1,+1}(t)$, and $N_{1,-1}(t)$ are obtained by providing appropriate initial conditions. In the case of unpolarized positroniums the conditions are $N_{0,0}(\omega, 0) = N_{1,0}(\omega, 0) = N_{1,+1}(0) = N_{1,-1}(0) = N_0/4$, where N_0 is the populations of all positroniums at $t = 0$.

Extremely high power radiation is necessary to cause enough stimulated emission to observe the hyperfine transition of the ground state of positronium because the decay rate of the upper state (o-Ps) is 10^{14} times larger than the rate of the spontaneous emission. Figure 1.8 shows fraction of 2γ decays per o-Ps versus radiation intensity. The fraction is zero without radiation but increases as the radiation intensity arises, and when $I > 10^8$ W/m², the fraction becomes larger than 10 %. Finally, the fraction is saturated at 1/3 because only $|1, 0\rangle$ state of o-Ps can interact with linearly polarized radiation, whose spin is $|1, 0\rangle$. $I = 10^8$ W/m² can be achieved if 10 kW power is concentrated on 10 mm \times 10 mm cross-section. This intensity is the most important requirement of this experiment.

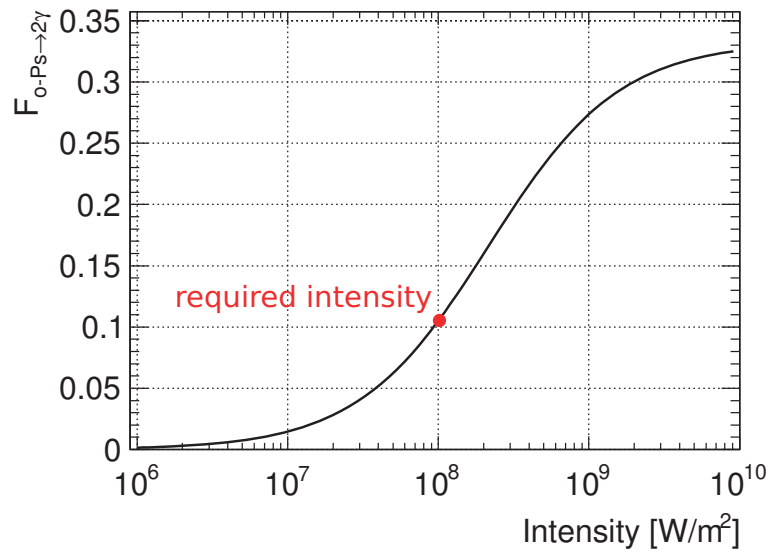


Figure 1.8: Fraction of 2γ decays per o-Ps increases as the radiation intensity arises and is saturated at $1/3$ due to the conservation law of the angular momentum. Red point shows required radiation intensity of this experiment.

This thesis is organized as follows. Chapter 2 describes the experimental apparatus in detail. The calibration and the analysis of the measured data is described in Chapter 3. The systematic errors and the result of the measurement are shown there. In Chapter 4, the result is checked and compared to the QED expectation. Finally, we conclude this thesis in Chapter 5.

Chapter 2

Experiment

2.1 Method of Our Experiment

The method of this experiment is as follows:

1. Gyrotron radiates sub-THz radiation, whose stable power is about 300 W. (→2.2.1)
2. The gyrotron output (TE_{03} mode) is converted to a Gaussian beam. (→2.2.2)
3. The Gaussian beam is accumulated in a Fabry-Pérot resonant cavity and the accumulated power is about 10 kW. (→2.2.3)
4. Positroniums are formed inside the Fabry-Pérot resonant cavity and o-Ps transits to p-Ps (hyperfine transition). (→2.3)
5. Para-positroniums increase due to the transition and decay into two γ rays. The γ rays are detected by γ -ray detectors and the increase of the 2γ decays are measured. (→2.3)

2.2 Optical System

The optical system is composed of three devices. In this section, details of the following devices are explained.

1. Gyrotron as a sub-THz radiation source
2. Mode converter to convert gyrotron output into Gaussian beam
3. Fabry-Pérot resonant cavity to accumulate sub-THz radiation

2.2.1 Gyrotron

Our target frequency is 203 GHz, in other words, the wavelength is 1.5 mm. There are BWO (Backward Wave Oscillator), FEL (Free Electron Laser), and gyrotron as a radiation source in this frequency region. BWO is frequency-tunable in a wide range, but its output power is very low (1 - 100mW). In the case of FEL, the average power is high (100 W - 1 kW), however, the apparatus is very large, its output is restricted to very short pulse ($< 1 \mu s$), and its linewidth is very wide (0.1 - 1 %). On the other hand, gyrotron can produce high power radiation (100 W - 1kW) and can operate in CW or long pulse wave and its size is reasonable. In addition, the linewidth of its output wave is very narrow (< 100 ppm). Therefore we use a gyrotron as a radiation source.

Theory of gyrotron

Gyrotron is an electron cyclotron maser. Figure 2.1 is a cross-sectional view of a gyrotron. An electron gun, a resonant cavity, and a collector are in vacuum.

At the electron gun, its cathode is heated and thermal electrons are emitted. There is an anode in the wall around the cathode and it pulls the electrons in a transverse direction. The electrons are cylindrically-distributed.

The electrons go toward the resonant cavity while accelerated by the potential difference and rotating around a magnetic line created by the superconducting magnet and the gun coil. The frequency of the cyclotron motion in the resonant cavity is

$$\omega_c = \frac{eB}{m_e\gamma} = \frac{\Omega_0}{\gamma}, \quad (2.1)$$

where e is the electron charge, B is a magnetic field strength in the resonant cavity, m_e is the electron mass, and $\gamma = 1/\sqrt{1 - (v/c)^2}$ (v is a velocity of the electron) is a Lorentz factor of an electron.

Let's consider the phase bunching process of electrons in a reference frame in which the axial velocity of electrons becomes zero. The radius of the cycrotron motion of electron is $r = v_t\gamma/\Omega_0 \ll R$, where v_t is the transverse velocity of electron. The transverse electric field (TE_{mn} mode) of the cavity of the gyrotron accelerates or decelerates the electrons. If the phase of the electrons is random, the energy exchange between the electrons and the electric field of the cavity is zero in total.

Phase bunching as shown in Fig. 2.2 occurs only when the frequency of the electric field in the resonant cavity becomes slightly larger than the initial frequency of the cyclotron motion of electrons, which is determined by the strength of the magnetic field. Then the electron 2 shown in the left side of Fig. 2.2 is accelerated, and gains energy while its cyclotron frequency decreases because its Lorentz factor γ increases. Thus the electron 2 goes out of resonance and therefore the energy gain on each cycle becomes less and less. On the other hand, the electron 1 is decelerated and loses energy while its cyclotron frequency increases until it reaches

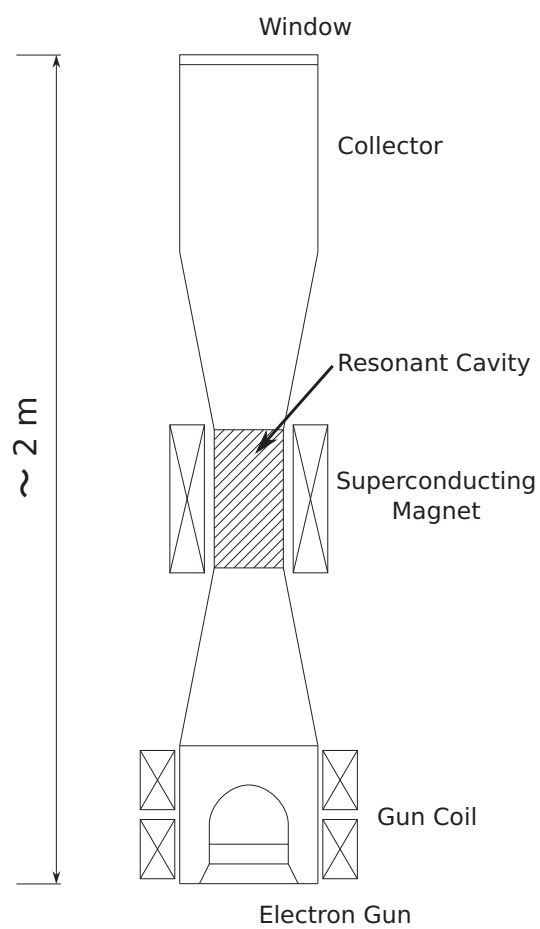


Figure 2.1: A schematic of a gyrotron.

the frequency of the electric field. Therefore, the energy loss of the electron 1 increases more and more. As a result, the energy exchange between the electrons and the electric field becomes maximum and the phase bunching occurs.

On the contrary, if the initial gyrotron frequency is larger than the frequency of the electric field of the cavity, the electron 2 approaches the resonance and gains energy more and more, and the electron 1 goes out of resonance and loses energy less and less. Consequently, the energy exchange between the electrons and the electric field becomes minimum.

The resonant cavity is a circular waveguide and the wave mode which interacts with the electrons is TE_{mn} mode, which has no electric field parallel to the axial direction ($E_z = 0$) and is expressed as

$$E_r(z) = iA \frac{m\omega\mu}{(j'_{mn}/R)^2 r} J'_m \left(\frac{j'_{mn}}{R} r \right) \sin(m\phi) e^{-i\zeta_{mn}z} \quad (2.2)$$

$$E_\phi(z) = iA \frac{\omega\mu}{(j'_{mn}/R)^2} J'_m \left(\frac{j'_{mn}}{R} r \right) \cos(m\phi) e^{-i\zeta_{mn}z} \quad (2.3)$$

$$E_z(z) = 0 \quad (2.4)$$

$$H_r(z) = -iA \frac{\zeta_{mn}}{(j'_{mn}/R)^2} J'_m \left(\frac{j'_{mn}}{R} r \right) \cos(m\phi) e^{-i\zeta_{mn}z} \quad (2.5)$$

$$H_\phi(z) = iA \frac{m\zeta_{mn}}{(j'_{mn}/R)^2 r} J'_m \left(\frac{j'_{mn}}{R} r \right) \sin(m\phi) e^{-i\zeta_{mn}z} \quad (2.6)$$

$$H_z(z) = AJ_m \left(\frac{j'_{mn}}{R} r \right) \cos(m\phi) e^{-i\zeta_{mn}z} \quad (2.7)$$

where $J_m(x)$ is the m -th Bessel function, $J'_m(x)$ is its 1st derivative, j'_{mn} is the n -th root of $J'_m(0) = 0$ and

$$\zeta_{mn} = \sqrt{\left(\frac{\omega}{c}\right)^2 - \left(\frac{j'_{mn}}{R}\right)^2} \quad (2.8)$$

The resonance condition is $\zeta_{mn} = l\pi/L$ ($l = 0, 1, 2, \dots$), where L is the cavity length. The resonant frequency of the circular cavity resonator of the gyrotron is

$$\omega_{mn,l} = c \sqrt{\left(\frac{j'_{mn}}{R}\right)^2 + \left(\frac{l\pi}{L}\right)^2}. \quad (2.9)$$

Gyrotron FU CW V

We develop a gyrotron named ‘‘Gyrotron FU CW V’’ (Fig. 2.3). Its parameters and operational conditions are summarized in Table 2.1. The peak power and frequency of its operating modes are summarized in Table 2.2.

The frequencies are measured with a synthesizer as a reference. The sub-THz radiation of frequency f and the reference RF radiation of frequency f_{RF} are fed

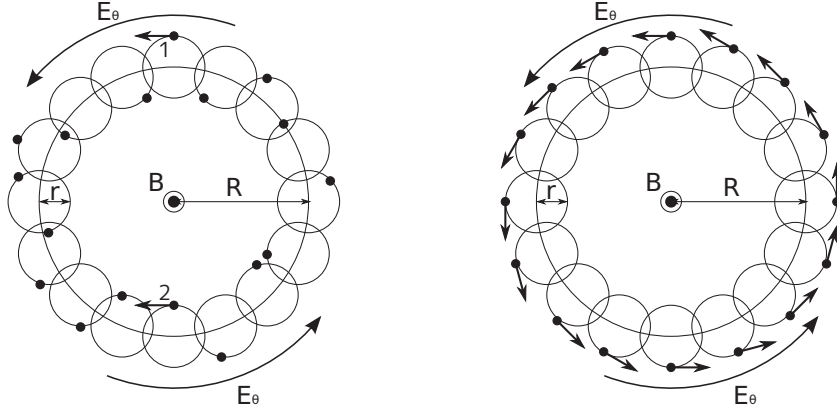


Figure 2.2: A schematic of an annular electron beam. The left figure shows initial random phasing of electrons. The right figure shows electrons bunched in phase.

cavity radius	2.39 mm
cavity length	14 mm
Q value of the cavity	1300
Cathode voltage	-18 kV
Anode voltage	-12 kV
Beam current	300~400 mA
Repetition rate	5 Hz
Duty ratio	30 %

Table 2.1: Parameters and operational conditions of Gyrotron FU CW V

mode (m, n)	B [T]	f_{meas} [GHz]	f_{calc} [GHz]	P [W]	eff. [%]
0, 1	2.793	-	68.36	314	4.4
1, 2	3.887	106.47	107.00	270	3.8
2, 2	4.870	134.00	134.45	704	9.8
0, 2	5.110	140.06	140.62	515	7.2
3, 2	5.840	159.95	160.54	314	4.4
1, 3	6.208	-	170.91	722	10.0
4, 2	6.729	185.21	185.67	597	8.3
2, 3	7.238	198.83	199.43	635	8.8
0, 3	7.364	202.89	203.42	695	9.7

Table 2.2: Operating modes of Gyrotron FU CW V



Figure 2.3: A picture of the Gyrotron FU CW V.

to a Schottky barrier diode, and its output radiation of frequency $|f - nf_{\text{RF}}|$ is measured with a spectrum analyzer through low pass filter. In the case of TE_{03} mode, the linewidth of the gyrotron output is about 1 MHz (5 ppm) but its center value varies by about 2 MHz (10 ppm) within a pulse (width = 15 ms). The measured frequencies are uniformly smaller than the calculation despite the wave mode. The difference can be explained if the radius is 12 μm larger than the design value due to the manufacturing accuracy or transformation during assembly or aging.

Power is estimated from the calorie deposited on water. All of the output radiation is absorbed by water and its power is estimated from the temperature increase. The absorption coefficient of water for sub-THz radiation is very large (about 10^2 cm^{-1} [17]). The peak power is about 700 W at maximum as shown in Fig. 2.2, but the stable peak power is down to only about 300 W.

We perform hyperfine transition measurements at off- and on-resonance frequencies for comparison. We use the TE_{03} mode ($f = 202.89 \text{ GHz}$) for on-resonance measurement and TE_{02} mode for off-resonance measurement. We select TE_{02} mode though there are modes whose frequency is nearer resonance, because the mode converter described in the following subsection works well only in TE_{0n} mode. TE_{0n} mode has no electric field in r -direction and is rotationally symmetric around z -axis. Its space distribution looks n concentric circle as shown in Fig. 2.4

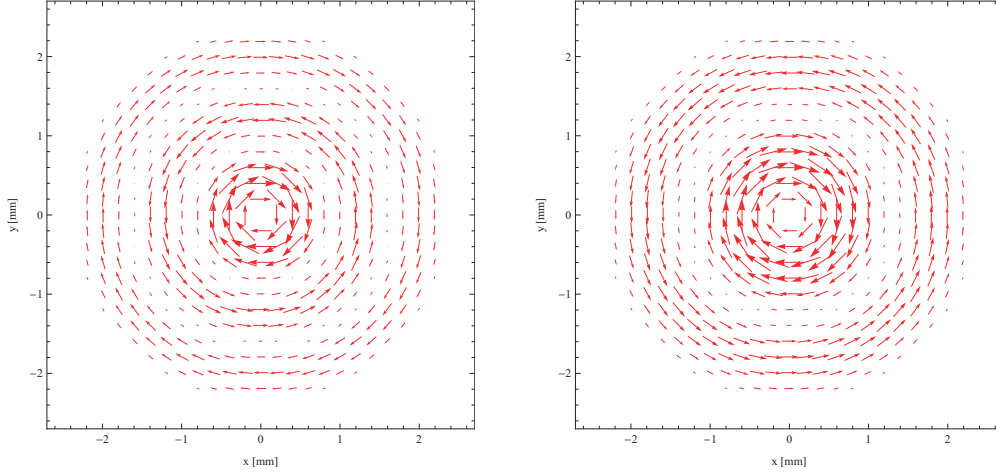


Figure 2.4: (left) TE_{03} mode, (right) TE_{02} mode.

Figure 2.5 is space distribution of the gyrotron output (TE_{03} mode) measured at 360 mm from the window. The pattern is obtained by taking an infrared picture of PVC (PolyVinyl Chloride) sheet (thickness = 1 mm) over the window. PVC is a good absorber of sub-THz radiation among solid and easily obtainable materials, whose absorption coefficient is about 1 cm^{-1} [18]. The reason of the asymmetric pattern is not clear, but a port near the window to evacuate the air is a possible reason.

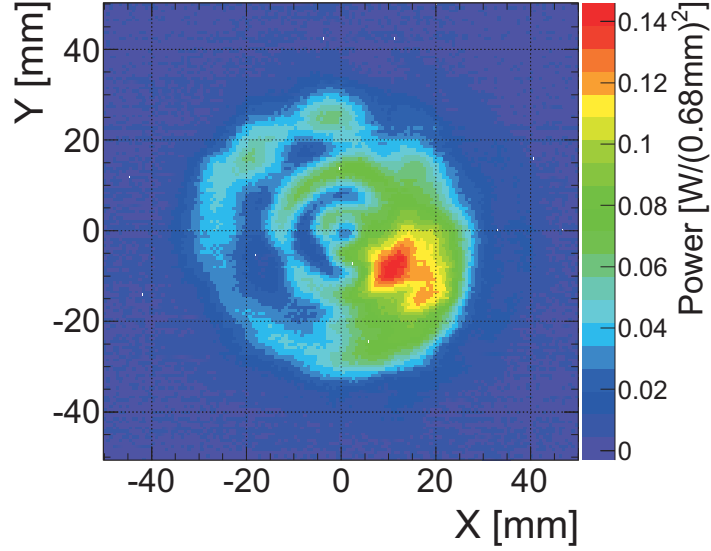


Figure 2.5: Space distribution of the gyrotron output (TE_{03} mode).

2.2.2 Mode Converter

Gyrotron FU CW V operates in TE_{03} (or TE_{02}) mode and its stable peak power is about 300 W. The power is high but not enough to observe the hyperfine transition of Ps. The radiation will be accumulated in the Fabry-Pérot resonant cavity but the wave mode of the Fabry-Pérot resonant cavity is Gaussian beam (Eq. (2.10)), which is completely different from TE_{0n} mode. If we define the polarization direction of the Gaussian beam as x -axis, the electric field is expressed as

$$E_x(r, z) = E_0 \frac{w_0}{w(z)} \exp \left[- \left(\frac{r}{w(z)} \right)^2 - i \left(kz - \tan^{-1} \frac{\lambda z}{\pi w_0^2} + \frac{kr^2}{2R(z)} \right) \right] \quad (2.10)$$

where

$$w(z) = w_0 \sqrt{1 + \left(\frac{\lambda z}{\pi w_0^2} \right)^2} \quad (2.11)$$

$$R(z) = z \left[1 + \left(\frac{\pi w_0^2}{\lambda z} \right)^2 \right]. \quad (2.12)$$

Figure 2.6 shows the shape of a Gaussian beam. The beam size $w(z)$ is shown in a red line.

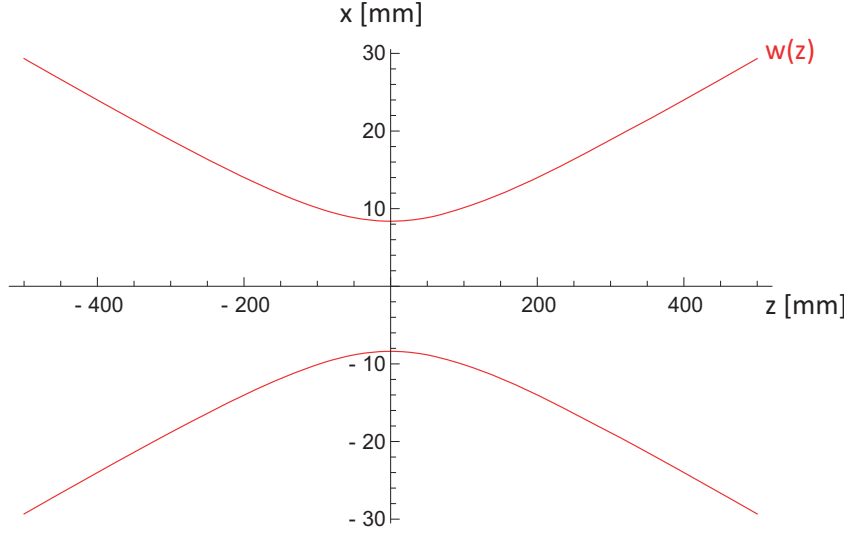


Figure 2.6: A Gaussian beam. Beam parameters are $w_0 = 8.39$ mm and $\lambda = 1.48$ mm.

Consequently, the output of the gyrotron can not be coupled with the Fabry-Pérot resonant cavity. The matching ratio η is expressed as

$$\eta = \frac{\left| \int E_{\text{beam}}^* E_{\text{FP}} dS \right|}{\sqrt{\int |E_{\text{beam}}|^2 dS \int |E_{\text{FP}}|^2 dS}} \quad (2.13)$$

and the scalar product in the numerator becomes zero since the electric field of TE_{0n} mode is only in the ϕ direction but the Gaussian beam is linearly polarized. Therefore, the gyrotron output must be converted to a Gaussian beam.

Design of the mode converter

Figure 2.7 is a schematic and a picture of the mode converter. Its main component is the step-cut waveguide made of copper and the Vlasov mirror, which is a large parabolic mirror made of aluminum. It converts the TE_{0n} mode to plain wave (or bi-Gaussian beam) geometrically by matching the center of the step-cut waveguide and the focus point of the Vlasov mirror (Fig. 2.8). This is because the parabola is expressed as

$$y = \frac{x^2}{4f} - f \quad (2.14)$$

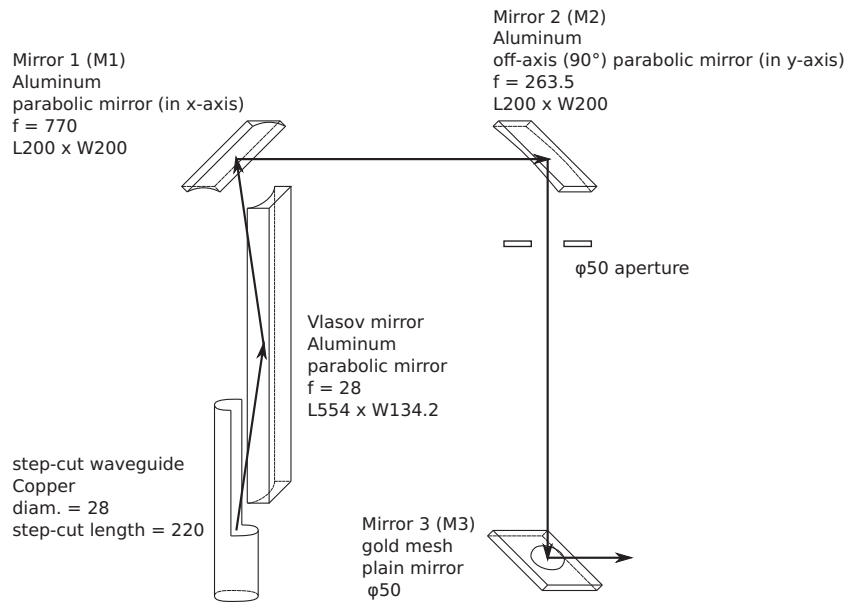


Figure 2.7: The schematic and the picture of the mode converter.

and the path length L from the center of the waveguide to the wavefront at $y = C$ is

$$L = \sqrt{x'^2 + y'^2} + C - y' = \sqrt{4f(y' + f) + y'^2} + C - y' \quad (2.15)$$

$$= \sqrt{(y' + 2f)^2} + C - y' = 2f + C = \text{const.} \quad (2.16)$$

when the light is reflected at (x', y') . The following two mirrors (M1 and M2) shape the bi-Gaussian beam into a Gaussian beam and the aperture cuts the sidelobes.

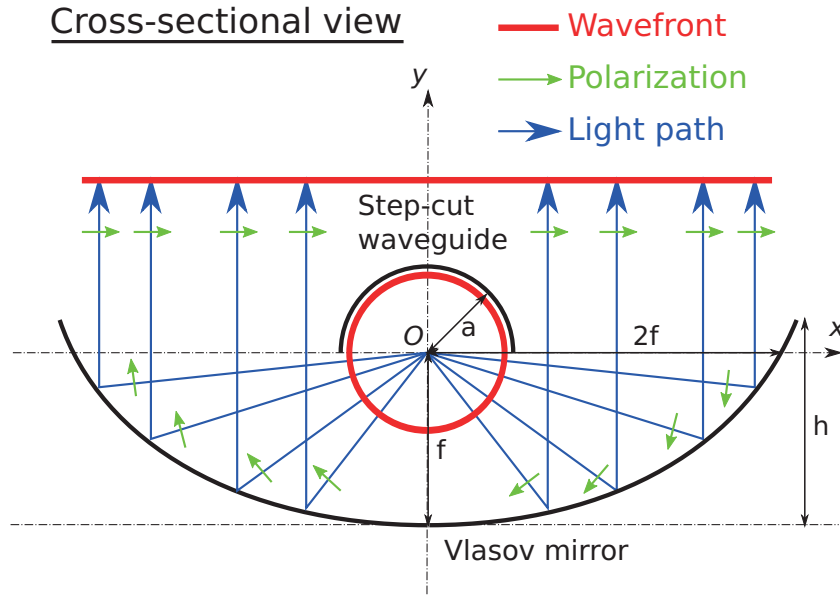


Figure 2.8: Cross-sectional view of the step-cut waveguide and the Vlasov mirror

Parameters of the Vlasov mirror are its length, its width and its focal length. The length in a transverse direction is determined by the depth of the mirror and the depth should be enough to reflect all the light from the step-cut waveguide. The condition for the depth h in Fig. 2.8 would be $h > f$ if there were no diffraction, but because of the diffraction, the condition is modified as

$$h > f + \frac{2f}{\sin \alpha_{mn}} \tan \left(\sqrt{\frac{(2f - a)\lambda \sin \alpha_{mn}}{16af}} \right) \quad [19], \quad (2.17)$$

where α_{mn} is a dispersion angle of the gyrotron output wave, which satisfies

$$\sin(\alpha_{mn}) = \frac{j'_{mn}/a}{2\pi/\lambda_{mn}} \quad (2.18)$$

$$= \frac{j'_{mn}/a}{\sqrt{\left(\frac{j'_{mn}}{R}\right)^2 + \left(\frac{l\pi}{L}\right)^2}} \quad (2.19)$$

$$= \frac{R}{a} \text{ (if } l = 0\text{)}, \quad (2.20)$$

where R is the radius of the cavity resonator, L is the length of the cavity resonator, and a is the radius of the waveguide. The dispersion angle is independent of the gyrotron mode if we use the same gyrotron in different mode.

The length in a longitudinal direction is determined by the condition that it reflects all the light from the step-cut waveguide. Figure 2.9 is a side view of the step-cut waveguide and the Vlasov mirror.

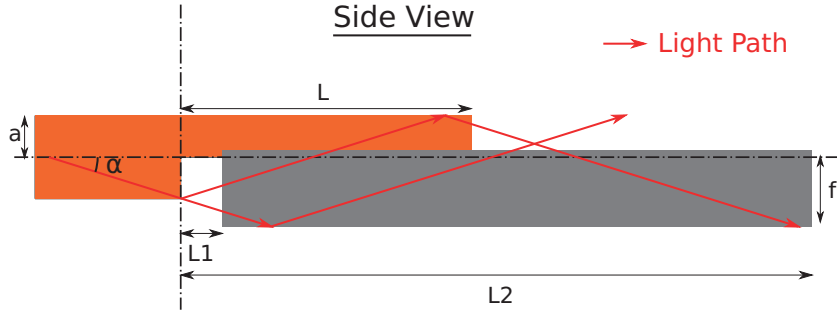


Figure 2.9: Side view of the step-cut waveguide and the Vlasov mirror

The reflection conditions in the longitudinal direction are

$$L1 < (f - a) \cot \left(\alpha + \frac{\lambda}{8a \cos \alpha} \right), \quad (2.21)$$

$$L2 > (2f + 3a) \cot \left(\alpha - \frac{\lambda}{8a \cos \alpha} \right) \text{ [19]}. \quad (2.22)$$

In the above equations, diffraction is considered. If the wavelength λ is enough short ($\lambda \ll a$), the above conditions become identical to those calculated by geometrical optics. In addition, the step-cut length of the waveguide L is limited due to the condition that it can reflect all the light toward the Vlasov mirror and it does not obstruct the lights reflected by the Vlasov mirror. The condition is expressed as

$$2a \cot \alpha < L < (2f - a) \cos \alpha. \quad (2.23)$$

L can be solved when $f > 1.5a$, and parameters used in our experiment are summarized in Table 2.3.

Parameter	[mm]
f	$2a = 28$
L	220
$L1$	73.6
$L2$	554
h	51.5

Table 2.3: Parameters of the step-cut waveguide and the Vlasov mirror

Light reflected from the Vlasov mirror can be treated as if it comes from a plain image source lying behind the Vlasov mirror with emission angle α . The light is linearly polarized. The direction of the polarization is defined as the x -direction. The field over the image source calculated using geometrical optics [20] is

$$E_x = \left(1 + \frac{x^2}{4f^2}\right)^{-\frac{1}{2}} \exp(-iky \cos \alpha). \quad (2.24)$$

Field at a distant point, ψ_{far} , can be calculated by the Huygens equation,

$$\psi_{\text{far}} = \frac{ik}{4\pi} \int_S \psi_s \frac{\exp(-ikr)}{r} (\hat{\mathbf{r}} + \hat{\mathbf{s}}) \cdot \hat{\mathbf{n}} dS, \quad (2.25)$$

where r is a distance from a point on the source to the distant point, $\hat{\mathbf{r}}$ is a unit vector from a point on the source to the distant point, $\hat{\mathbf{s}}$ is a unit vector of the Poynting vector, and $\hat{\mathbf{n}}$ is a normal unit vector of the source plain. Figure 2.10 shows the result for various distances.

In order to convert the wave into the clear bi-Gaussian beam with maximum conversion efficiency, light path of about 10 m is necessary. In that case the conversion efficiency is about 90 %. The reason of the loss of 10 % is that the converted beam is not pure bi-Gaussian but an airy function and therefore there are many sidelobes around the main component. The spot size $w_x(0)$, $w_y(0)$ at the beam waist of the bi-Gaussian beam (= the position of the plain image source) is estimated from the beam size $w_x(z)$, $w_y(z)$ of the far-field by the following equation

$$w_{x,y}(z) = w_{x,y}(0) \sqrt{1 + \left(\frac{\lambda z}{\pi w_{x,y}(0)}\right)^2}, \quad (2.26)$$

and the estimated value is $w_x(0) = 44.5$ mm and $w_y(0) = 22.5$ mm.

There is a large discrepancy between the calculated (Fig. 2.10) and the measured space distribution (Fig. 2.11). Many sidelobes are observed in the measured distribution at $r = 710$ mm. The space distribution at far-field ($r = 3380$ mm) is disturbed due to the interferences between these sidelobes, as shown in Fig. 2.11 (c). Thus we use an aperture whose diameter is 50 mm and it is placed so that only

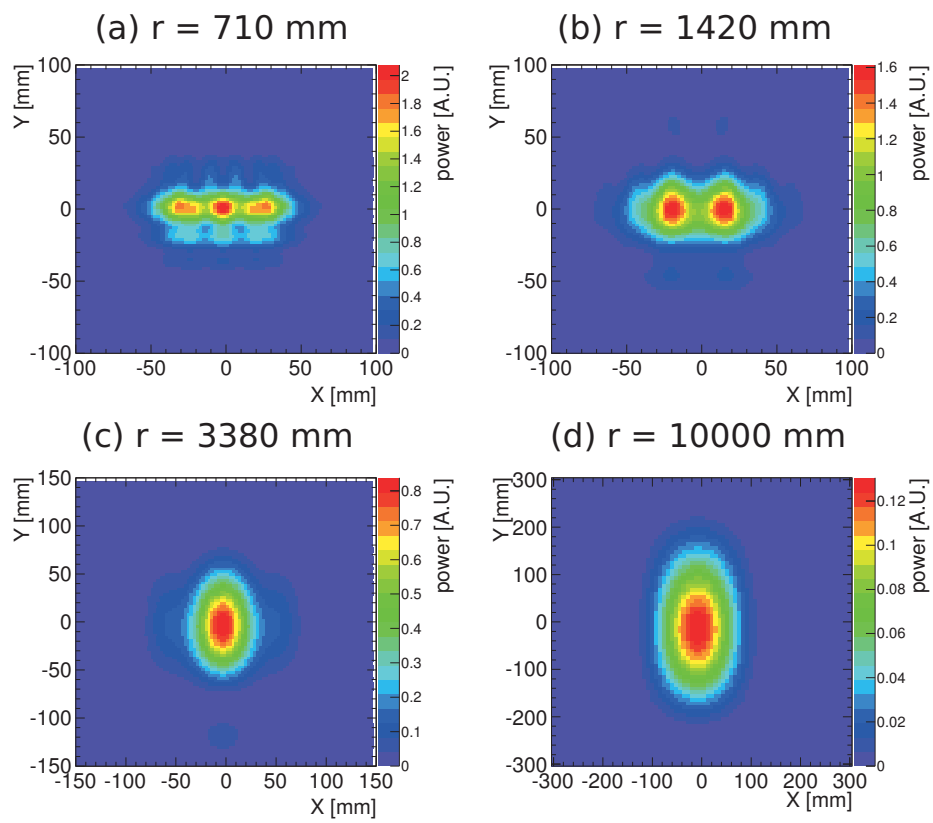


Figure 2.10: Calculated intensity distributions at various distances from the Vlasov mirror

the mainlobe can pass it. Figure 2.11 (d) is the space distribution at $r = 3380$ mm when the aperture is used. The fraction of the beam which passes the aperture is 35 ± 2 %.

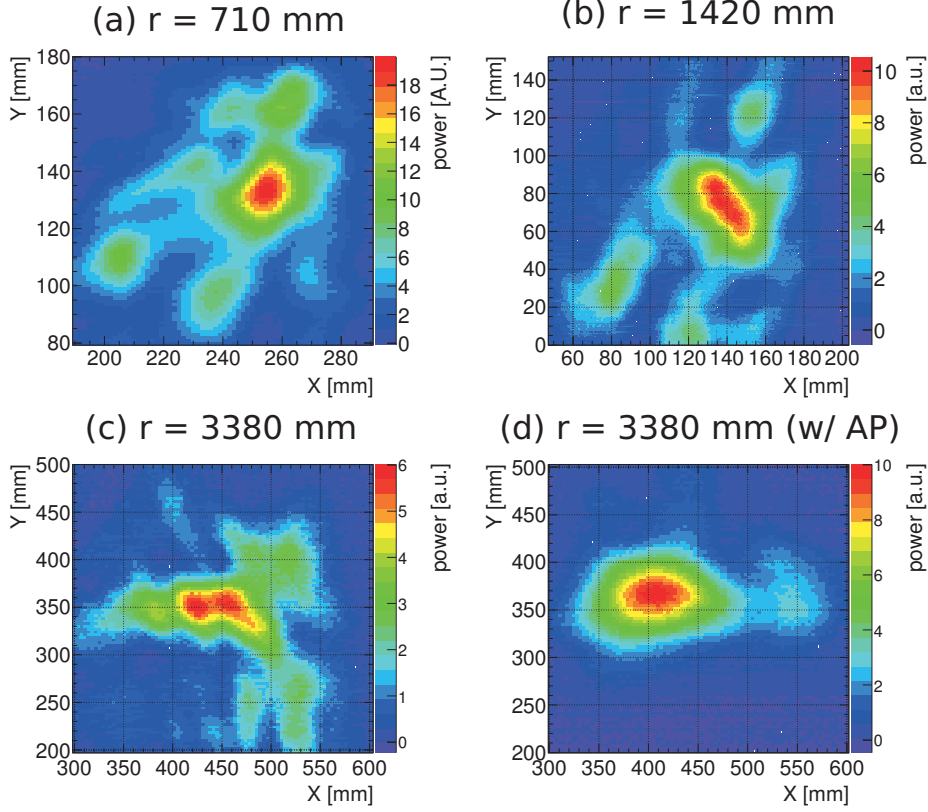


Figure 2.11: Measured intensity distributions at various distances from the Vlasov mirror

The polarization of the converted beam is measured using a grid polarizer which is made from tungsten wires (diameter = $15 \mu\text{m}$, pitch = $60 \mu\text{m}$). Only the electric field perpendicular to the wires can pass the polarizer. The polarizer behaves as metal for the electric field parallel to the wires because electrons of tungsten wires can move freely in the wire direction, therefore the radiation of parallel polarization is reflected by the polarizer. Figure 2.12 is the result of a polarization measurement. θ is the angle of the electric field from the horizontal direction.

The fraction of the beam polarized linearly in $\theta = 0^\circ$ is 80 ± 6 %. The sidelobes remaining even after the aperture are also linearly polarized, but the direction is orthogonal to the mainlobe. Consequently, the overall efficiency is 28 ± 2 % combined with the efficiency of the aperture.

Since the shape of the mainlobe is wide in a horizontal direction, the shape is arranged by two parabolic mirrors (M1, M2) and the nearly circular beam expect

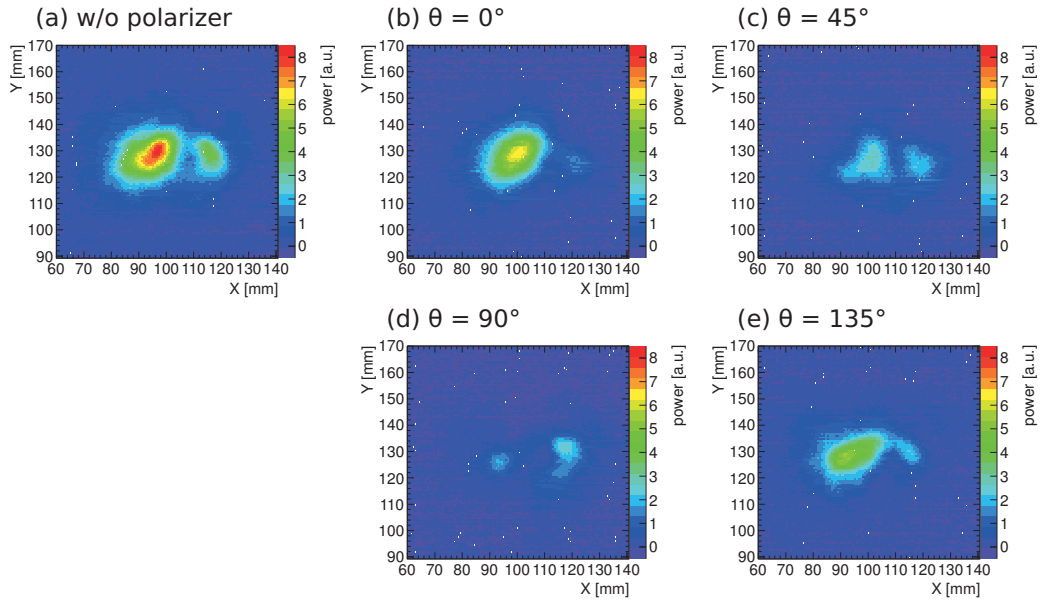


Figure 2.12: Polarization of the converted beam. θ is the angle of the electric field from the horizontal direction.

for the tail at bottom right due to the sidelobe after the aperture is obtained as shown in Fig. 2.13.

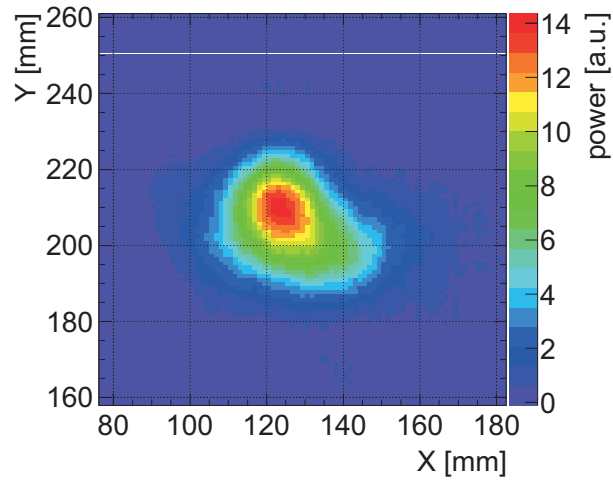


Figure 2.13: Beam shape after the mode converter.

Mode matching

When the waist sizes of the Gaussian beam and the Fabry-Pérot resonant cavity are w_{beam} and w_{FP} , respectively, and the distance of their waist positions is d , the mode matching ratio η (Eq. (2.13)) becomes

$$\eta = \frac{4w_{\text{beam}}^2 w_{\text{FP}}^2}{(w_{\text{beam}}^2 + w_{\text{FP}}^2)^2 + (\lambda d/\pi)^2}. \quad (2.27)$$

The waist of our Fabry-Perot cavity is at the front plain mirror of the cavity and the waist size is determined by the curvature of the end mirror and the cavity length. The waist size and its position of the Gaussian beam have to be matched with those of the Fabry-Pérot cavity in order to obtain good coupling. We use a spherical plano convex lens (curvature $r = 120$ mm) made of Teflon for the purpose and the lens is placed between the mirror 3 (M3) and the Fabry-Pérot cavity. The transmittance of lens can be calculated from the refractive index and the absorption coefficient of the material. The one-side power reflectance at the interface between the air and the material (refractive index n , absorption coefficient α) is

$$R = \left(\frac{1 - n}{1 + n} \right)^2, \quad (2.28)$$

thus the transmittance of the lens (thickness L) is

$$T_{\text{lens}} = (1 - R)^2 \exp(-\alpha L) \quad (2.29)$$

Therefore, materials such as quartz are not suitable for sub-THz radiation because its refractive index at frequency of sub-THz is large, for example, refractive index of quartz at 202.9 GHz is about 2.0. On the other hand, the refractive index of Teflon is 1.4 and the reflection is small. Transmittance of the Teflon lens is measured 89 ± 4 %, which is consistent with the calculation from the refractive index of Teflon ($n = 1.4$ at 203 GHz) and the absorption coefficient of Teflon ($\alpha = 0.05$ [cm⁻¹] at 203 GHz) [21]. The focal length of the lens is $f = r/(n - 1) = 300$ mm.

2.2.3 Fabry-Pérot Resonant Cavity

Theory of the Fabry-Pérot resonant cavity

A Fabry-Pérot resonant cavity is made with a plane front mirror and a concave end mirror (Fig. 2.14). The incident light is resonant with the cavity when the cavity length L is equal to the integral multiple of $\lambda/2$.

The input field is defined as $E_{\text{in}} = E_0 e^{ikz}$. The front mirror is at $z = 0$ and the end mirror is at $z = L$. Then the transmittance of the cavity is

$$E_{\text{tr}} = E_0 e^{ik(z-L)} t_{\text{f}} t_{\text{e}} e^{ikL} \sum_{n=0}^{\infty} [r_{\text{f}} r_{\text{e}} e^{2ikL}]^n \quad (2.30)$$

$$= E_0 e^{ik(z-L)} \frac{t_{\text{f}} t_{\text{e}} e^{ikL}}{1 - r_{\text{f}} r_{\text{e}} e^{2ikL}} \quad (2.31)$$

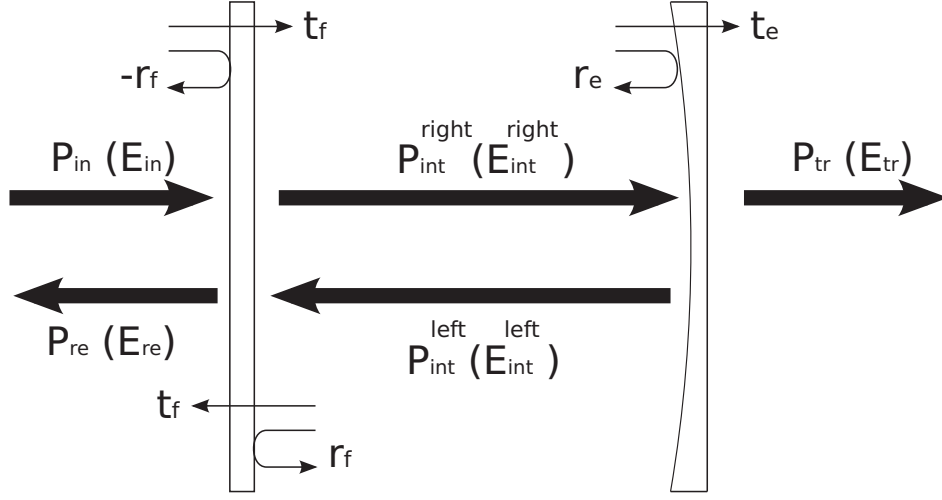


Figure 2.14: A schematic of a Fabry-Pérot resonant cavity.

where t_f and t_e are the amplitude transmittance of the front mirror and the end mirror, r_f and r_e are the amplitude reflectance of the front mirror and the end mirror, respectively, and e^{ikL} is a phase shift per way.

In the same way, reflectance of the cavity is

$$E_{re} = E_0 e^{-ikz} (-r_f) + E_0 e^{-ikz} r_e t_f^2 e^{2ikL} \sum_{n=0}^{\infty} [r_f r_e e^{2ikL}]^n \quad (2.32)$$

$$= E_0 e^{-ikz} \left(-r_f + \frac{t_f^2 r_e e^{2ikL}}{1 - r_f r_e e^{2ikL}} \right). \quad (2.33)$$

The internal wave going to the right direction E_{acc}^{right} is

$$E_{acc}^{right} = \frac{E_{tr}}{t_e} = E_0 e^{ikz} \frac{t_f}{1 - r_f r_e e^{2ikL}}, \quad (2.34)$$

and the internal wave going to the left direction E_{acc}^{left} is

$$E_{acc}^{left} = \frac{E_{re} - E_0 e^{-ikz} (-r_f)}{t_f} = E_0 e^{-ikz} \left(\frac{t_f r_e e^{2ikL}}{1 - r_f r_e e^{2ikL}} \right). \quad (2.35)$$

The total internal field is sum of these,

$$E_{acc} = E_{acc}^{right} + E_{acc}^{left} \quad (2.36)$$

$$= E_0 \left(e^{ikz} + r_e e^{-ikz} e^{2ikL} \right) \frac{t_f}{1 - r_f r_e e^{2ikL}}. \quad (2.37)$$

From Eq. (2.31), (2.33) and (2.37), we obtain

$$\frac{P_{\text{tr}}}{P_{\text{in}}} = \frac{T_{\text{f}}T_{\text{e}}}{(1 - \sqrt{R_{\text{f}}R_{\text{e}}})^2 (1 + F \sin^2 kL)} \quad (2.38)$$

$$\frac{P_{\text{re}}}{P_{\text{in}}} = \frac{[\sqrt{R_{\text{f}}} - (T_{\text{f}} + R_{\text{f}})\sqrt{R_{\text{e}}}]^2 + 4(T_{\text{f}} + R_{\text{f}})\sqrt{R_{\text{f}}R_{\text{e}}}\sin^2 kL}{(1 - \sqrt{R_{\text{f}}R_{\text{e}}})^2 (1 + F \sin^2 kL)} \quad (2.39)$$

$$\frac{P_{\text{acc}}}{P_{\text{in}}} = \frac{T_{\text{f}} [(1 + \sqrt{R_{\text{e}}})^2 - 4\sqrt{R_{\text{e}}}\sin^2 k(z - L)]}{(1 - \sqrt{R_{\text{f}}R_{\text{e}}})^2 (1 + F \sin^2 kL)}, \quad (2.40)$$

where P_{in} , P_{re} , P_{tr} , and P_{acc} are the incident, the reflected, the transmitted, and the accumulated power, respectively, T_{f} and T_{e} are the power transmittance of the front mirror and the end mirror, respectively, R_{f} and R_{e} are the power reflectance of the front mirror and the end mirror, respectively, and

$$F = \frac{4\sqrt{R_{\text{f}}R_{\text{e}}}}{(1 - \sqrt{R_{\text{f}}R_{\text{e}}})^2} = \left(\frac{2\mathcal{F}}{\pi}\right)^2. \quad (2.41)$$

\mathcal{F} is called finesse. If we denote $\rho = R_{\text{f}}R_{\text{e}}$, which is called round-trip reflectivity, finesse is expressed as

$$\mathcal{F} = \frac{\pi\sqrt[4]{\rho}}{1 - \sqrt{\rho}} \approx \frac{2\pi}{1 - \rho}. \quad (2.42)$$

P_{acc} depends on z . Average power over the cavity is

$$\frac{\langle P_{\text{acc}} \rangle}{P_{\text{in}}} = \frac{1}{L} \int_0^L \frac{T_{\text{f}} [(1 + \sqrt{R_{\text{e}}})^2 - 4\sqrt{R_{\text{e}}}\sin^2 k(z - L)]}{(1 - \sqrt{R_{\text{f}}R_{\text{e}}})^2 [1 + F \sin^2 kL]} dz \quad (2.43)$$

$$= \frac{T_{\text{f}}(1 + R_{\text{e}})}{(1 - \sqrt{R_{\text{f}}R_{\text{e}}})^2 (1 + F \sin^2 kL)}, \quad (2.44)$$

Therefore, given P_{tr} , T_{e} , and R_{e} , we can estimate $\langle P_{\text{acc}} \rangle$ via following equation.

$$\langle P_{\text{acc}} \rangle = \frac{1 + R_{\text{e}}}{T_{\text{e}}} P_{\text{tr}} \quad (2.45)$$

$\langle P_{\text{acc}} \rangle / P_{\text{in}}$ becomes maximum when resonance occurs ($kL = n\pi$). The maximum accumulated power is

$$\frac{\langle P_{\text{acc}}^{\text{max}} \rangle}{P_{\text{in}}} = \frac{T_{\text{f}}(1 + R_{\text{e}})}{(1 - \sqrt{R_{\text{f}}R_{\text{e}}})^2}, \quad (2.46)$$

and the transmitted power also becomes maximum,

$$\frac{P_{\text{tr}}^{\text{max}}}{P_{\text{in}}} = \frac{T_{\text{f}}T_{\text{e}}}{(1 - \sqrt{R_{\text{f}}R_{\text{e}}})^2}. \quad (2.47)$$

On the other hand, the reflected power becomes minimum

$$\frac{P_{\text{re}}^{\text{min}}}{P_{\text{in}}} = \frac{[\sqrt{R_{\text{f}}} - (T_{\text{f}} + R_{\text{f}})\sqrt{R_{\text{e}}}]^2}{(1 - \sqrt{R_{\text{f}}R_{\text{e}}})^2}. \quad (2.48)$$

Figure 2.15 is the basic performance ($P_{\text{acc}}/P_{\text{in}}$, $P_{\text{tr}}/P_{\text{in}}$, and $P_{\text{re}}/P_{\text{in}}$) calculated with $R_{\text{f}} = 99.38\%$, $T_{\text{f}} = 0.39\%$, $R_{\text{e}} = 99.8\%$, and $T_{\text{e}} = 0.2\%$. Since $T_{\text{f}} + R_{\text{f}} \neq 1$

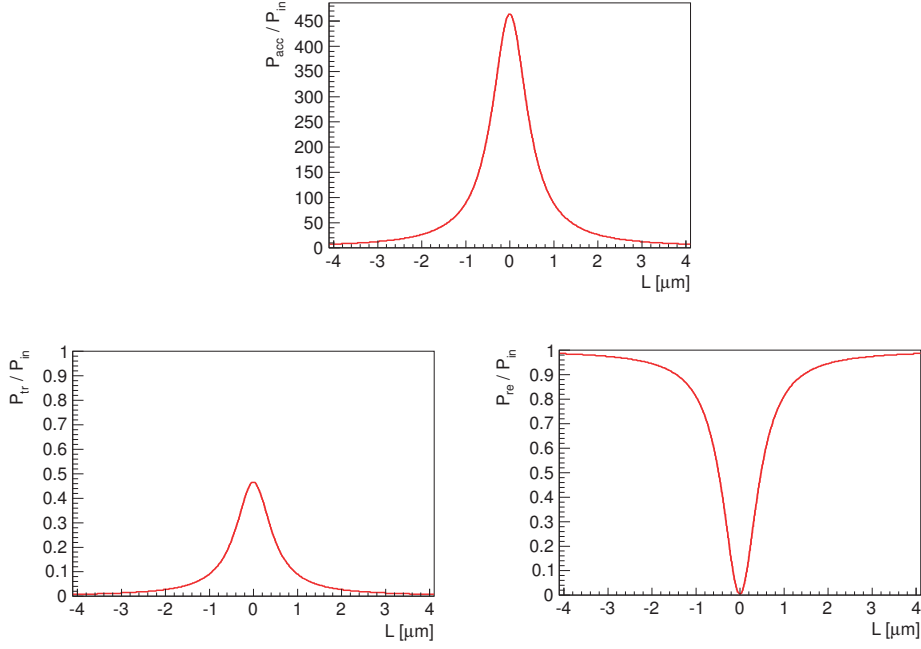


Figure 2.15: Basic performance of Fabry-Pérot resonant cavity calculated with $R_{\text{f}} = 99.38\%$, $T_{\text{f}} = 0.39\%$, $R_{\text{e}} = 99.8\%$, and $T_{\text{e}} = 0.2\%$. The top figure shows accumulated power, the bottom left figure shows transmitted power, and the bottom right figure shows reflected power.

due to the loss, sum of the transmitted power and the reflected power is less than the incident power. The width of the peak is related to the finesse of the cavity by the following equation

$$\mathcal{F} = \frac{\lambda/2}{\Gamma}. \quad (2.49)$$

Next, we consider the beam shape in the Fabry-Pérot cavity. The lowest wave mode of the Fabry-Pérot cavity is a Gaussian beam (or TEM_{00} mode). Figure 2.16 is a general Fabry-Pérot cavity with two mirrors of different curvatures (R_1 , R_2).

The cavity resonator is stable when

$$0 \leq \left(1 - \frac{L}{R_1}\right) \left(1 - \frac{L}{R_2}\right) \leq 1. \quad (2.50)$$

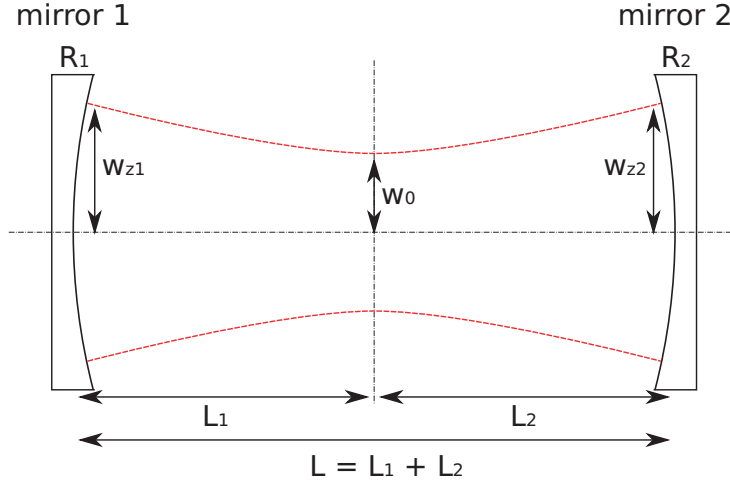


Figure 2.16: The beam shape in the Fabry-Pérot cavity.

The waist position is at L_1 from mirror 1 and L_2 from mirror 2. L_1 and L_2 is

$$L_1 = \frac{L(R_2 - L)}{R_1 + R_2 - 2L} \quad (2.51)$$

$$L_2 = \frac{L(R_1 - L)}{R_1 + R_2 - 2L}, \quad (2.52)$$

and the waist size w_0 is

$$w_0 = \sqrt{\frac{\lambda}{\pi} \frac{\sqrt{L(R_1 - L)(R_2 - L)(R_1 + R_2 - L)}}{R_1 + R_2 - 2L}}. \quad (2.53)$$

The beam sizes at the mirror 1 and 2 are

$$w_{z1} = \sqrt{\frac{\lambda}{\pi} R_1 \sqrt{\frac{L(R_2 - L)}{(R_1 - L)(R_1 + R_2 - L)}}} \quad (2.54)$$

$$w_{z2} = \sqrt{\frac{\lambda}{\pi} R_2 \sqrt{\frac{L(R_1 - L)}{(R_2 - L)(R_1 + R_2 - L)}}} \quad (2.55)$$

Performance of the Fabry-Pérot resonant cavity

Our Fabry-Pérot cavity is composed of a gold mesh plain mirror as a front mirror and a Cu concave mirror as an end mirror. The curvature of the concave mirror is $R = 300$ mm and therefore the focal length $f = R/2 = 150$ mm. The cavity length $L = 136$ mm. By substituting $R_1 = \infty$ and $R_2 = R$, the beam waist is at the front

mirror ($L_1 = 0$, $L_2 = L$) and the waist size is

$$w_0 = w_{z1} = \sqrt{\frac{\lambda}{\pi} \sqrt{L(R-L)}} = 8.38 \text{ [mm]} \quad (2.56)$$

$$w_z = w_{z2} = \sqrt{\frac{\lambda}{\pi} R \sqrt{\frac{L}{R-L}}} = 11.34 \text{ [mm]}. \quad (2.57)$$

The cavity resonator is stable since the parameters satisfy Eq. (2.50),

$$0 \leq \left(1 - \frac{136}{\infty}\right) \left(1 - \frac{136}{300}\right) = 0.55 \leq 1. \quad (2.58)$$

The Au mesh mirror is a key component of the cavity. In order to obtain high gain resonator, both of the high finesse and the reasonable transmittance of the front mirror are necessary. Figure 2.17 is a picture of the mesh mirror used in the experiment.

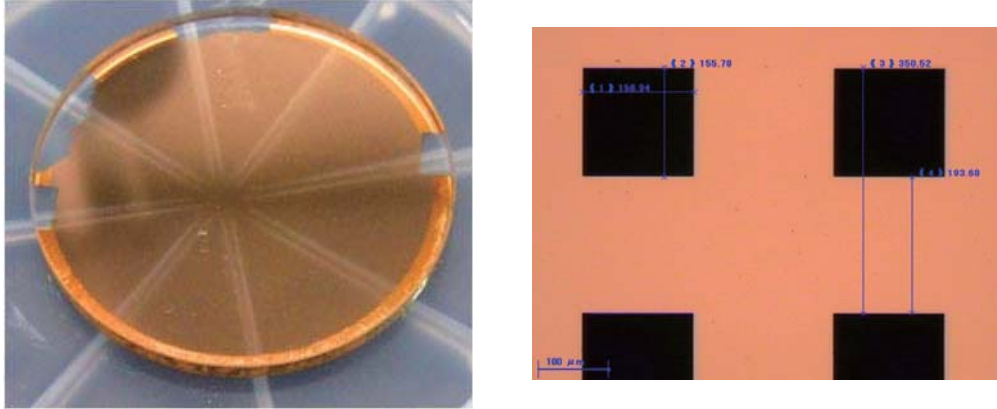


Figure 2.17: Pictures of the gold mesh mirror. The right figure is its magnified picture.

The Au mesh is made on a SiO_2 plate using conventional photolithography and liftoff technique [22]. Thickness of the mesh pattern is $1 \mu\text{m}$, which is 6 times thicker than the skin depth of Au at 203 GHz. Skin depth δ is expressed as

$$\delta = \sqrt{\frac{1}{\pi f \mu \sigma}} \text{ [m]}, \quad (2.59)$$

where f is wave frequency, $\mu = 4\pi \times 10^{-7}$ is the magnetic permeability, and σ is electrical conductivity of metal. In our case, $f = 203 \text{ GHz}$ and $\sigma = 41 \times 10^6 \text{ S/m}$ (Au), therefore $\delta = 0.17 \mu\text{m}$.

The line width is $200 \mu\text{m}$ and the line separation is $160 \mu\text{m}$, which is designed to obtain high reflectivity and reasonable transmittance by 3D electromagnetic field simulation based on the finite integration technique (FIT) [23, 24] using CST

MICROWAVE STUDIO (CST MWS). Figure 2.18 is the result of the simulation whose parameters are the same as the mesh used in the experiment. The fluctuation with a cycle of about 25 GHz is due to the interference in the SiO₂ substrate, whose thickness is 3 mm. The cycle is equal to $c/(2nL)$, where c is the speed of light in vacuum, n is the refractive index of SiO₂ ($n = 2.0$ at 202.9 GHz), and L is the thickness of the SiO₂ substrate. The reflectance basically increases with increase of frequency because the larger wavelength results in less transmittance of the mesh pattern. Its simulated reflectivity is $R_f = 99.38\%$ and the transmittance is $T_f = 0.39\%$.

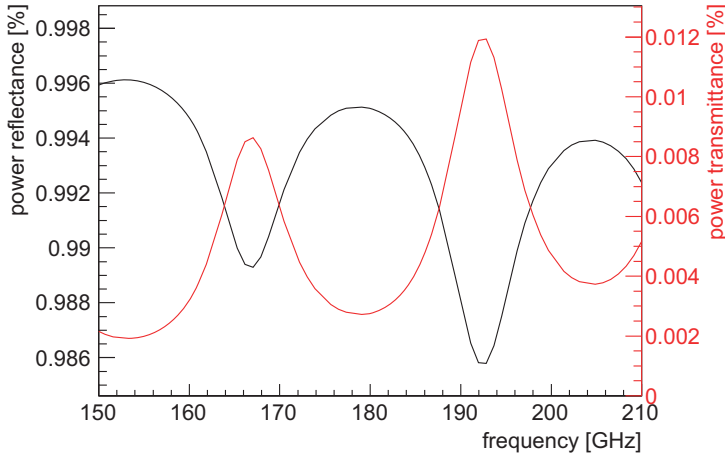


Figure 2.18: The reflectance (black) and the transmittance (red) of the Au plain mesh mirror simulated using CST MICROWAVE STUDIO.

Cavity length is controlled by moving the Cu concave mirror mounted on an X-axis stage (NANO CONTROL TS102-G). It is an SIDMTM (Smooth Impact Drive Mechanism) actuator using the piezoelectric element as the driving force. Its long stroke (15 mm) and its high resolution (10 nm) is achieved at the same time by combining coarse motion and slight motion (Fig. 2.19). The closed loop control with a linear encoder in the main body enables accurate control with 10 nm resolution (Fig. 2.20).

Figure 2.22 shows the accumulated power (left), which is estimated from the transmitted power, and the reflected power (right) measured while changing cavity length of the Fabry-Pérot cavity. FWHM of the resonance peak is 1.19(6) μm , which corresponds to the finesse $\mathcal{F} = 623 \pm 29$ (or the round-trip reflectivity $\rho = R_f R_e = 98.99(5)\%$). Relative power is measured with pyroelectric detectors (Spectrum Detector Inc. SPH-49, Fig. 2.21). Pyroelectric detectors are thermal

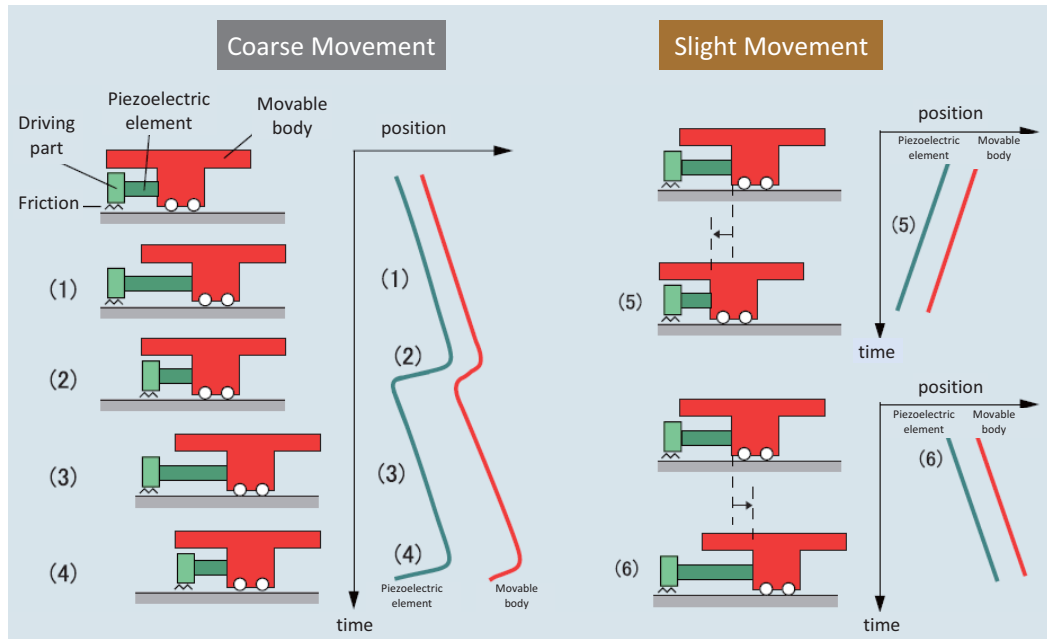


Figure 2.19: Principal of operation of an SIDM™ (Smooth Impact Drive Mechanism) actuator.

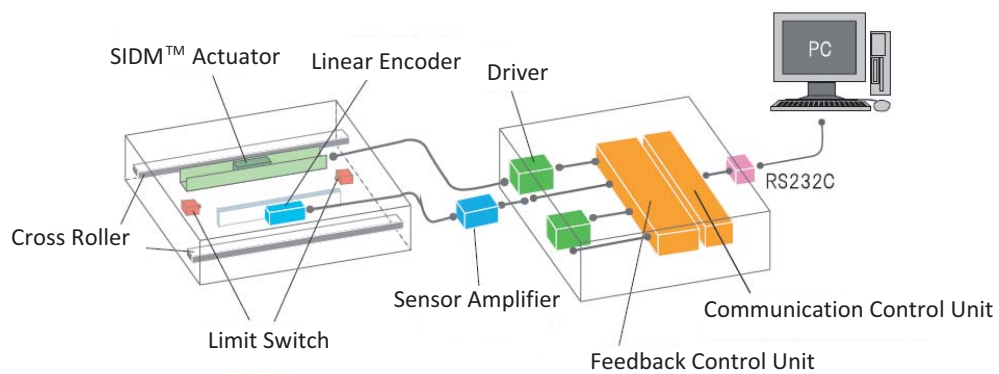


Figure 2.20: Structural drawing of the X-axis stage and its controller.



Figure 2.21: Pyroelectric detectors (Spectrum Detector Inc. SPH-49).

detectors made of lithium tantalate (LiTaO_3). Lithium tantalate is a pyroelectric crystal whose ends become oppositely charged when heated. The output current of a pyroelectric detector, which is proportional to a change in temperature, is converted to voltage output via an operational amplifier and a feedback resistance. Transmitted power is transmitted through a hole (diameter = 0.6 mm) at the center of the Cu concave mirror. The hole diameter is smaller than half of the wavelength ($\lambda/2$), therefore its transmittance is much smaller than the fraction of the beam within the hole area. This is important to keep high reflectivity of the Cu concave mirror and obtain high finesse of the Fabry-Pérot cavity. The accumulated power reaches ~ 10 kW at the resonance peak of the Fabry-Pérot resonant cavity. The accumulated power is estimated from the transmitted power of the Fabry-Pérot resonant cavity. Detail of the power estimation is described in next subsection.

2.2.4 Power Estimation

Power accumulated in the cavity is estimated from the transmitted power, that is the output voltage V_{tr} [V] of the pyroelectric detector behind the hole at the center of the Cu concave mirror, since they are related via Eq. (2.45). Calibration constant $C_{\text{calib}} = P_{\text{acc}}/V_{\text{tr}}$ [W/V] is necessary to estimate accumulated power P_{acc} [W].

We obtain the calibration constant in the following way because there is no radiation sources whose absolute power and the shape is well-known in the frequency and power domain of our experiment. In this section, details of the following measurements are explained.

1. measure $P_{\text{in}}/V_{\text{in}}$ [W/V] with water

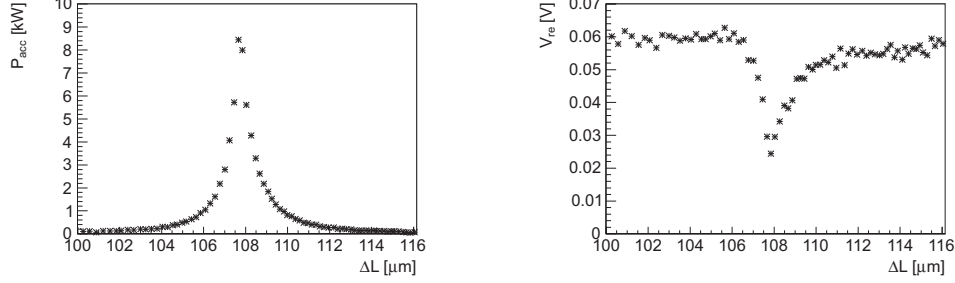


Figure 2.22: The accumulated power (left) and the reflected power (right) of the Fabry-Pérot resonant cavity measured while changing cavity length.

2. measure $V_{\text{tr}}/V_{\text{in}}$ of the hole of Cu concave mirror
3. measure $P_{\text{hole}}/P_{\text{in}}$ with PVC sheet
4. calculate $P_{\text{hole}}/P_{\text{acc}}$ from the cavity length, the curvature of the Cu concave mirror, the hole diameter, and the reflectivity of the Cu concave mirror

The calibration constant is obtained from these by the following equation.

$$C_{\text{calib}} = \frac{P_{\text{acc}}}{V_{\text{tr}}} = \frac{P_{\text{in}}/V_{\text{in}} \times P_{\text{hole}}/P_{\text{in}}}{V_{\text{tr}}/V_{\text{in}} \times P_{\text{hole}}/P_{\text{acc}}} \quad (2.60)$$

Measurement of $P_{\text{in}}/V_{\text{in}}$ [W/V] with water

Water is a good absorber of sub-THz radiation (α is about 10^2 [cm^{-1}] [17]). We fill $V = 50$ cc of water in a box made of Teflon. Cross section of water is $100 \text{ mm} \times 100 \text{ mm}$ and its thickness is 5 mm. The cross section is much larger than the beam size, and 5 mm of water is enough thick to absorb all of the radiation which pass through Teflon wall, whose thickness at the beam side is 3 mm. Transmittance of Teflon wall at the beam side is $T_{\text{Teflon}} = 95.1 \pm 1.4$ %, which is calculated from the thickness, the refractive index ($n = 1.44$) and the absorption coefficient ($\alpha = 0.05$ [cm^{-1}]) [21]. The error is mainly due to the uncertainty of the absorption coefficient of the Teflon. Temperature increase ΔT [K] after beam exposure for Δt [sec] is measured. During beam exposure, the water is agitated. A fraction of the input power V_{in} [V] during beam exposure is monitored with a pyroelectric detector. The temperature of water increases in proportion to the integral of V_{in} over time of exposure, but the water cools down as time passes due to diffusion as shown in Fig. 2.23. In order to estimate the total beam power P_{in} normalized by V_{in} , the graph is fitted by the following equation

$$T \left(\int_0^t V_{\text{in}}(t') dt' \right) = p_0 + p_1 p_2 \left(1 - \exp \left(-\frac{1}{p_2} \int_0^t V_{\text{in}}(t') dt' \right) \right), \quad (2.61)$$

and $P_{\text{in}}/V_{\text{in}}$ can be estimated from its gradient at $V \cdot t = 0$, which is equal to p_1 , because the gradient is equal to

$$\frac{\langle P_{\text{in}}/V_{\text{in}} \rangle \cdot f_{\text{duty}} \cdot T_{\text{PTFE}}}{C \cdot V} \quad (2.62)$$

where C ($= 4.18(1)$ [J/K·g]) is the heat capacity of water at room temperature and f_{duty} ($= 0.3$) is duty ratio of the beam. Thus $P_{\text{in}}/V_{\text{in}} = 694 \pm 44$ [W/V] is obtained.

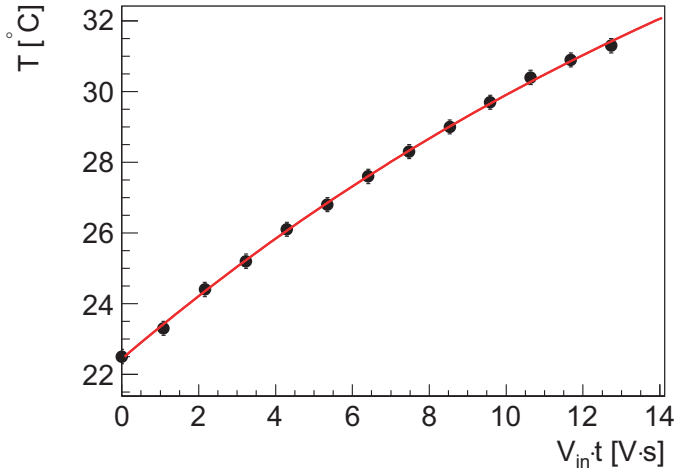


Figure 2.23: Temperature of water measured while the water is exposed to the Gaussian beam during 120 s. The horizontal axis of the figure is the integral of the input beam power measured with a pyroelectric detector.

Measurement of $V_{\text{tr}}/V_{\text{in}}$ of the Cu concave mirror

A portion of radiation which comes within the hole area transmits the Cu concave mirror is detected by the pyroelectric detector because the diameter of the hole is smaller than $\lambda/2$. Input beam power V_{in} [V] and transmitted power through the Cu concave mirror V_{tr} [V] are measured with pyroelectric detectors at the same time. Figure 2.24 shows V_{tr} normalized by V_{in} while changing cavity length. The dependency on the cavity length in $\lambda/2$ cycle is due to the resonance with very low finesse. In order to measure the transmittance, the Cu concave mirror must be placed perpendicular to the beam, and then the beam reflected by the Cu concave mirror can go back to the gyrotron. There is a Teflon lens in the light path. The Cu concave mirror and the lens become an optical resonator with very low finesse and the interference curve is observed in Fig. 2.24.

In order to obtain the value if there is no interference, the graph is fitted by Eq. (2.38) with initial phase, that is,

$$\frac{V_{\text{tr}}}{V_{\text{in}}} = \frac{\langle V_{\text{tr}}/V_{\text{in}} \rangle}{1 + \rho + \sqrt{\rho} \cos \left(2\pi \frac{x - \Delta x}{\lambda/2} \right)} \quad (2.63)$$

where $\langle V_{\text{tr}}/V_{\text{in}} \rangle$ is the value without interference, Δx is the initial phase times $\lambda/4\pi$. As a result, $\langle V_{\text{tr}}/V_{\text{in}} \rangle = 0.09458(72)$ is obtained in the case of this beam alignment.

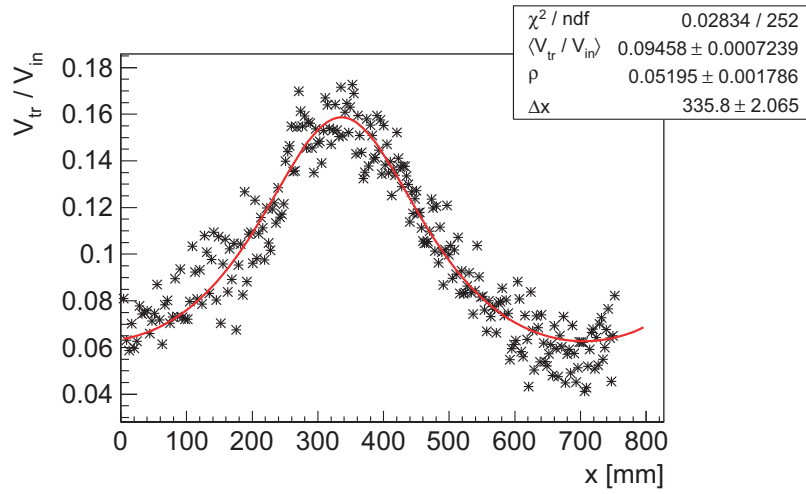


Figure 2.24: The transmitted power of the Cu concave mirror V_{tr} normalized by the input beam power V_{in} while changing the cavity length L by $\lambda/2$.

Measurement of $P_{\text{hole}}/P_{\text{in}}$ with PVC sheet

Because space distribution of the input beam is similar to but not the same as that of the accumulated electromagnetic field in the cavity, correction of the difference is necessary. How much fraction of the input beam comes within the hole area of the Cu concave mirror is measured with PVC sheet. PVC sheet is placed at the same position as the face of the Cu concave mirror and is exposed to the incident beam. Thus the space distribution of the input beam at the Cu mirror is measured. Relative total power of the input beam P_{in} is estimated from the integral of the temperature increase over the PVC sheet. There is remaining background even after the space distribution before beam exposure is subtracted from that after beam exposure. The background is estimated from sideband where the beam never comes, and subtracted from the integral. The error of P_{in} is estimated from the amount of the background in the integral region.

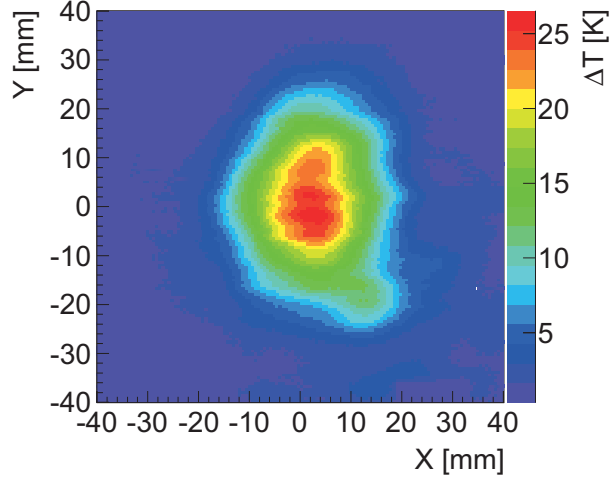


Figure 2.25: A picture of the PVC sheet taken by IR camera to estimate $P_{\text{hole}}/P_{\text{in}}$. The origin is the position of the hole at the center of the Cu concave mirror.

Relative power coming within the hole area P_{hole} is estimated from product of the temperature increase at the center of the PVC sheet, which should be the same as the center of the Cu concave mirror, and the hole size. This is because the resolution of the IR camera is not enough (pixel size is about $0.5 \text{ mm} \times 0.5 \text{ mm}$). The error of P_{hole} derives from the alignment uncertainty ($\pm 1 \text{ mm}$) of the center of the PVC sheet. The other uncertainties are cancelled when divided by P_{in} . The uncertainty of the hole diameter is almost cancelled when divided by $P_{\text{hole}}/P_{\text{acc}}$. In the case of this beam alignment, $P_{\text{hole}}/P_{\text{in}} = 3.06^{+0.27}_{-0.17} \times 10^{-4}$.

Calculation of $P_{\text{hole}}/P_{\text{acc}}$

The internal waveform of the Fabry-Pérot cavity is Gaussian. Its space distribution is determined by its beam size and the beam size can be calculated with the following three parameters, the cavity length $L = 136 \text{ mm}$, the curvature of the Cu concave mirror $R = 300 \text{ mm}$, and the frequency of the radiation $f = 202.9 \text{ GHz}$. The beam size at the Au mesh mirror is $w_0 = 8.38 \text{ mm}$ and that at the Cu concave mirror is $w_z = 11.34 \text{ mm}$.

$P_{\text{hole}}/P_{\text{acc}}$ is estimated from the integral of the space distribution of the beam

over the hole area divided by $(1 + R_e)$ (see Eq. (2.45)),

$$\frac{P_{\text{hole}}}{P_{\text{acc}}} = \frac{\int_0^{0.3} \exp(-2(r/w_z)^2) r dr}{\int_0^\infty \exp(-2(r/w_z)^2) r dr} \cdot \frac{1}{1 + R_e} = 7.02(24) \times 10^{-4}. \quad (2.64)$$

R_e is evaluated from the round-trip reflectivity $\rho = R_f R_e = 98.99(5) \%$ and the fact that the possible maximum of R_e is 99.85 %, which is the reflectivity of Cu, and as a result, $R_e = 99.42(43) \%$. The manufacturing accuracy of the hole is 0.01 mm in diameter.

Result of the power estimation

C_{calib} is obtained from the results of these four measurements using Eq. (2.60),

$$C_{\text{calib}} = \frac{P_{\text{acc}}}{V_{\text{tr}}} = \frac{P_{\text{in}}/V_{\text{in}} \times P_{\text{hole}}/P_{\text{in}}}{V_{\text{tr}}/V_{\text{in}} \times P_{\text{hole}}/P_{\text{acc}}} \quad (2.65)$$

$$= \frac{694 \pm 44 \text{ [W/V]} \times 3.06_{-0.17}^{+0.27} \times 10^{-4}}{0.09458(72) \times 7.02(24) \times 10^{-4}} \quad (2.66)$$

$$= 3.20_{-0.29}^{+0.37} \text{ [kW/V]}. \quad (2.67)$$

We repeat these measurements 10 times in order to estimate the uncertainty due to the discrepancy between the beam shape during the $P_{\text{hole}}/P_{\text{in}}$ measurement with a PVC sheet and that during the $V_{\text{tr}}/V_{\text{in}}$ measurement with the Cu concave mirror. The arithmetic average of these 10 measurements is $2.91_{-0.36}^{+0.52}$ kW/V, and the standard deviation of these 10 measurements is 0.80 kW/V. We denote quadrature sum of the arithmetic mean error and the standard deviation as a total error. Consequently, we obtain

$$C_{\text{calib}} = 2.91_{-0.88}^{+0.95} \text{ [kW/V]}. \quad (2.68)$$

It is difficult to perform these two measurements at the same time because of the difference between their measurement times. If we can perform these two measurements at the same time with an appropriate beam splitter, the uncertainty of the hole position becomes large.

2.2.5 Stabilization

We have to stabilize gyrotron output power and keep resonance of the Fabry-Pérot cavity during the measurement of the hyperfine transition. Figure 2.26 shows the schematic diagram of the feedback stabilization system. The incident power and the power reflected from the Fabry-Pérot cavity are measured with pyroelectric detectors placed behind the Mirror 3, which is a beam splitter. The transmitted power of the Fabry-Pérot cavity is also measured with a pyroelectric detector placed behind the hole at the center of the Cu concave mirror.

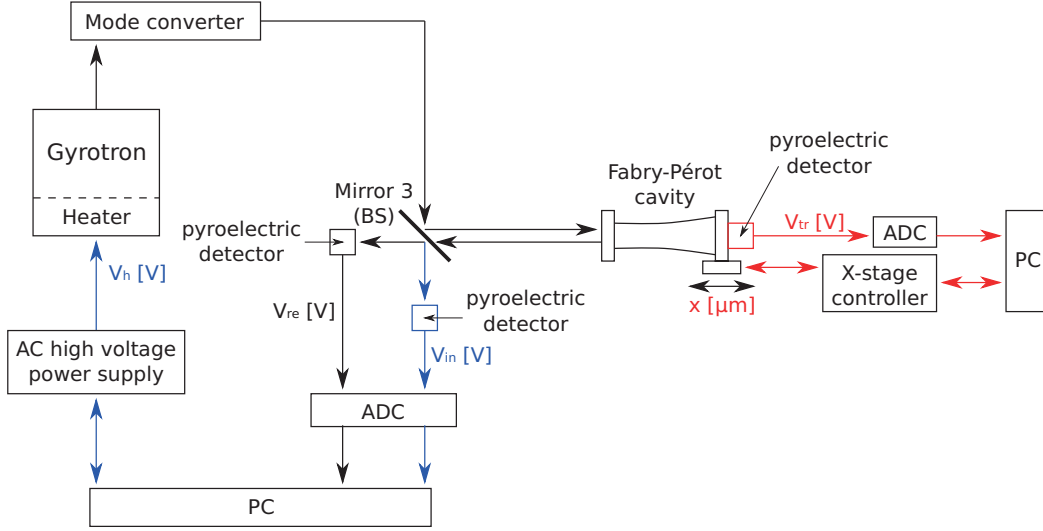


Figure 2.26: Schematic diagram of the feedback stabilization system. The feedback circuit for the gyrotron output power is shown in blue line. The red line shows the feedback circuit for the Fabry-Pérot resonant cavity stabilization.

Stabilization of the gyrotron output power

The heater of the electron gun is controlled to stabilize gyrotron output power, since the temperature of the heater is higher, more electrons are emitted from the electron gun and the gyrotron output power becomes higher.

The gyrotron output power is measured as follows. The Gaussian beam is split by a beam splitter (or Mirror 3 in Fig. 2.7). It is a gold mesh mirror whose power transmittance is high (2.7 %). The line width is $50 \mu\text{m}$ and the line separation is $130 \mu\text{m}$. The beam reflected by the beam splitter goes to the Fabry-Pérot resonant cavity. On the other hand, the beam through the beam splitter is monitored by a pyroelectric detector. We stabilize the output of the pyroelectric detector (V_{in} [V]), since it is a sample of the gyrotron output power. The output of the pyroelectric detector is measured with a 16-bit ADC (NATIONAL INSTRUMENTS NI USB-6215). The gyrotron output without feedback stabilization is very unstable as shown in Fig. 2.27. It is necessary to stabilize it.

The temperature of the heater of the electron gun is determined by its AC high voltage. The AC high voltage power supply (MATSUSADA SRJ500) can be controlled from the PC via RS232C. The heater voltage V_h is determined by the following equation (PI control).

$$V_h(n) = V_h(n-1) + K_P(V_{\text{in}}(n-1) - V_{\text{in}}(n)) + K_I(V_{\text{in}}^{\text{target}} - V_{\text{in}}(n)), \quad (2.69)$$

where $V_h(n)$ is the heater voltage set at the n -th operation, $V_{\text{in}}(n)$ is the output of the pyroelectric detector at the n -th measurement, K_P is a proportional gain, K_I is an integral gain, and $V_{\text{in}}^{\text{target}}$ is a target voltage. In this experiment, K_P is set to

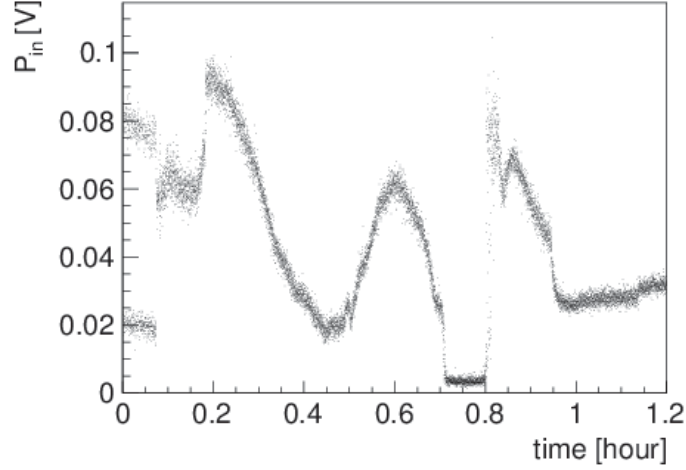


Figure 2.27: Time variation of the gyrotron output power is very large unless the feedback system is installed.

100 and K_I is set to 0.05 (Typical voltage : $V_h \sim 200$ V, $V_{in} \sim 0.2$ V). Figure 2.28 is a monitor plot of the gyrotron output power and the heater voltage with this stabilization system. The gyrotron output power is stable within ± 10 %.

Stabilization of the resonance of the Fabry-Pérot resonant cavity

We control the cavity length to keep it resonant with the Gaussian beam. The cavity length is varied without moving the piezoelectric X-stage due to the fluctuation of the temperature of the gas chamber made of aluminum. The coefficient of thermal expansion of aluminum is 2.3×10^{-5} /K, and the length of the surface where the Fabry-Pérot cavity is mounted is 562 mm. The temperature fluctuation of ± 0.05 K results in ± 0.6 μm (± 1 ppm) fluctuation of the length of aluminum, which unstabilizes resonance of the Fabry-Pérot cavity. Note that 0.6 μm is equal to the HWHM (Half Width at Half Maximum) of the resonance peak of the Fabry-Pérot cavity. The resonance of the Fabry-Pérot cavity lasts for a few minutes even if the cavity length is not controlled. We rescan the cavity length searching resonance peak position only when the transmitted power of the Fabry-Pérot cavity falls below a threshold.

The rescan procedure is as follows. Figure 2.29 is its schematic.

1. If V_{tr} gets less than V_{thr}^{high} , rescan process starts and the cavity length is lengthened until V_{tr} gets less than V_{thr}^{low} .
2. We shorten the cavity length until V_{tr} gets less than V_{thr}^{low} of the other side of

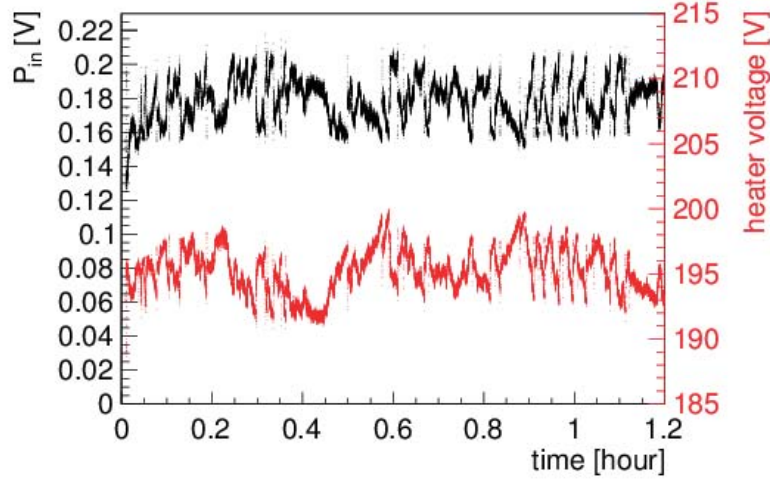


Figure 2.28: Stabilization of the input beam power by controlling heater AC voltage.

the resonance curve, while searching the peak of it.

3. The cavity length is set at the peak position found in the 2nd step.

The 1st step is necessary since we can not figure out in which side of the resonance curve the cavity is.

Figure 2.30 is a monitor plot of the transmitted power and the displacement of the piezoelectric stage. The cavity rapidly returns to the resonance when resonance breaks. The rescan threshold $V_{\text{thr}}^{\text{high}}$ is 80 % of the peak power.

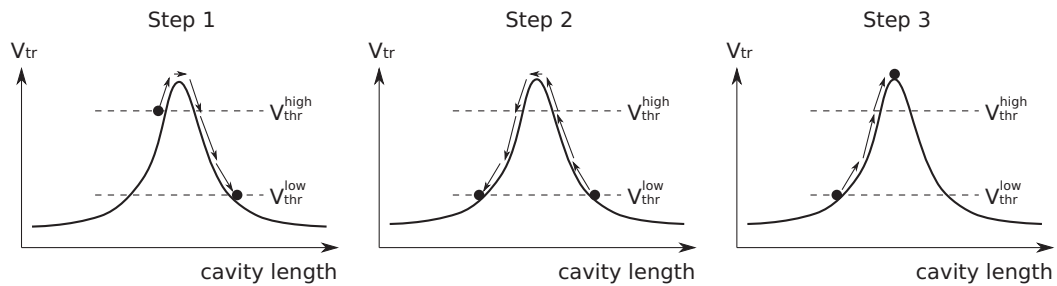


Figure 2.29: Schematic of the rescan procedure.

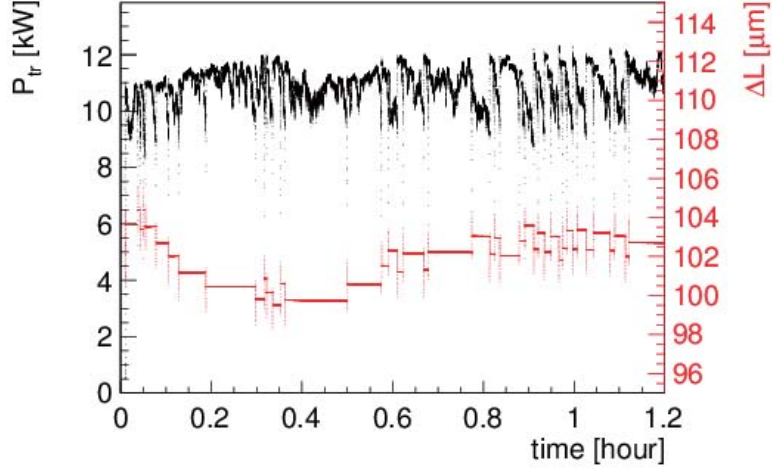


Figure 2.30: Control of the cavity length to keep resonance of the Fabry-Pérot cavity.

2.3 Positronium Assembly and γ -ray Detectors

Figure 2.31 is a top view of the positronium assembly chamber and the γ -ray detectors. A positronium atom is formed when a positron stops in the mixed gas (1.9 atm nitrogen (N_2) and 0.1 atm isobutane ($i-C_4H_{10}$)). The gas is filled and the positron source is placed in the sealed chamber. The Fabry-Pérot cavity is also placed in the chamber. The Gaussian beam enters the chamber passing the window made of high-resistive Si. We select high-resistive Si since it prevents light whose wavelength is smaller than $1.2 \mu\text{m}$ entering the chamber and is enough rigid (bending strength $\sim 80 \text{ MPa}$) to fill 2 atm of the mixed gas in the chamber. However, the refractive index is large ($n = 3.4$ [25]). The transmittance of an optical parallel of thickness d cm, absorption coefficient $\alpha \text{ cm}^{-1}$, and refractive index n is

$$T = \frac{(1 - R)^2}{(1 - Re^{-2\alpha d})^2 + 4Re^{-4\alpha d} \sin^2 kd}, \quad (2.70)$$

where $R = \left(\frac{1 - n}{1 + n}\right)^2$ is a one-side reflectivity. We optimize the thickness of the window to maximize the transmittance for 202.9 GHz radiation. The thickness of the Si window is 1.96 mm (measured) and the transmittance is measured $98 \pm 2 \%$. Four γ -ray detectors are placed 25 mm away from the beam axis, which is the shortest distance so that the γ -ray detectors do not interrupt the resonance of the Fabry-Pérot cavity.

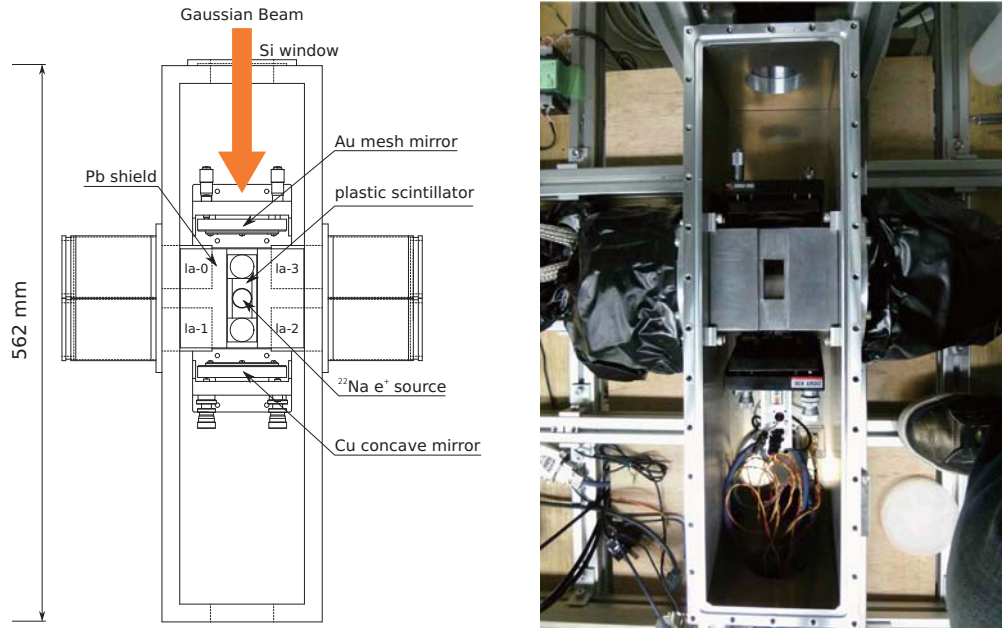


Figure 2.31: A schematic and a picture of the positronium assembly chamber and γ -ray detectors. The plastic scintillator and the ^{22}Na source is not placed in the right picture.

2.3.1 Positronium Formation Assembly

Positronium formation assembly used in this experiment is shown in Fig. 2.32. Intensity of the ^{22}Na positron source (Eckert & Ziegler POSN-22) is approximately 780 kBq. Since the radioactive half-life of ^{22}Na is 950.8 days, the decrease of the event rate is only 1.5 % during the experiment. The decay scheme of the ^{22}Na is shown in Fig. 2.33.

The ^{22}Na positron source is titanium packaged and 19.1 mm in diameter and has an active diameter of 9.53 mm. The activity is placed between two layers of 0.0051 mm titanium foil, supported by two 0.25 mm titanium disks. This assembly is sealed by electron beam welding.

Positrons are emitted from the ^{22}Na source, which is placed 47 mm away from the beam axis. Positrons emitted toward the beam direction pass a thin (100 μm) plastic scintillator (OKEN NE-102). The characteristics of the plastic scintillator are summarized in Table 2.4. About 88 % of the positrons annihilate into two γ rays around the source, and these γ rays become source of accidental background. In order to block such γ -rays, the source and the plastic scintillator are surrounded by a 15 mm Pb shield. The light of the scintillator is collected by a light guide made of PMMA and two $1\frac{1}{2}$ -inch fine-mesh photomultipliers (HAMAMATSU R5924-70) to tag e^+ emissions. The characteristics of these PMTs is summarized in Table 2.5.

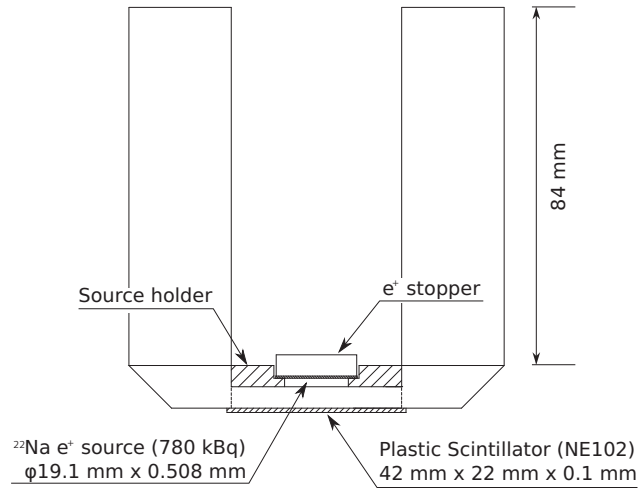
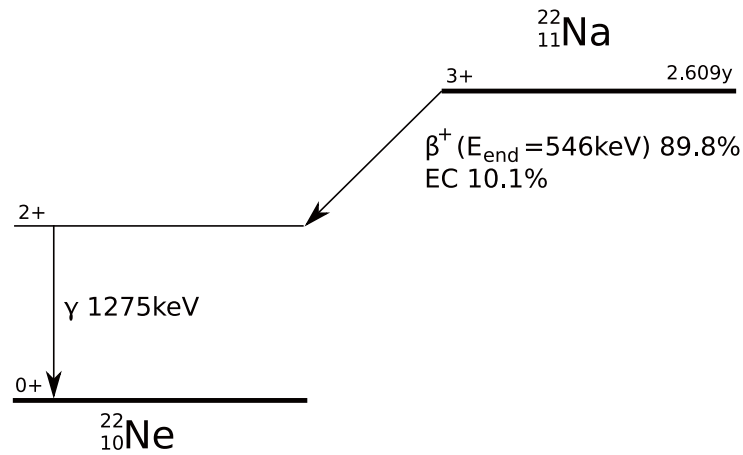


Figure 2.32: A schematic of the positronium formation assembly

Figure 2.33: The decay scheme of the ^{22}Na isotope

Light output [% of NaI(Tl)]	29
Primary decay time [ns]	2.4
Density [g/cm^3]	1.03
Wavelength of emission max [nm]	423
Refractive index	1.58
Melting point [$^{\circ}\text{C}$]	75

Table 2.4: Properties of NE-102 (plastic) scintillator.

Size	$\phi 51$ mm
Active diameter	$\phi 39$ mm
Dynode type	Fine mesh (19 stages)
Wavelength	300 - 650 nm (peak 420 nm)
Typical HV	2000 V
Typical gain	1×10^7
Typical Q.E.	20 %
Rise time	2.5 ns
Transit time	9.5 ns

Table 2.5: Properties of the PMT (HAMAMATSU R5924-70).

The fine-mesh PMT is used because there is remaining magnetic field (0.5 - 1.0 mT) of the superconducting magnet of the gyrotron. About 5 % of the positrons are tagged by the plastic scintillator and stop in the gas. The others stop at materials around the source or are too energetic to stop in the gas and annihilate at the wall of the chamber.

2.3.2 Characteristics of Mixed Gas

We use the mixed gas of nitrogen 1.9 atm and isobutane 0.1 atm as a source of electron to form positronium. The mixing ratio is determined to satisfy following conditions. Details are also given later.

1. Slow positron annihilation becomes negligible.
2. Absorption of 203 GHz radiation becomes small enough.
3. The formation rate of positronium becomes as high as possible.
4. The stopping power for positron becomes as high as possible.

The condition 3. and 4. is equal to as much isobutane as possible.

Slow positron annihilation

A positron, whose energy is under the first ionization energy of a gas molecule, can not form a positronium any more, and is called slow positron. When such a positron collides with an electron of the gas molecule, pair-annihilation occurs. The rate of the slow positron annihilation is expressed as

$$\lambda_{\text{slow}} = \pi r_0^2 c n Z_{\text{eff}} = 0.201 \rho Z_{\text{eff}} \mu\text{s}^{-1} \quad (2.71)$$

where r_0 is the classical electron radius, c is the speed of light, n is number density of the gas molecule, and Z_{eff} is the effective number of electrons per gas molecule

[26]. ρ is the gas density in amagat, which is defined as the number of ideal gas molecules per unit volume at 1 atm and 0 °C. Gas of P [atm] and T [°C] is

$$\rho = P \cdot \frac{273.15}{273.15 + T} \text{ [amagat]} \quad (2.72)$$

Nitrogen gas does not absorb 203 GHz radiation at all but $Z_{\text{eff}}(\text{N}_2)$ is small ($Z_{\text{eff}}(\text{N}_2) = 29.75(85)$ [27]), therefore $\lambda_{\text{slow}}(\text{N}_2) = 11.96(31) \mu\text{s}^{-1}$ and the lifetime is long ($\tau_{\text{slow}}(\text{N}_2) = 91.3(2.6)$ ns) in nitrogen gas at 2 atm and 25 °C. In this case, the slow positron annihilation becomes serious background since the lifetime of the slow positron annihilation in nitrogen gas at 2 atm is comparable to that of o-Ps. On the other hand, isobutane absorbs 203 GHz radiation but it is a good quencher of the slow positron because its Z_{eff} is very large ($Z_{\text{eff}}(\text{iso}) = 14400$ [28]). In the mixed gas of nitrogen at ρ_{N_2} amagat and isobutane at ρ_{iso} amagat, the rate of the slow positron annihilation λ_{slow} is expressed as

$$\lambda_{\text{slow}} = 0.201(\rho_{\text{N}_2} Z_{\text{eff}}(\text{N}_2) + \rho_{\text{iso}} Z_{\text{eff}}(\text{iso})) \quad (2.73)$$

Figure 2.34 shows the lifetime of the slow positron in the mixed gas at total pressure 2 atm and 25 °C while changing the partial pressure of isobutane. If the partial pressure of isobutane is larger than 0.03 atm, then the lifetime of slow positron becomes smaller than 10 ns.

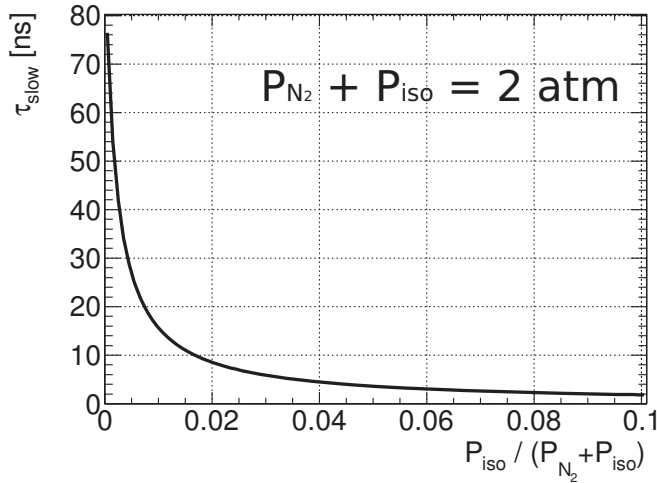


Figure 2.34: The lifetime of the slow positron as a function of the partial pressure of isobutane.

Absorption of 203 GHz radiation in isobutane

Since the sub-THz beam makes many round-trips when the cavity is on resonance, absorption by the gas is not negligible. Figure 2.35 shows transmitted power on the resonance of the Fabry-Pérot cavity while changing the partial pressure of isobutane (total pressure is 1 atm). The graph is fitted by the following function, which is the natural extension of Eq. (2.47),

$$\frac{P_{\text{tr}}}{P_{\text{in}}} = \frac{C_0}{(1 - \sqrt{\rho} + 1 - \exp(-\alpha p_{\text{iso}} L))^2} \quad (2.74)$$

where α is the absorption coefficient of isobutane at 1 atm, L is the cavity length (136 mm) and p_{iso} is the pressure of isobutane. If the graph is fitted by fixing the round-trip reflectivity $\rho = 0.9899(5)$ (or $\mathcal{F} = 623 \pm 29$) in order to obtain the absorption coefficient, $\alpha = 2.41(50) \times 10^{-4} [\text{cm}^{-1}]$ at 1 atm (Fig. 2.35). If the

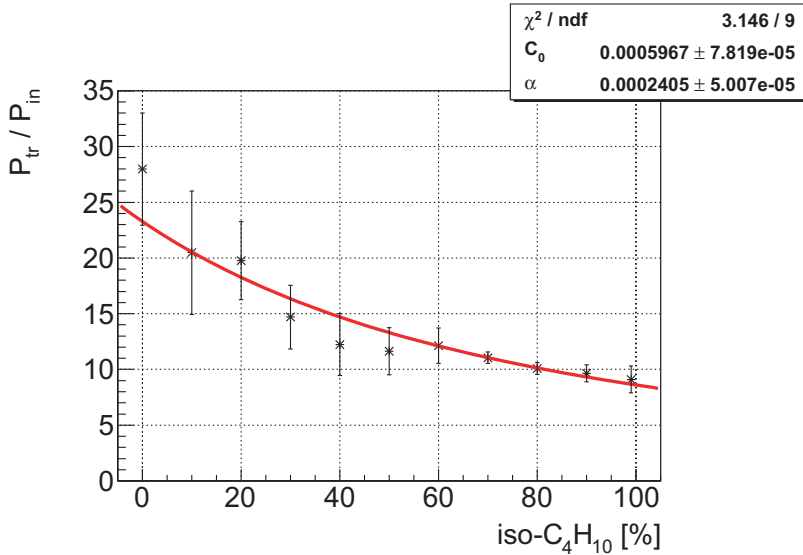


Figure 2.35: Absorption of sub-THz radiation by isobutane.

partial pressure of isobutane is less than 0.1 atm, the loss of the accumulated power is less than 20 %.

Considering both of the lifetime of slow positron annihilation and the absorption, we selected the mixed gas of nitrogen 1.9 atm and isobutane 0.1 atm.

2.3.3 γ -ray Detectors

Four $\text{LaBr}_3(\text{Ce})$ inorganic scintillators (Saint-Gobain Crystals, BrillanCeTM 380) are used to detect γ rays from decay of Ps. $\text{LaBr}_3(\text{Ce})$ detector has good energy resolution ($\text{FWHM} = 4\%$ at 511 keV), which is good advantage to search

monochromatic 511 keV γ rays. In addition, its fast time response ($\tau = 16$ ns) is appropriate for high statistics experiment. The characteristics are summarized in Table 2.6.

Light yield [photons/keV γ]	63
Primary decay time [ns]	16
Density [g/cm ³]	5.08
Wavelength of emission max [nm]	380
Refractive index @ emission max	1.9
Thickness for 50 % attenuation (662 keV) [cm]	1.8

Table 2.6: Properties of LaBr₃(Ce) scintillator

The LaBr₃(Ce) detectors used in this experiment are ϕ 1.5 inch \times 2.0 inch large crystal. The crystals are covered with aluminum housing (0.5 mm thick). They are connected to 1.5 inch photomultipliers (HAMAMATSU R5924-70). Four LaBr₃(Ce) detectors are arranged to make four back-to-back pairs as shown in Fig. 2.36.

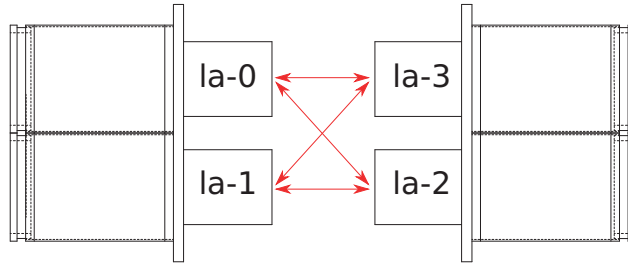


Figure 2.36: Four γ -ray detectors are arranged to make four back-to-back pairs. The pairs are (la-0, la-2), (la-0, la-3), (la-1, la-2), and (la-1, la-3).

2.4 Electronics and Data Acquisition

Data flow

The data acquisition system of the experiment consists of two parts, the detector part and the optics part. The detector part acquires the data concerning the transition signal and consists of the clusters of NIM standard modules and the CAMAC system. The optics part controls the optical system and monitors the condition of the experiment (power, temperature, pressure, gyrotron parameters, position of the piezoelectric stage, etc.). It consists of a data logger (HIOKI 8420-50), the piezoelectric X-stage (NANO CONTROL TS102-G), the pyroelectric detectors, and the

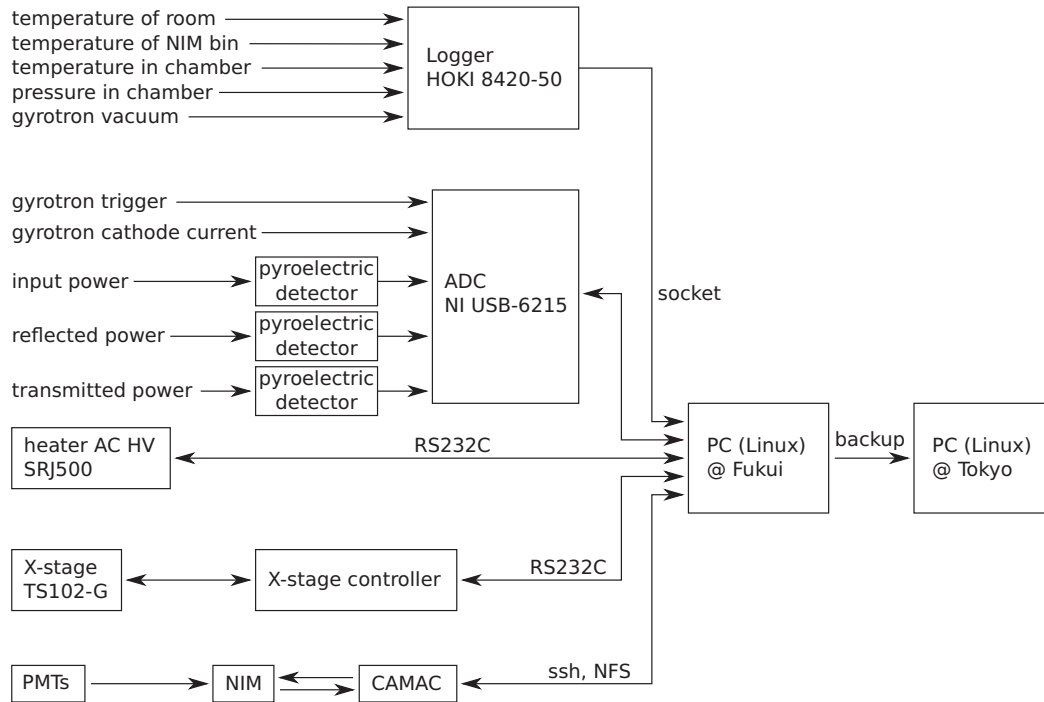


Figure 2.37: The schematic view of the whole DAQ system.

ADC (National Instruments NI USB-6215). Figure 2.37 is a schematic view of the whole DAQ system.

First of all, the gyrotron output power is stabilized by controlling the heater voltage of the electron gun. The AC voltage of the heater is supplied by Matsusada Precision SRJ500 and its output voltage is remote-controlled from the PC via RS232C. Once the gyrotron output power becomes stable, then the resonance peak of the Fabry-Pérot cavity is searched by moving the piezoelectric stage, whose driver is connected to the PC via RS232C. The cavity length is controlled so that the cavity can stay on resonance. Then the PC sends a start command to the CAMAC controller (Toyo Corp. CC/NET). At first, all the CAMAC modules are cleared and the latch is released by the reset signal from the output register. This makes all the systems active and the controller waits the interrupt signal, so-called LAM (Look-At-Me) signal from the CAEN ADC (CAEN C1205). The interrupt signal comes only when the main trigger condition is satisfied. The data acquisition is triggered when back-to-back γ -ray signals from the $\text{LaBr}_3(\text{Ce})$ scintillators are coincident within 40 ns and then when this coincidence is within -100 ns to 1100 ns of the timing of the plastic scintillators. A charge ADC (CAEN C1205) is used to measure the energy information of the $\text{LaBr}_3(\text{Ce})$ detectors, a charge ADC (PHILLIPS 7167) and a charge ADC (REPIC RPC-022) are used to measure the energy information of the plastic scintillator. The time information of the plastic and $\text{LaBr}_3(\text{Ce})$ scintillators is recorded using a direct clock (2 GHz) count type

TDC (KEK GNC-060). After the reading procedures, the controller saves the data through NFS and starts the next event cycle.

Environmental conditions (temperature, pressure, and gyrotron vacuum) are recorded with the data logger (HIOKI 8420-50). The incident, reflected and transmitted power are monitored with pyroelectric detectors as shown in Fig. 2.26. The signal waveform of the pyroelectric detectors are read with an ADC (NI USB-6215). The trigger pulse for the gyrotron output and the level of the cathode current of the gyrotron are also recorded with the ADC. These data per gyrotron output pulse are recorded to the PC.

In the following subsections, details of the detector part are described.

Electronics for the plastic scintillator

A schematic diagram of electronics for the plastic scintillator is shown in Fig. 2.38.

The photomultipliers for the plastic scintillator are operated at +2215 V (ps-0) and +2250 V (ps-1). These high voltage are supplied by a positive high voltage module (REPIC RPH-022). Their gains are 3.4×10^7 and 3.8×10^7 .

The output of the plastic scintillator PMT is divided into three lines by a linear fanout module. One of the divided signals is fed into a discriminator. The others are used to measure the amplitude of the signal with short (60 ns) and long (1000 ns) gate.

The threshold value is set to 25 mV, which corresponds about 1 p.e. One of the output of the discriminator is delayed by 200 ns and then provides the stop signal for the TDC (KEK GNC-060).

The other output is used to make a coincidence signal of the two PMTs (ps-and). The noise is suppressed by requiring the coincidence. The coincidence signal is used to make a common start signal of the TDC (KEK GNC-060), a short gate signal of a charge sensitive ADC (phillips 7167), a long gate signal of a charge sensitive ADC (REPIC RPC-022), the fast clear, and the main trigger. These are described in the explanation of the trigger part.

Electronics for the γ -ray detectors

A schematic diagram of electronics for the γ -ray detectors is shown in Fig. 2.39.

The high voltages of the photomultipliers are supplied by a positive high voltage module (REPIC RPH-022). The HV values are +1310 V for la-0, +1220 V for la-1, +1440 V for la-2, and +1270 V for la-3.

The output of the γ -ray detector PMT is divided into two lines by a linear fanout module. One of the divided signals is fed into a discriminator. The other is used to measure the amplitude of the signal with a charge sensitive ADC (CAEN C1250). The gate width is 150 ns. The pulse height of the 511 keV signal is about 0.9 V. The threshold value is set to 90 mV, which corresponds about 50 keV.

One of the outputs of the discriminator is delayed by 200 ns and then provides the stop signal for the TDC (KEK GNC-060). The other outputs of the four

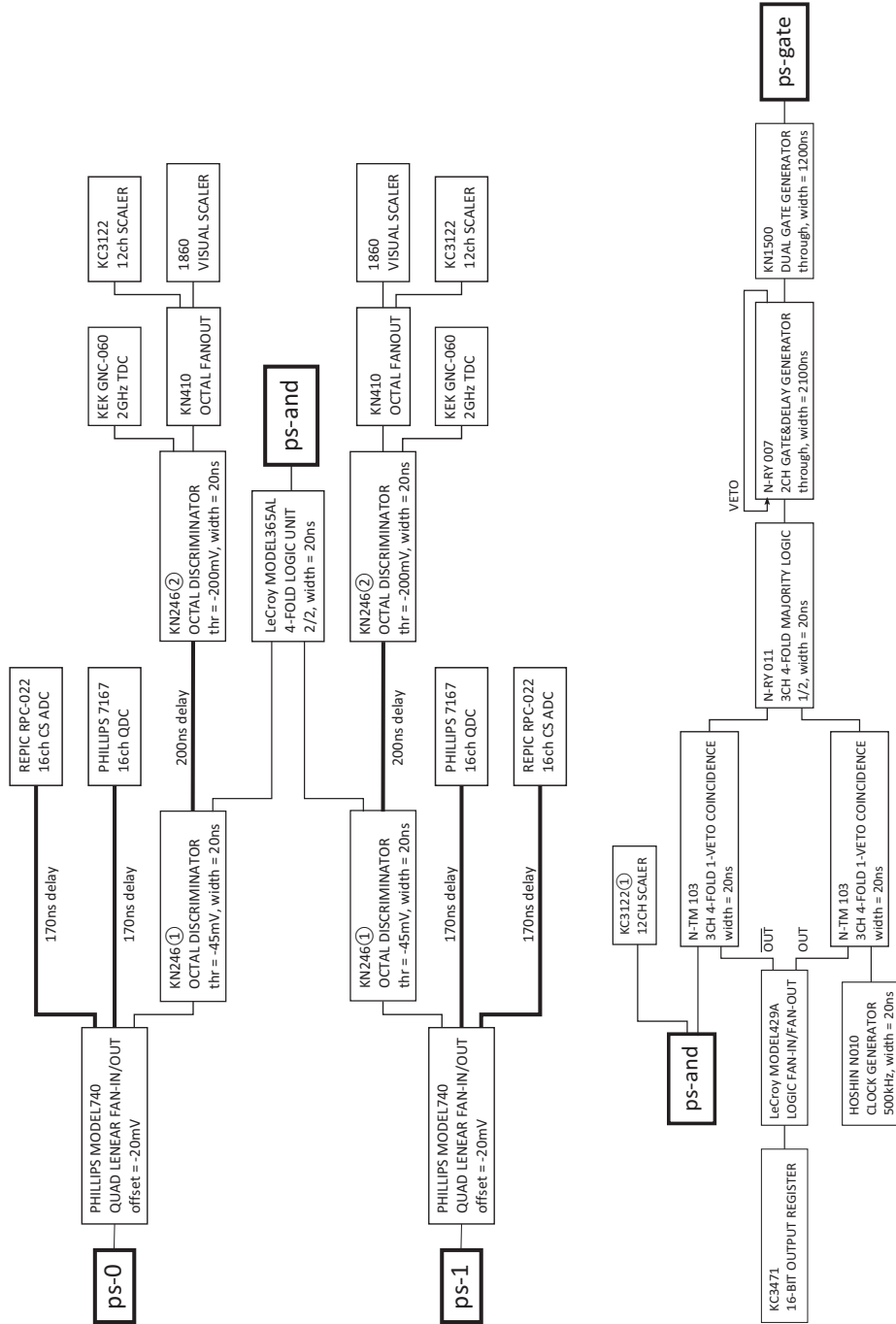


Figure 2.38: Schematic diagram of electronics for plastic scintillator system.

discriminators are fed by a logic fan-in/fan-out module and a logic unit, and the output of the logic unit is the back-to-back coincidence signal of the four γ -ray detectors (1a-b2b). The 1a-b2b signal is used to make a gate signal of a charge sensitive ADC (CAEN C1205) to record the energy information of the $\text{LaBr}_3(\text{Ce})$ detectors and the main trigger. These are described in the explanation of the trigger part.

Electronics for the trigger system

A schematic diagram of electronics for the trigger system is shown in Fig. 2.40.

The coincidence signal from the two plastic scintillator PMTs (ps-and) is widened to 1200 ns (ps-gate). The 1a-b2b signal is delayed by 100 ns, and when the delayed signal coincides with ps-gate, then the data acquisition is triggered (main trigger). The main trigger is also the gate signal of the charge sensitive ADC (CAEN C1205) to record the energy information of the $\text{LaBr}_3(\text{Ce})$ detectors. The trigger signal works also as the latch start. The latch signals veto the second gate signals and the fast clear signals. After all the data are read and saved, the latch reset signals are produced by an output register.

On the other hand, the short and long gate signals for the ADCs which record the energy information of the plastic scintillator is produced as long as the signals from the two PMTs of the plastic scintillator are coincident within 40 ns. Though the coincidence rate is very high (about 200 kHz), the data are cleared by the clear signal (fast clear) unless the main trigger signal is produced.

In the same way, the coincidence signal from the two PMTs of the plastic scintillator is the common start signal for the TDC. The TDC data is also cleared by the fast clear signal unless the main trigger signal is produced.

Data summary

The quantities recorded at the main trigger timing are summarized in Table 2.7, and the quantities recorded in synchronization with the gyrotron output pulse are summarized in Table 2.8.

2.5 Monte Carlo Simulation

In this experiment, a Monte Carlo simulation is used to estimate the transition probability and the systematic error because the ratios of the 3γ detection efficiency and the 2γ detection efficiency for the $\text{LaBr}_3(\text{Ce})$ scintillators are necessary.

For the detector simulation, the Geant4 (ver. 4.9.3) package [29] is used and the details of the experimental setup (Fig. 2.41) are reproduced in the simulation. In this package, the interaction of e^\pm and γ -rays in various materials are implemented. Practically, the Penelope low-energy electromagnetic models for e^\pm and γ -rays are used.

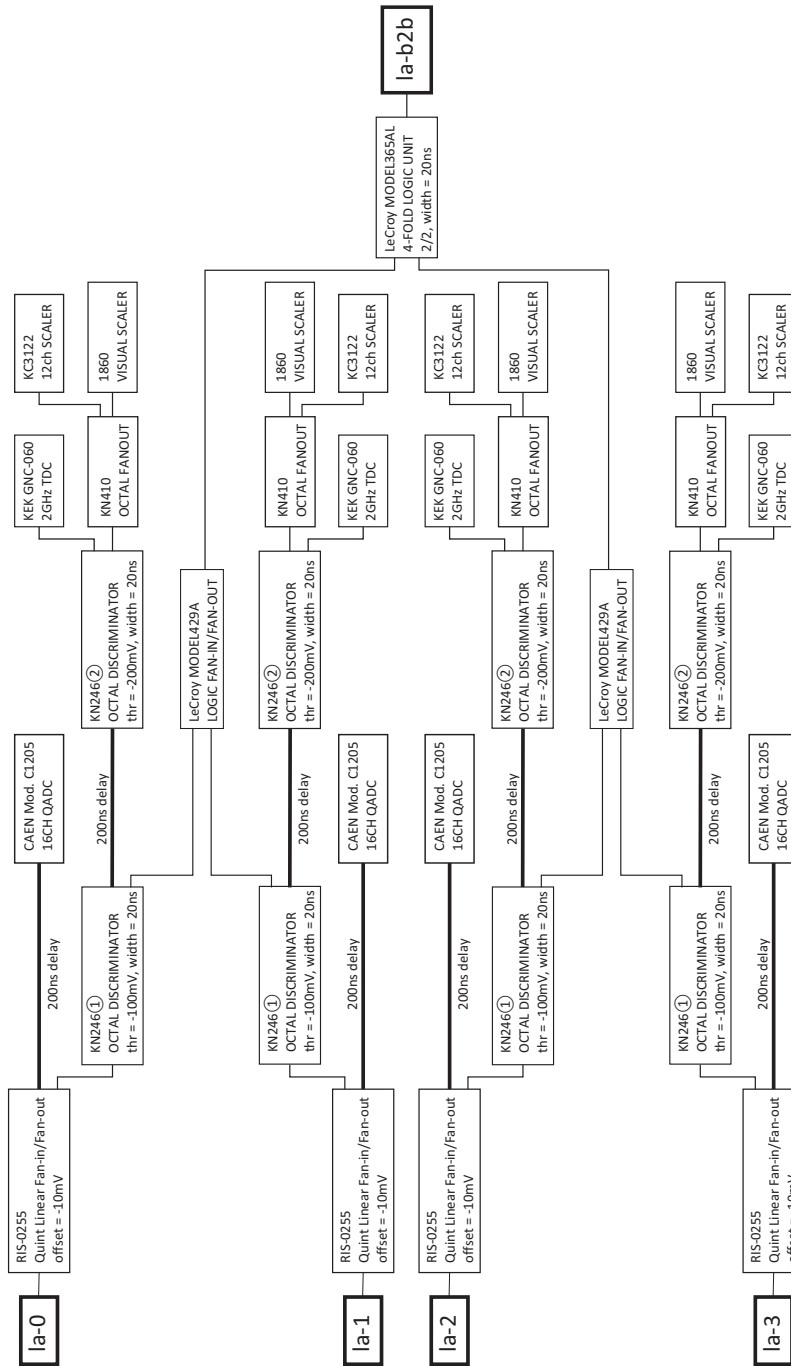


Figure 2.39: Schematic diagram of electronics for γ -ray detector system.

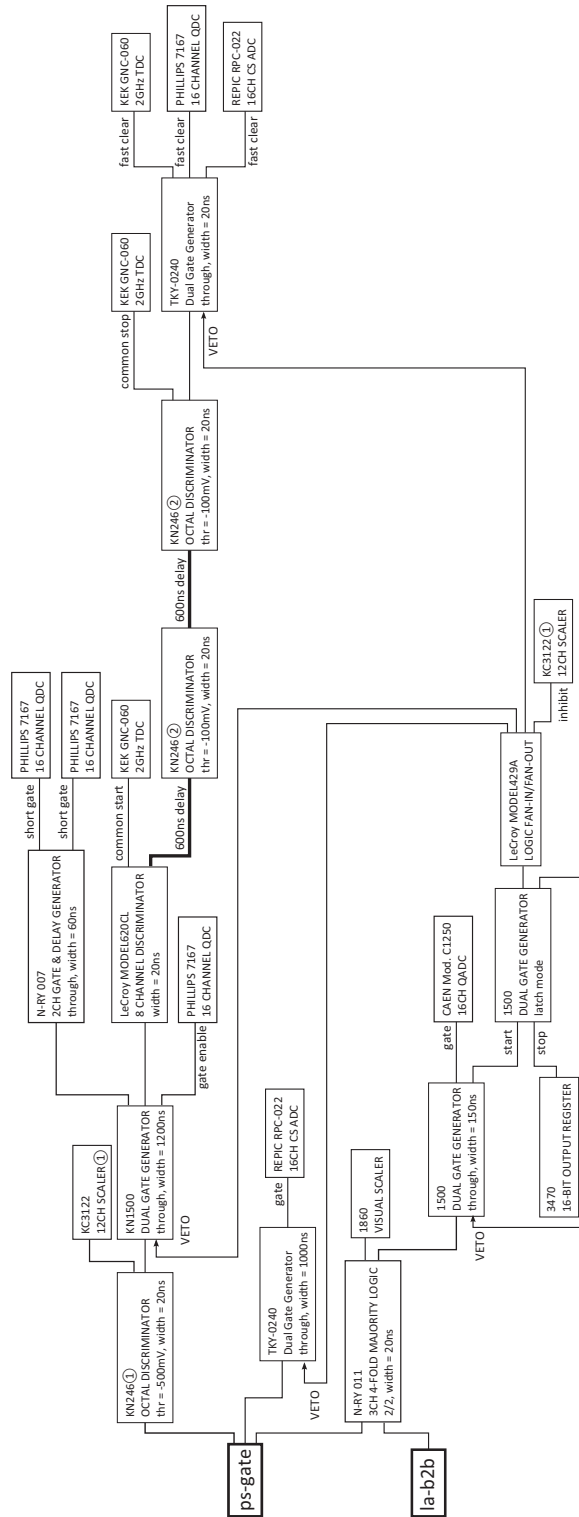


Figure 2.40: Schematic diagram of electronics for trigger system.

name	module
event ID	-
real time	-
gyrotron ON/OFF	input register (LeCroy C005)
ps-energy (short gate), 2ch	CS ADC (phillips 7167)
ps-energy (long gate), 2ch	CS ADC (REPIC RPC-022)
la-energy, 4ch	CS ADC (CAEN C1205)
ps-time, 2ch	TDC (KEK GNC-060)
la-time, 4ch	TDC (KEK GNC-060)
live time	SCALAR (Kaizu KC3122)
ps-rate, 2ch	SCALAR (Kaizu KC3122)
ps-and-rate	SCALAR (Kaizu KC3122)
la-rate, 4ch	SCALAR (Kaizu KC3122)

Table 2.7: Quantities measured at the main trigger timing.

name	device
input power	pyroelectric detector
reflected power	pyroelectric detector
transmitted power	pyroelectric detector
trigger pulse of gyrotron	ADC (NI USB-6215)
cathode current of gyrotron	ADC (NI USB-6215)
heater voltage of gyrotron	-
vacuum of gyrotron	logger (HIOKI 8420-50)
cavity length	NANO CONTROL TS102-G
room temperature	logger (HIOKI 8420-50)
temperature of NIM bin	logger (HIOKI 8420-50)
temperature in the Ps assembly chamber	logger (HIOKI 8420-50)
pressure in the Ps assembly chamber	logger (HIOKI 8420-50)

Table 2.8: Quantities measured in synchronization with the gyrotron output pulse

The Monte Carlo simulation is proceeded as follows. At first, a positron is emitted from the source with the energy corresponding to the energy spectrum of ^{22}Na . Then the interactions of the positron in the materials are simulated step by step. The simulation of the secondary particles is also included in this process. The positrons which stopped in the gas are selected as the candidate for Ps.

The next step is the simulation of the γ rays emitted from Ps. For the simulation of the 2γ annihilation, back-to-back γ rays with the energy of 511 keV are emitted toward in a random direction from the point where the positron stopped in the positron simulation. The 3γ annihilation from the o-Ps decay are also generated in the same manner, but their direction and the energy are calculated from the $O(\alpha)$ matrix element [30]. Then, the interactions of all the γ rays and their secondary particles are simulated step by step.

In the end, the energies deposited on the $\text{LaBr}_3(\text{Ce})$ scintillators and the plastic scintillator are obtained for o-Ps $\rightarrow 3\gamma$ (normal 3γ decay), o-Ps $\rightarrow 2\gamma$ (pick-off annihilation), and o-Ps \rightarrow p-Ps $\rightarrow 2\gamma$ (stimulated emission). The obtained energies are smeared by the measured resolutions of the corresponding detectors.

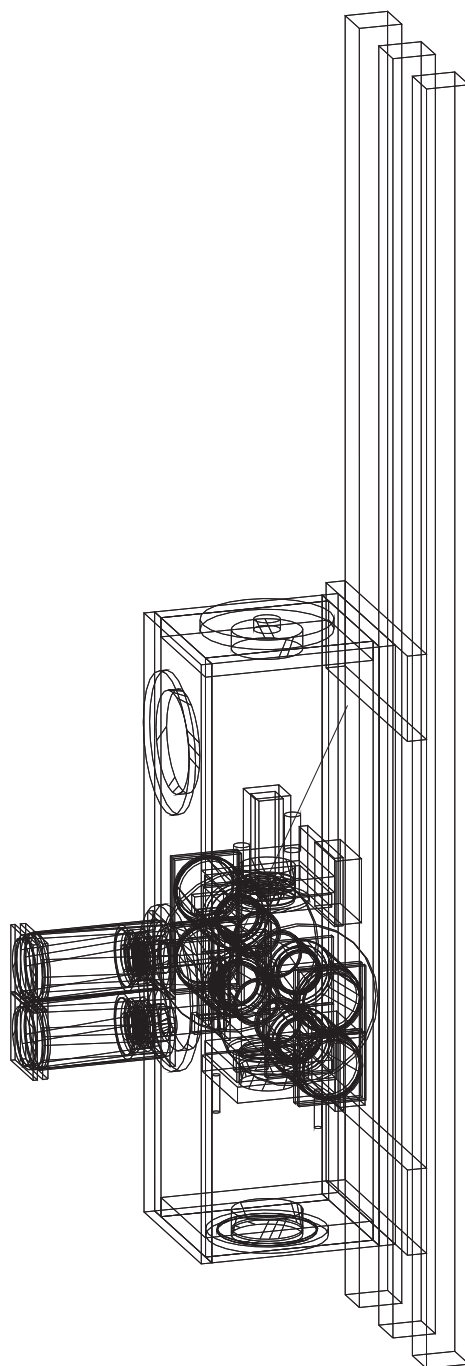


Figure 2.41: Geometry of the Monte Carlo simulation.

Chapter 3

Analysis

The details of the analysis are described in this chapter. First, data sets are described. Calibration, several cuts, time walk correction and charge leak correction are explained in Sec. 3.2. The detailed description of the event selections to select the transition events will follow. In the next section, the systematic errors are discussed in Sec. 3.4. Finally, the result of this experiment is shown.

3.1 Data Sets

Four RUNs have been performed and detail information of the four RUNs are summarized in Table 3.1. Most of the parts are the same, but the accumulated power and the radiation frequency are different. RUN I, III and IV use 202.9 GHz radiation (TE_{03} mode) and they are different in accumulated power in the Fabry-Pérot resonant cavity. RUN I is the most high power RUN and the accumulated power is 11.0 kW in the average during the DAQ. The accumulated power of 11.0 kW corresponds to the peak intensity of 8.3×10^7 W/m² and the peak energy density of 0.28 J/m³ at the center of the Fabry-Pérot resonant cavity. RUN IV is operated at about half power of RUN I, and RUN III is the power OFF data by not resonating the Fabry-Pérot cavity. RUN II is the off-resonance data and uses 140 GHz radiation (TE_{02} mode) by setting the magnetic field strength to about 5.07 T to check systematic uncertainties due to the absorption of the radiation in the mixed gas.

The pulse frequency of the gyrotron output used in the four RUNs is 20 Hz and the duty cycle is 30 % as shown in Fig. 3.1. We measure the transition signal by comparing the data during “beam ON” and “beam OFF”. Duration of total data taking and live time during “beam ON” and “beam OFF” are summarized in Table 3.1. The duration of data taking and the live time are not proportional because the data acquisition is not performed when the Fabry-Pérot cavity is out of resonance (except for RUN III, which is non-resonance RUN).

Data are stored into the multiple calibration units for every 30 minutes. The calibration, some corrections, and offline trigger cuts described in the next section

are carried out within one calibration unit. Since the data taking time for one unit is only 30 minutes, it is guaranteed that the fluctuation and the shift of the measured quantities by the environment do not propagate over that time scale. During the measurements, the temperature of the experimental area is controlled within ± 1.3 °C to suppress the fluctuation of the measured quantities due to the electronics. The difference of the trigger rate is due to the difference of alignment of the source and Pb shield, the pressure and the temperature of the mixed gas.

Gyrotron output : 20 Hz, duty 30 %

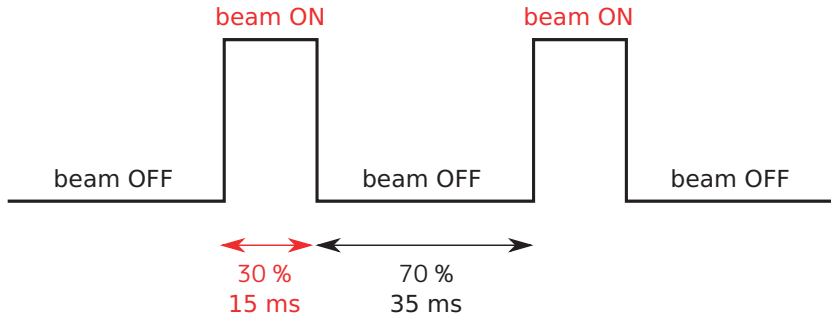


Figure 3.1: The timing diagram of the gyrotron output. The pulse frequency is 20 Hz and the duty ratio is 30 %.

ID	frequency	power	duration	live time (ON)	live time (OFF)	trigger rate
I	203 GHz	11.0 kW	4.3 days	7.0×10^4 sec	1.6×10^5 sec	949 Hz
II	140 GHz	3.3 kW	3.3 days	4.3×10^4 sec	1.0×10^5 sec	949 Hz
III	203 GHz	0.0 kW	2.4 days	4.1×10^4 sec	9.6×10^4 sec	936 Hz
IV	203 GHz	5.6 kW	2.8 days	3.8×10^4 sec	8.9×10^4 sec	932 Hz

Table 3.1: Properties of the RUNs

3.2 Calibration and Basic Cut

In this section, the energy and time calibration, some corrections, and offline trigger cut are described. They are carried out within one calibration unit per 30 minutes, and the “beam ON” data and the “beam OFF” data are processed separately because there is a difference (less than 2 %) in the width of the pedestal peak between “beam ON” data and “beam OFF” data due to the electrical noise coincident with the gyrotron output pulse.

3.2.1 Energy Spectrum of the Plastic Scintillator

Energy spectra of the plastic scintillator are calibrated in the number of photoelectrons by the gain of the PMTs. The left figure of Fig. 3.2 shows the spectrum measured with long-gate (ps-0) versus that measured with short-gate (ps-0). The charge in collection of the short-gate energy depends on the amplitude and must be corrected to obtain the intrinsic amplitude because the difference of energies of short-gate and long-gate is used for accidental rejection. The correction for short-gate energy is as follows. At first, the short-gate energy range from 15 p.e. to 45 p.e. is divided into 5 p.e. width regions and the long-gate energy spectra for these regions are fitted with Landau distribution. The long-gate energy spectra for the regions where the short-gate energy is less than 15 p.e. are not used to determine the correction curve, since there are many accidental events and it is difficult to find the peak position without accidental events. Then, the most probable energy loss values are fitted with second order polynomial functions as in the left figure of Fig. 3.2. The short-gate energy is corrected with this function. The right figure of Fig. 3.2 shows the 2D energy distribution after this correction.

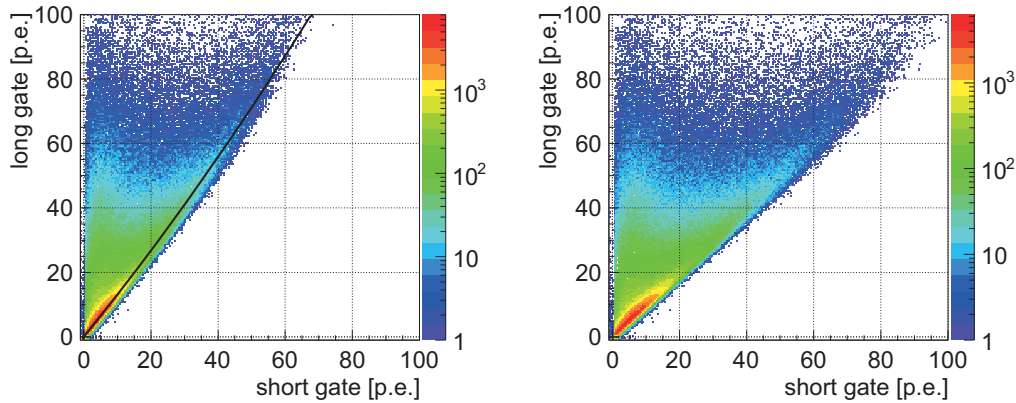


Figure 3.2: Plastic scintillator energy with long-gate vs that with short-gate. (left) before the correction of short-gate charge in collection, (right) after the correction

3.2.2 Energy Spectrum of the $\text{LaBr}_3(\text{Ce})$ Scintillator

The calibration of the ADC spectra has made use of the pedestal line and the 511 keV positron annihilation line. Each peak is fitted with normal Gaussian function. Then the fitted center values are used to determine the energy scale of the ADCs. Figure 3.3 shows energy spectrum measured with one of the $\text{LaBr}_3(\text{Ce})$ scintillators (la-0). The time window is restricted within prompt peak (from -3 ns to 1.5 ns), where positron annihilations are dominant, in order to enhance 511 keV peak. The

absolute time calibration is described in the following two subsections. The energy resolutions of the $\text{LaBr}_3(\text{Ce})$ scintillators are summarized in Table 3.2.

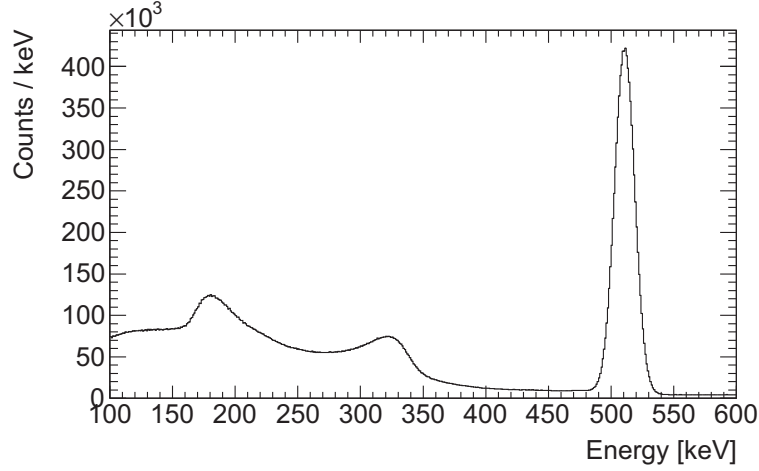


Figure 3.3: Energy spectrum of one of the $\text{LaBr}_3(\text{Ce})$ scintillators (la-0). The time window is restricted within prompt peak (from -3 ns to 1.5 ns).

$\text{LaBr}_3(\text{Ce})$	σ_{ped}	σ_{511}
la-0	0.56 keV	7.99 keV (3.68% FWHM)
la-1	0.57 keV	8.08 keV (3.72% FWHM)
la-2	0.58 keV	9.05 keV (4.17% FWHM)
la-3	0.56 keV	8.29 keV (3.82% FWHM)

Table 3.2: Energy resolutions of the $\text{LaBr}_3(\text{Ce})$ scintillators

3.2.3 Time Walk Correction of the $\text{LaBr}_3(\text{Ce})$ Scintillator

The absolute scale of the KEK TDC is determined by the external clock source. 2 GHz clock leads to 0.5 ns bin width and 32 μs full range. The calibration of the absolute value makes use of the prompt events which appears as a sharp peak and exactly stands at decay time $t = 0$ since it consists of the p-Ps, e^+ annihilation, etc., and at the same time, time walk of $\text{LaBr}_3(\text{Ce})$ scintillator is corrected. Time walk is the lag of detection timings of the signals depending on their amplitudes.

The procedures of the time walk correction for $\text{LaBr}_3(\text{Ce})$ scintillator are as follows. At first, the energy range from 100 keV to 600 keV is divided with a step of 25 keV, and the prompt peak of each region is fitted with normal Gaussian.

The fitted center values of these regions are fitted with a function expressed as $p_0 + p_1/E + p_2E$ as shown in the left figure of Fig. 3.4. The relative correction width is determined by this function at any energy (the left figure of Fig. 3.4).

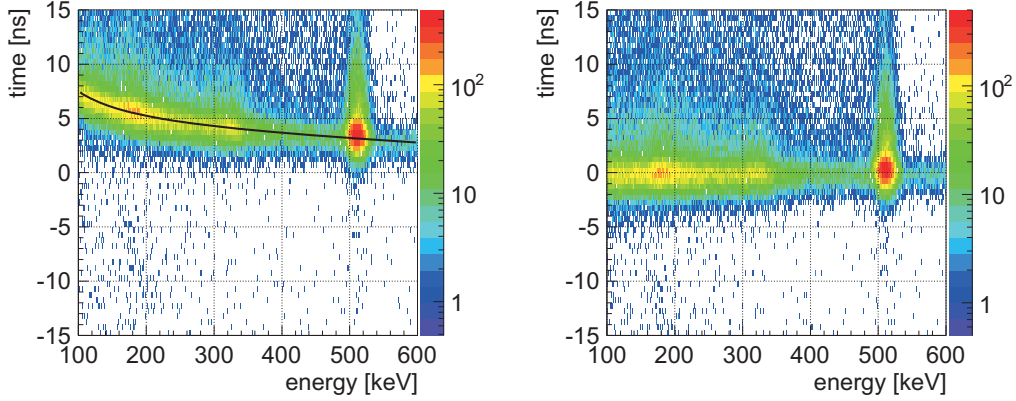


Figure 3.4: The left and the right figure show the scatter plot of timing vs energy deposited on one of the $\text{LaBr}_3(\text{Ce})$ scintillators (la-0) before and after time walk correction, respectively.

3.2.4 Time Walk Correction of the Plastic Scintillator

The time walk of the plastic scintillator is clearly seen in the left figure of Fig. 3.5, though the plastic scintillator has a fast rise-time signal. As in the $\text{LaBr}_3(\text{Ce})$ case, the energy range of the plastic scintillator (ps-0 short + ps-1 short) from 4 p.e. to 100 p.e. is divided into 16 regions and the prompt peaks for these regions are fitted with normal Gaussian. Then, the peak values are fitted with a function expressed as $p_0 + p_1/E + p_2E + p_3/E^2$ as shown in the left figure of Fig. 3.5. The relative correction width is determined by this function at any energy (the right figure of Fig. 3.5).

3.2.5 Offline Trigger Cuts

Offline trigger cuts are applied before main analysis. The offline trigger is similar to the online trigger but requires more strict conditions. This cut is applied to each calibration unit per 30 minutes.

e^+ tagging

To select events such that e^+ hits the plastic scintillator, the following energy selection is applied on the signals of two PMTs placed at the both side of the

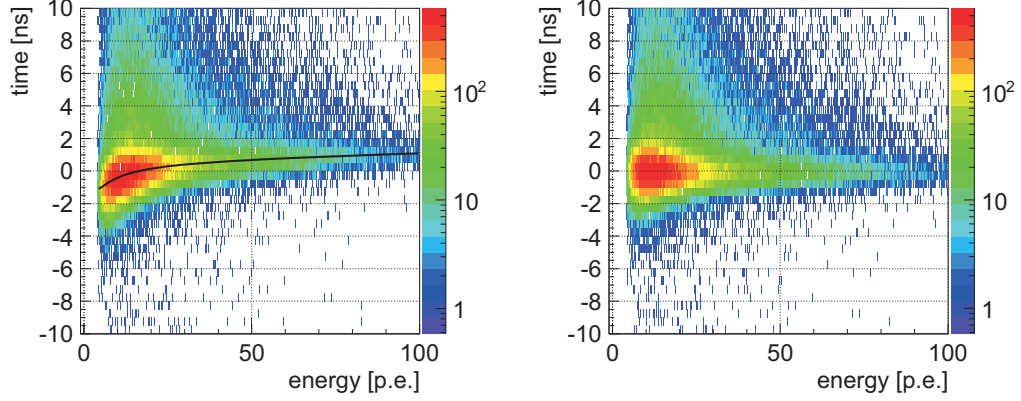


Figure 3.5: The left and the right figure show the scatter plot of timing vs energy deposited on the plastic scintillator before and after time walk correction, respectively.

plastic scintillator (Fig. 3.6). The second cut is the condition on the energy balance, which rejects the events such that e^+ does not hit near the center of the plastic scintillator and cross-talk noise.

- $E_{\text{SG},0}^{\text{ps}} > 2 \text{ p.e.} \ \& \ E_{\text{SG},1}^{\text{ps}} > 2 \text{ p.e.}$
- $\left| \sqrt{E_{\text{SG},0}^{\text{ps}}} - \sqrt{E_{\text{SG},1}^{\text{ps}}} \right| < 3\sigma,$

where $E_{\text{SG},0}^{\text{ps}}$ and $E_{\text{SG},1}^{\text{ps}}$ are the energy deposited on the plastic scintillator measured with short-gate with one PMT (ps-0) and the other PMT (ps-1), respectively. Note that the online threshold for the signals from the two PMTs of the plastic scintillator is 1 p.e.

In addition, we require that the two signals from the plastic scintillator is coincident within $\pm 3\sigma$ ($\sigma = 1.2 \text{ ns}$) (Fig. 3.7).

- $|t_0^{\text{ps}} - t_1^{\text{ps}}| < 3\sigma,$

where t_0^{ps} and t_1^{ps} are the timing of the plastic scintillator hit measured with one PMT (ps-0) and the other PMT (ps-1).

Back-to-back γ -ray hits

To select events such that only two back-to-back γ rays are detected by the $\text{LaBr}_3(\text{Ce})$ scintillators, the following energy selection is applied on the energy of the $\text{LaBr}_3(\text{Ce})$ scintillators.

- $(E_0^{\text{la}} > 100 \text{ keV} \mid E_1^{\text{la}} > 100 \text{ keV}) \ \& \ (E_2^{\text{la}} > 100 \text{ keV} \mid E_3^{\text{la}} > 100 \text{ keV})$

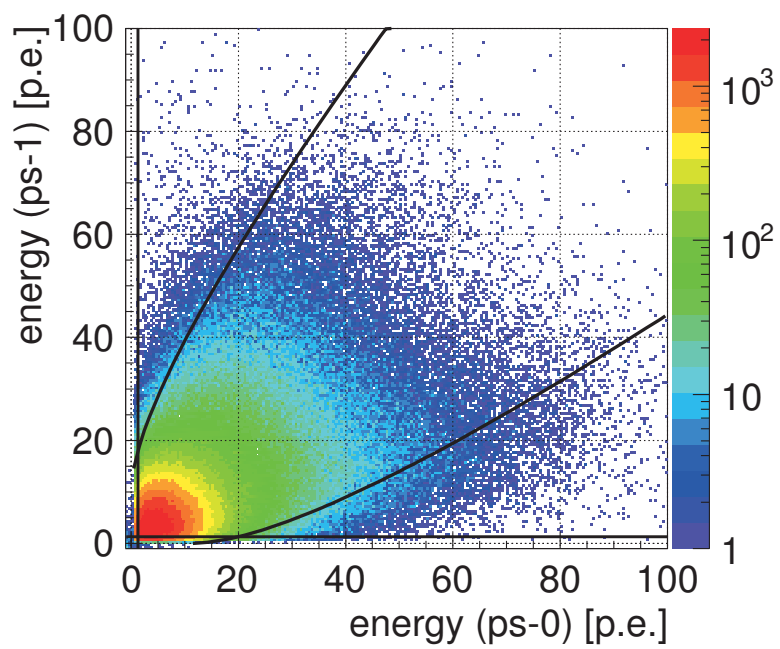


Figure 3.6: ps-1 energy (short-gate) vs. ps-0 energy (short-gate). The energy selection is shown in black line.

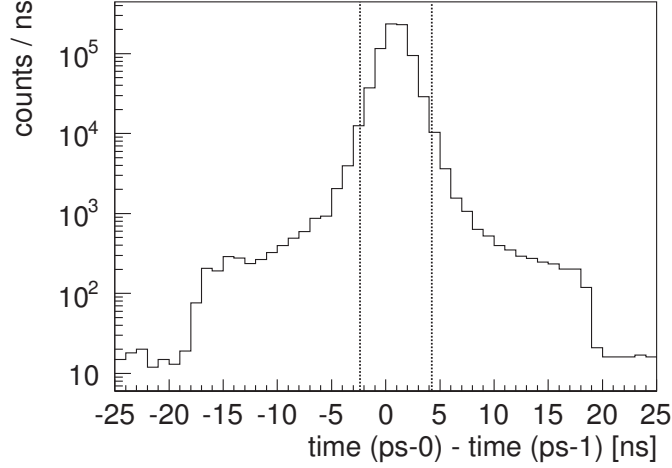


Figure 3.7: Time difference between the ps-1 signal and the ps-0 signal. The coincidence cut region is shown in black dash line.

- $N_{\text{hits}} = 2$

E_i^{la} is the energy deposited on the i -th $\text{LaBr}_3(\text{Ce})$ scintillator. N_{hits} is the number of hits on the $\text{LaBr}_3(\text{Ce})$ scintillators. The offline threshold is 100 keV.

In addition, we require that the timing of two $\text{LaBr}_3(\text{Ce})$ scintillator hits are coincident within $\pm 3\sigma$ ($\sigma = 0.55$ ns) (Fig. 3.8). The two $\text{LaBr}_3(\text{Ce})$ scintillators make a back-to-back pair as shown in Fig. 2.36.

- $|t_i^{\text{la}} - t_j^{\text{la}}| < 3\sigma,$

where t_i^{la} is the timing of the i -th $\text{LaBr}_3(\text{Ce})$ scintillator hit. Note that the coincidence width of the electronics is 40 ns.

Event rates after each selection are summarized in Table 3.3. About 57 % of the online-triggered events pass the offline trigger cuts and there is no difference between “beam ON” and “beam OFF” so far.

3.3 Event Selection

In this section, the signature of the transition signal and the background are described in the first two subsections. Then, event selections to reduce the background are described.

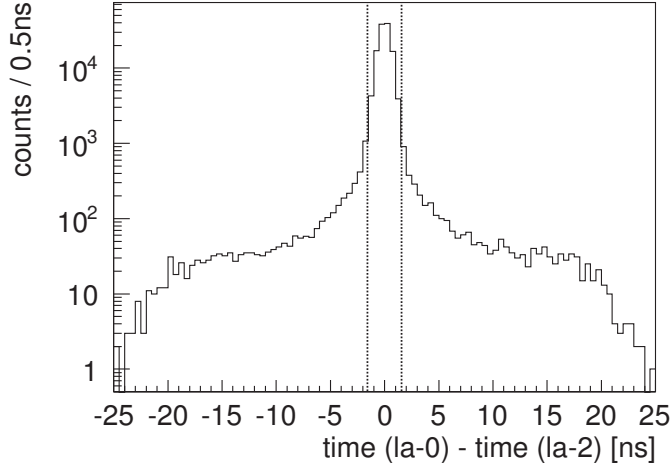


Figure 3.8: Time difference between the back-to-back signals from the $\text{LaBr}_3(\text{Ce})$ scintillators. The coincidence cut region is shown in black dash line.

selection	ON [Hz]	OFF [Hz]
online trigger	948.55(11)	948.59(7)
e^+ tagging : energy cut	771.75(10)	771.94(7)
e^+ tagging : time coincidence	724.90(10)	724.97(7)
back-to-back γ -ray hits : energy cut	491.51(8)	491.56(5)
back-to-back γ -ray hits : time coincidence	457.44(8)	457.47(5)

Table 3.3: Summary of the event rates until offline trigger cut.

3.3.1 Signatures of the Transition Signal

The transition signals are the events that p-Ps ($\tau = 125$ ps) transitioned from o-Ps ($\tau = 142$ ns) decays into two back-to-back monochromatic (511 keV) γ rays. Therefore the transition signals have distinctive features as follows:

- long lifetime of o-Ps (142 ns)
- two back-to-back monochromatic 511 keV γ rays

In order to select such events, delayed coincidence and 511 keV energy selection are applied to the offline-triggered events. Detail will be discussed in Sec. 3.3.3 and 3.3.5.

3.3.2 Background

The background processes are as follows:

- pick-off annihilation of o-Ps
- 3γ decay of o-Ps
- accidental background

The pick-off annihilation of o-Ps is caused by a collision of o-Ps with the atomic electrons inside the target gas. It also occurs when the electron of the o-Ps exchanges its spin with electrons of the target materials. This conversion from o-Ps to p-Ps results in the rapid annihilation into two γ rays (spin-flip). This 2γ decay has the same kinematics as the transition signals and becomes background.

3γ decays of o-Ps make continuous energy spectrum and some of them become background because of the finite resolution of the γ -ray detectors. In addition, some of the 3γ decays are such events that two of the three γ rays are emitted in the same direction and the other γ ray is emitted in the opposite direction. This event mimics back-to-back 511 keV γ decay events.

The accidental background is dominant (about 2/3 of the total background) after the delayed coincidence and the 511 keV energy selection are applied. This background events removed as mentioned in Sec. 3.3.4. After accidental rejection, the remaining small accidental background estimated from the sideband in the Ps decay time distribution is subtracted.

Background estimation

Since the gyrotron output is pulse wave of duty 30 %, positroniums are not exposed to the radiation for 70 % of the operation period. The events during the “beam OFF” period are used to estimate background.

In order to avoid the uncertainty of normalization due to the pulse shape (width) and the other systematics by the offline trigger cuts, “beam OFF” events are normalized to “beam ON” events using the number of prompt decay events (time

window is set from -3.0 ns to 1.5 ns). About 80 % of the prompt decay events are due to the e^+ annihilation, therefore the uncertainty from the differences in Ps formation probability, transition probability, and pick-off probability is small.

3.3.3 Delayed Coincidence

Figure 3.9 shows the time difference between the plastic scintillator and the coincidence signal of the $\text{LaBr}_3(\text{Ce})$ scintillators. A sharp peak, called as the prompt peak, is observed at $t = 0$, where e^+ annihilations and p-Ps decays are dominant. The time region after the prompt peak is dominated by the o-Ps events and forms the exponential decay curve. The flat time spectrum far beyond the prompt peak is dominated by the accidental events. The γ -ray hit of the accidental event is not correlated with the e^+ hit.

Back-to-back 511 keV γ rays are mainly due to the prompt peak. Delayed coincidence is applied in order to improve S/N. The time window is set from 50 ns to 350 ns (Fig. 3.9). The event rates after the delayed coincidence is summarized in Table 3.4.

- $50 \text{ ns} < t < 350 \text{ ns}$,

where t is the time difference between the plastic scintillator and the coincidence signal of the $\text{LaBr}_3(\text{Ce})$ scintillators.

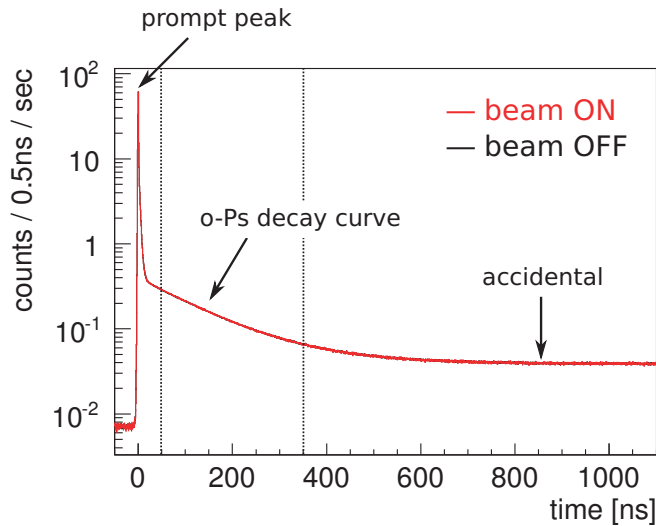


Figure 3.9: Time difference between the plastic scintillator and the coincidence signal of the $\text{LaBr}_3(\text{Ce})$ scintillators. Time window is set from 50 ns to 350 ns (black dash line). Note that this spectrum is a spectrum of the mean time of the two back-to-back $\text{LaBr}_3(\text{Ce})$ hits.

selection	rate (ON) [Hz]	rate (OFF) [Hz]
Delayed coincidence	67.933(29)	67.797(19)

Table 3.4: Event rates after the delayed coincidence.

3.3.4 Accidental Rejection

Even if delayed coincidence is applied, accidental events are dominant source of the back-to-back 511 keV γ rays. Accidental events are subtracted afterwards but subtraction of a lot of events spoils statistics. Thus, accidental rejection cut is applied before subtraction.

Figure 3.10 is time chart of the normal event (upper) and the accidental events (lower). In the case of the accidental events, there is another plastic scintillator hit at the timing of the γ -ray hit. As a result, the energy deposit on the plastic scintillator measured with long-gate becomes larger than that measured with short-gate.

The energy difference of the long-gate energy and the short-gate energy can be used to reject the accidental events. Figure 3.11 shows the energy difference between long-gate and short-gate of the ps-0 signal. Cut window is set from -2.5 p.e. to 1.7 p.e. and the cut is applied to both ps-0 and ps-1. Resolution of the zero peak is about 0.85 p.e.. The event rates after the accidental rejection are summarized in Table 3.5.

In order to show the efficiency of the accidental rejection, time spectrum before (black) and after (blue) accidental rejection are shown in Fig. 3.12. Accidental coincidence are suppressed and o-Ps decay curve is clearly enhanced.

selection	rate (ON) [Hz]	rate (OFF) [Hz]
Accidental rejection	29.116(19)	29.079(13)

Table 3.5: Events rate after the accidental rejection

3.3.5 γ -ray Energy Cut

Finally, the number of events such that back-to-back 511 keV γ -rays are observed are counted. Figure 3.13 is the energy spectrum when the delayed coincidence and the accidental rejection are applied and, in addition, a 511 keV γ -ray hit on the LaBr₃(Ce) scintillator at the opposite side is required (the energy window is set from 494 keV to 536 keV). The accidental events are only 4 % in time window after all selections are applied. Remaining accidental background estimated from the events in another time window (accidental window) set from 850 ns to 900 ns is subtracted.

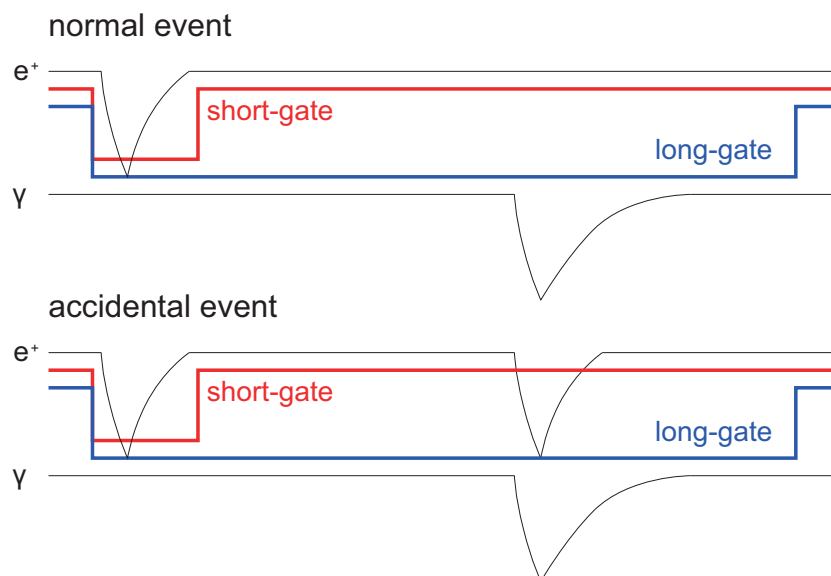


Figure 3.10: Time chart of the normal event (upper) and the accidental event (lower).

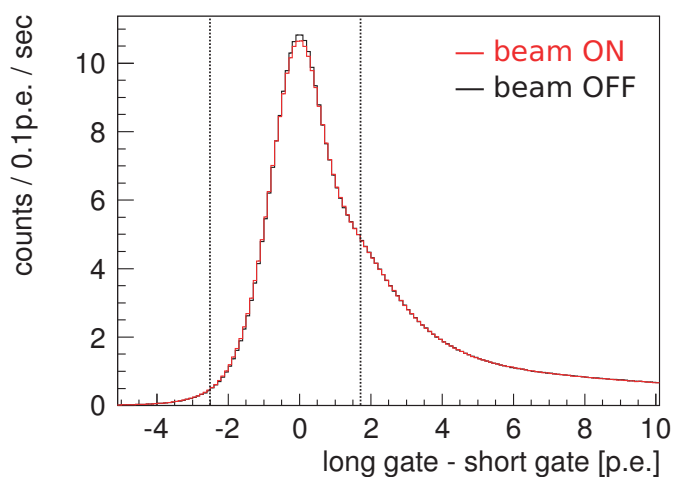


Figure 3.11: Energy difference between long-gate and short-gate of the ps-0 signal. The cut is shown in black dash line.

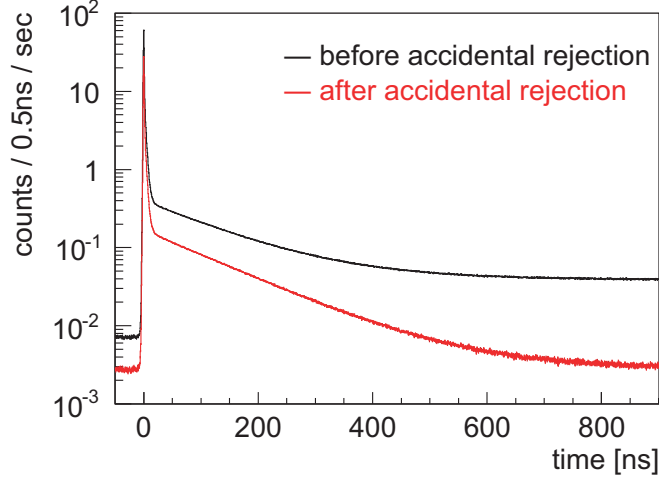


Figure 3.12: Time spectrum before (black) and after (blue) accidental rejection.

The signal region is from 494 keV to 536 keV and transition signals are clearly observed. The difference in rate between “beam ON” events and “beam OFF” events is

$$R_{\text{ON}} - R_{\text{OFF}} = 303.7(2.3) \text{ [mHz]} - 288.6(1.5) \text{ [mHz]} = 15.1 \pm 2.7(\text{stat.}) \text{ [mHz]} \quad (3.1)$$

3.4 Systematic Errors

In this section, the systematic errors are discussed. They are put into several categories according to their origins.

3.4.1 Energy Scale and Energy Resolution

If the energy scales and the energy resolutions are different between “beam ON” events and “beam OFF” events, fake signals appear. In order to estimate the uncertainties, the 511 keV peak of “beam ON” events and “beam OFF” events after the energy calibration are fitted again with Gaussian function. The positions and the resolutions of the peaks are summarized in Table 3.6. The width includes pedestal uncertainty. These values are put into the Monte Carlo simulation, and the difference of the number of events in the signal region without power is found to be +0.08 %, thus the systematic error for the transition signal is -0.08 % of the background.

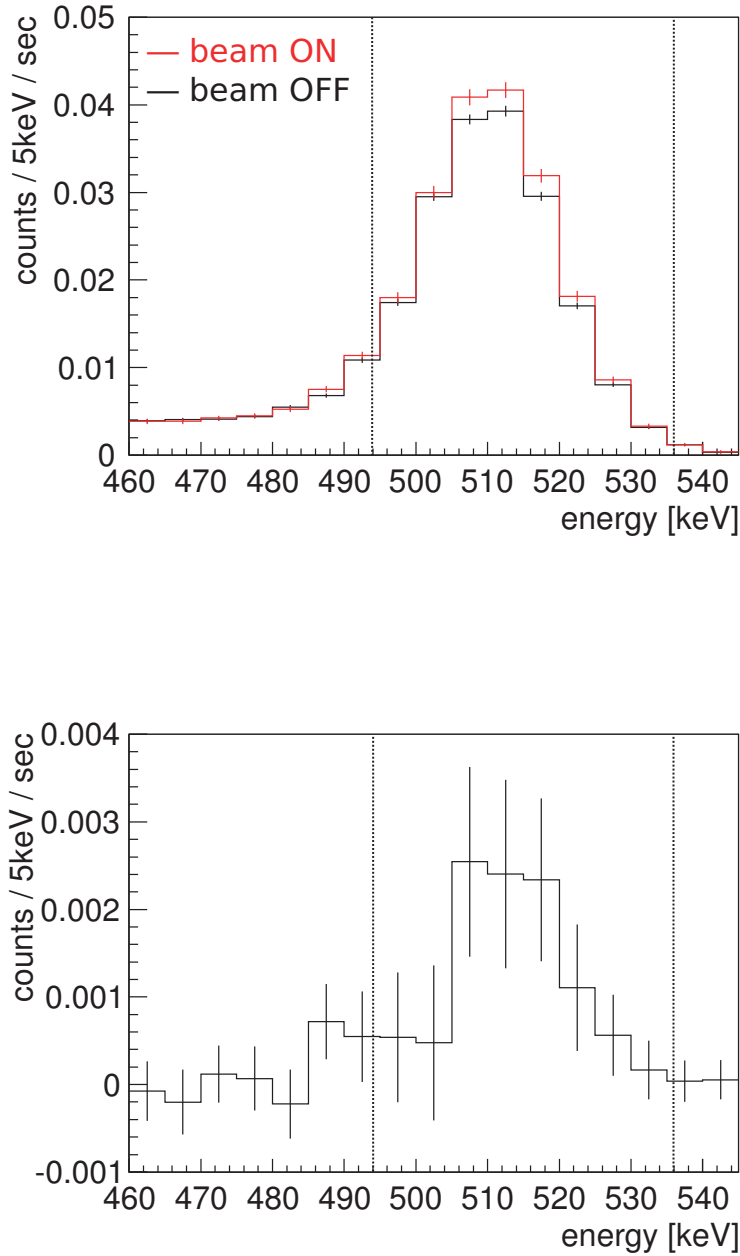


Figure 3.13: Energy spectrum of on-resonance data (RUN I) when the delayed coincidence and the accidental rejection are applied and a 511 keV γ ray is observed (energy window is set from 494 keV to 536 keV) at the opposite side of the LaBr₃(Ce) scintillator. Accidental background estimated from the events in the time window set from 850 ns to 900 ns is subtracted. (top) ON (red line), OFF (black line), (bottom) ON - OFF

LaBr ₃ (Ce)	E_{511}^{off} [keV]	$\sigma_{511}^{\text{off}}$ [keV]	E_{511}^{on} [keV]	σ_{511}^{on} [keV]
0	511.047(6)	7.994(8)	511.072(10)	7.951(12)
1	511.049(6)	8.084(8)	511.050(10)	8.074(12)
2	511.136(9)	9.052(12)	511.153(14)	9.016(18)
3	511.085(7)	8.291(9)	511.089(11)	8.275(13)

Table 3.6: The positions and the widths of the 511 keV peaks of “beam ON” events and “beam OFF” events.

3.4.2 Ps Formation Probability and Pick-off Annihilation Probability

Ps formation probabilities of the “beam ON” and the “beam OFF” data are different when sub-THz radiation resonant with the Fabry-Pérot cavity. Figure 3.14 is the magnified view of the time spectrum of “beam ON” – “beam OFF” just after the offline trigger cut. Except for the no power data (RUN III), the slow positron annihilation rate of “beam ON” data is smaller than that of “beam OFF” data. Since we adopt the delayed coincidence, the difference of the slow positron annihilation rates does not contribute to the systematic error, but it means that the Ps formation probability of “beam ON” data is larger than that of “beam OFF” data, because the slow positron is the positron which is not able to form positronium. Difference of the Ps formation probability is a source of systematic error.

Actually, the difference of the Ps formation probability is estimated by counting the number of events in the time window (accidental events are subtracted) before energy cut is applied and is found to be +0.27 % in RUN I. Since the Ps formation probability is not dependent on the γ -ray energy cut, the systematic error is found to be -0.27 %. The reason of the difference of the Ps formation probability is not sure, but the amount of the difference correlates with the temperature of the gas filled in the chamber, as shown in Fig. 3.15. The difference of the Ps formation probability is the largest in RUN II, which is off-resonance RUN using 140 GHz radiation, because the gas temperature of RUN II is also the highest among the four RUNs. In other words, we can conclude that if no excess is observed in RUN II, the uncertainty of the Ps formation probability is not crucial to this experiment.

3.4.3 Accidental Rejection Efficiency

The accidental rejection cut also rejects the signal events to some extent. The efficiency of the accidental rejection depends on the rates of the plastic scintillator signals which go over the discriminator threshold (~ 1 p.e.). If the “beam ON” rate is smaller than the “beam OFF” rate, less events are rejected. In order to estimate this systematic effect, the accidental rejection cut efficiency is checked and the difference between “beam ON” events and “beam OFF” events is -0.17 %, which is not dependent on the γ -ray energy cut, thus the systematic error is

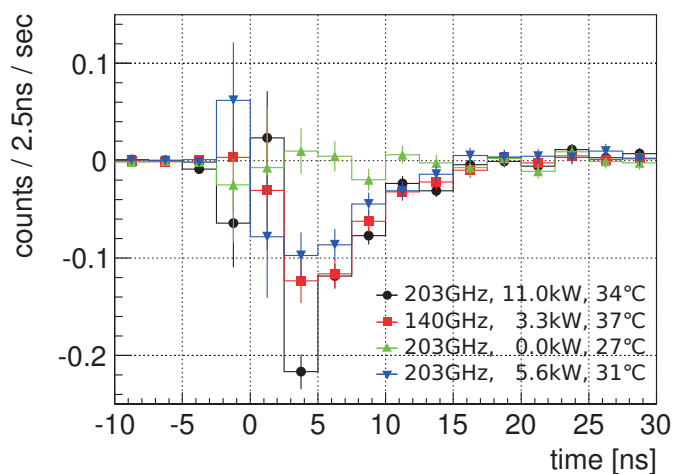


Figure 3.14: The difference of the slow positron annihilation rate.

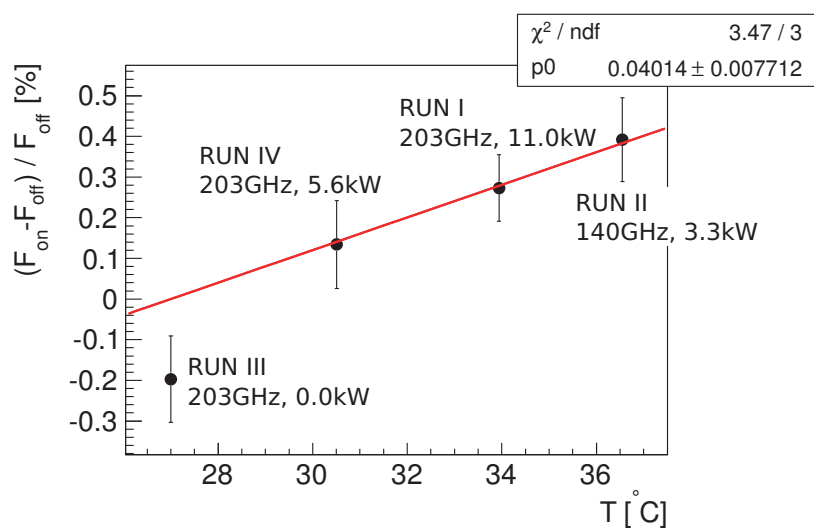


Figure 3.15: The difference of the Ps formation probabilities. It correlates with the temperature in the gas chamber. The fitting function (red line) is $p_0(T - 27)$.

found to be +0.17 %.

3.4.4 Background Normalization

The background is estimated from the “beam OFF” events and its normalization is performed using the number of events in the prompt time window (from -3 ns to 1.5 ns), where the usual e^+ annihilation is 77 %, the decay of p-Ps is 14 %, and the slow positron annihilation is 8 %. Since the fraction of the p-Ps events is larger than that of the slow positron events, this normalization is conservative about the Ps formation probability. These events are statistically independent of the events in the signal region. The uncertainty of the background normalization can be estimated from the statistical error of the normalization factor, which is only ± 0.03 %.

3.4.5 Summary of the Systematic Errors

Above systematic errors are summarized in Table 3.7. The total systematic error is calculated as a quadrature sum of them since they are considered to be independent with each other. The values are percentage of the rate of “beam OFF” events.

source	RUN I	RUN II	RUN III	RUN IV
Energy scale and resolution	-0.08 %	$+0.06$ %	-0.11 %	-0.02 %
Ps formation probability	-0.27 %	-0.39 %	$+0.20$ %	-0.13 %
Accidental rejection efficiency	$+0.17$ %	$+0.05$ %	$+0.13$ %	$+0.23$ %
Background normalization	± 0.03 %	± 0.04 %	± 0.04 %	± 0.04 %
Total	$+0.17$ % -0.29 %	$+0.08$ % -0.39 %	$+0.24$ % -0.12 %	$+0.24$ % -0.14 %

Table 3.7: Summary of the systematic errors. The values are percentage of the rate of “beam OFF” events.

3.5 Result

From the analysis in this chapter, the following result is obtained for RUN I (202.89 GHz, 11.0 kW).

$$\text{ON} - \text{OFF} \tag{3.2}$$

$$= 303.7 \pm 2.3 \text{ (stat.) } \begin{matrix} +0.5 \\ -0.8 \end{matrix} \text{ (sys.)} - 288.6 \pm 1.5 \text{ (stat.)} \pm 0.1 \text{ (sys.)} \tag{3.3}$$

$$= 15.1 \pm 2.7 \text{ (stat.) } \begin{matrix} +0.5 \\ -0.8 \end{matrix} \text{ (sys.) [mHz]} \tag{3.4}$$

where the first error represents a statistical error and the second one is for systematic. The significance of the transition signal is 5.4σ .

The results of four RUNs are summarized in Table 3.8 and the power dependence of on-resonance data is shown in Fig. 3.16. The amount of the transition is proportional to the accumulated power and the off-resonance data (RUN II) gave a null result though the systematic uncertainty of the Ps formation probability is the largest among the four RUNs.

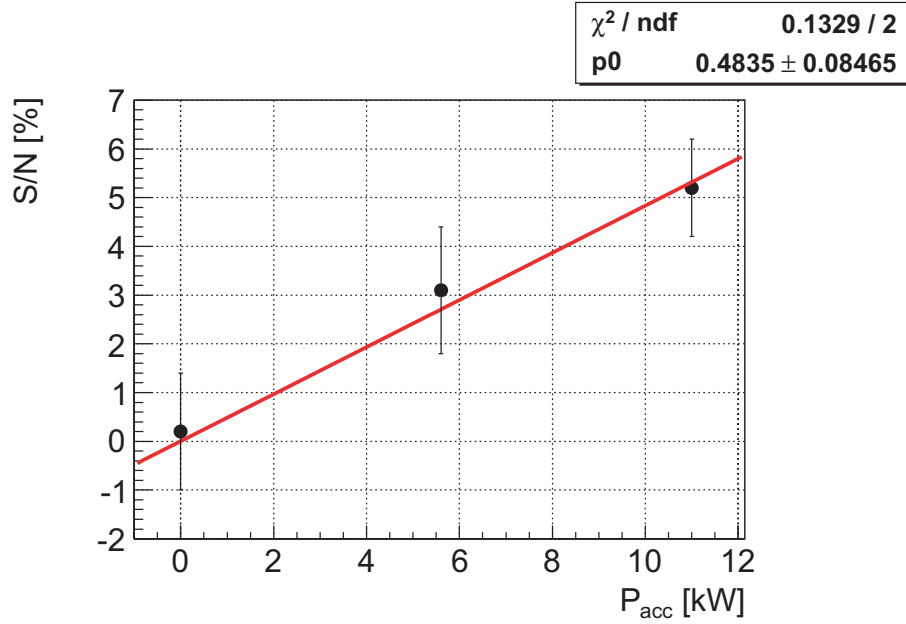


Figure 3.16: The fraction of the transition signals is proportional to the accumulated power in the Fabry-Pérot resonant cavity.

ID	frequency	power	pressure	temperature	S/N
I	203 GHz	11.0 kW	2.011 atm	33.94 °C	5.2 ± 1.0 %
II	140 GHz	3.3 kW	2.015 atm	36.55 °C	1.0 ± 1.2 %
III	203 GHz	0.0 kW	2.003 atm	27.00 °C	0.2 ± 1.2 %
IV	203 GHz	5.6 kW	2.008 atm	30.51 °C	3.1 ± 1.3 %

Table 3.8: Results of the four RUNs.

Chapter 4

Discussion

4.1 Various Checks

The several cuts are applied to reject the accidental events and the 3γ decay events. The measured signal to noise ratio must be independent of the cut condition of the accidental rejection. On the other hand, it must depend on the energy selection. To make sure of these relationship, the cut conditions are varied to some extent.

In addition, lifetime of the transition signal is checked for confirmation of the result.

4.1.1 Accidental Rejection

The default cut window of the accidental rejection is from -2.5 p.e. to 1.7 p.e., which corresponds to from -3σ to $+2\sigma$. The upper limit determines the rejection power (c.f. Fig. 3.10) and therefore we set the more strict upper limit than the lower limit. The upper limit is varied to check if the S/N (after remaining accidental events are subtracted) is independent of it. The result is summarized in Table 4.1. The deviation of the S/N can be explained by the statistical fluctuation (0.7σ , -0.6σ).

upper limit	default	tight	loose
	1.7 p.e. ($= +2\sigma$)	1.4 p.e. ($= +1.64\sigma$)	2.5 p.e. ($= +3\sigma$)
S/N	$5.24 \pm 0.96(\text{stat.}) \%$	$5.38 \pm 0.98(\text{stat.})$	$5.43 \pm 0.91(\text{stat.})$

Table 4.1: Check dependency on the upper limit of the accidental rejection cut.

4.1.2 Energy Selection

The default energy window for the 511 keV peak is from 494 keV to 536 keV, which corresponds to from -2σ to $+3\sigma$. The lower limit determines the $2\gamma/3\gamma$

ratio, therefore the S/N depends on the energy window. The lower limit is varied to check if the S/N depends on it and the dependency is consistent to the Monte Carlo (MC) expectation. The result is summarized in Table 4.2. The dependence on the lower limit of the energy selection is observed and the dependency is consistent to the MC expectation. The input parameters of the MC simulation is the same as those determined in the next section.

upper limit	default 494 keV ($= -2\sigma$)	tight 497 keV ($= -1.64\sigma$)	loose 486 keV ($= -3\sigma$)
S/N	$5.24 \pm 0.96(\text{stat.}) \%$	$5.43 \pm 0.99(\text{stat.}) \%$	$4.82 \pm 0.86(\text{stat.}) \%$
S/N (MC)	5.37 %	5.76 %	4.81 %

Table 4.2: Check dependency on the lower limit of the energy selection.

4.1.3 Time Spectrum of the Transition Signal

Figure 4.1 is the time spectrum of the transition signal, that is the difference between the time spectrum of the “beam ON” events and that of the “beam OFF” events after the accidental rejection and the back-to-back 511 keV cut. The time spectrum is fitted with exponential function and the lifetime is obtained to be 133 ± 34 ns, which is consistent with the lifetime of o-Ps. The reduced χ^2 of the fit is 0.89 and the probability is 64 %. That is, the transition signals are properly distributed as expected.

4.2 Comparison with QED Calculation

The energy spectra of the most high power on-resonance data (RUN I) is fitted with MC spectra to estimate Einstein’s A coefficient of the hyperfine transition of positronium and compare it with QED calculation ($A = 3.37 \times 10^{-8} [\text{s}^{-1}]$).

If we set the beam intensity distribution which can be calculated from the accumulated power P_{acc} during DAQ and the beam shape inside the Fabry-Pérot resonant cavity, parameters of the MC spectra are normalization factor C , the Einstein’s A coefficient A , and the probability of the pick-off annihilation P_{pick} . The MC spectra are expressed as follows :

$$S_{\text{OFF}} = C[f_{3\gamma}(0, P_{\text{pick}}, A)S_{3\gamma} + f_{\text{pick}}(0, P_{\text{pick}}, A)S_{2\gamma}] \quad (4.1)$$

$$S_{\text{ON}} = C\{f_{3\gamma}(I, P_{\text{pick}}, A)S_{3\gamma} + [f_{\text{pick}}(I, P_{\text{pick}}, A) + f_{\text{trans}}(I, P_{\text{pick}}, A)]S_{2\gamma}\} \quad (4.2)$$

where $f_{3\gamma}(I, P_{\text{pick}}, A)$, $f_{\text{pick}}(I, P_{\text{pick}}, A)$, and $f_{\text{trans}}(I, P_{\text{pick}}, A)$ can be calculated from the solution of the rate equation for the hyperfine transition of the ground state of Ps (Eq. (1.18)).

The “beam ON” spectrum and the “beam OFF” spectrum are fitted at the same time as shown in Fig. 4.2. The fit range is from 460 keV to 545 keV and

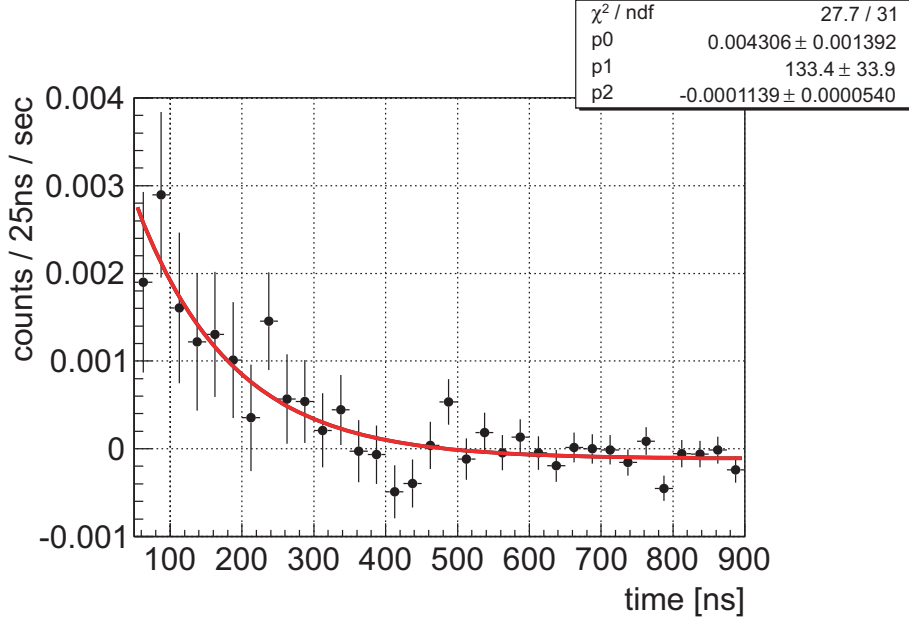


Figure 4.1: Fitted time spectrum of the transition signals.

the best fit parameters are $P_{\text{pick}} = 5.45(22) \%$ and $A = 3.07(93) \times 10^{-8} \text{ s}^{-1}$ when $P_{\text{acc}} = 11.0 \text{ [kW]}$ ($I = 8.3 \times 10^7 \text{ W/m}^2$, $\epsilon = 0.28 \text{ J/m}^3$) is put as the accumulated power. The reduced χ^2 is 0.91 and the probability is 77 %. In order to estimate the systematic error of A due to the uncertainty of the absolute power estimation, we change P_{acc} within its error and check how much A changes. Finally, the Einstein's A coefficient is estimated to be

$$A = (3.1_{-1.2}^{+1.6}) \times 10^{-8} \text{ [s}^{-1}\text{]}, \quad (4.3)$$

which is consistent with the QED calculation $3.37 \times 10^{-8} \text{ s}^{-1}$.

Note that P_{pick} is also consistent with the pick-off probability estimated by fitting the time spectrum after the accidental rejection and the back-to-back 511 keV cut are applied. From Fig. 4.3, the o-Ps decay rate of data is $7.417(52) \mu\text{s}$ (fitting start time = 50 ns), thus $P_{\text{pick}} = 5.35(73) \%$.

4.3 Future Prospect

We are planning to measure the Ps-HFS directly for the first time by the end of 2012. In order to measure the Ps-HFS, we have to measure the shape of the resonance curve, whose center value is the Ps-HFS. Therefore we have to perform the measurement of the hyperfine transition while changing the radiation frequency. We plan to measure five points over a frequency range from 201 GHz to 205 GHz.

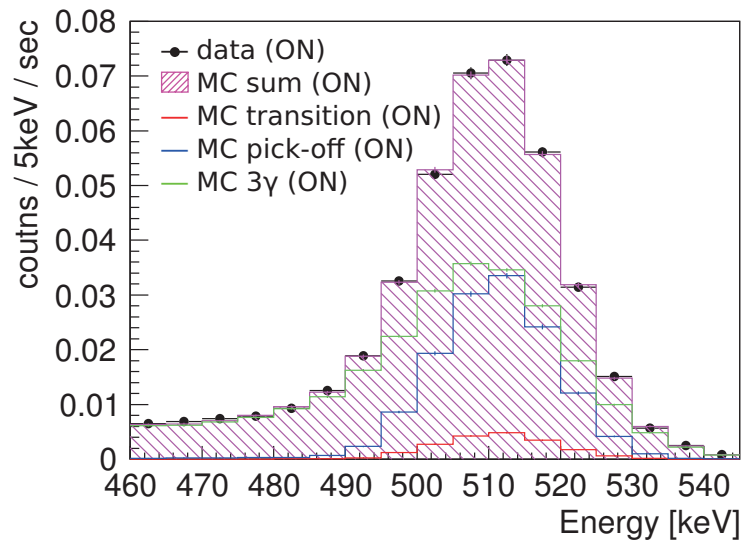
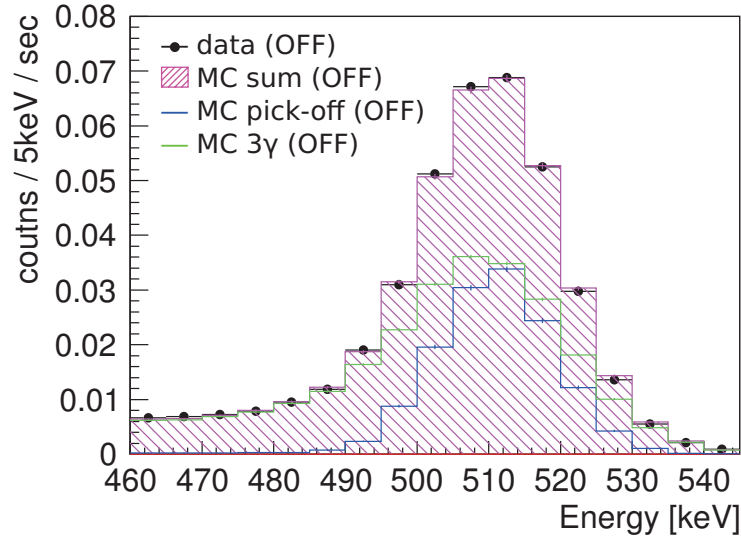


Figure 4.2: The fraction of the transition signals is consistent with QED calculation. The top figure shows the “beam OFF” spectrum and the bottom figure shows the “beam ON” spectrum (RUN I).

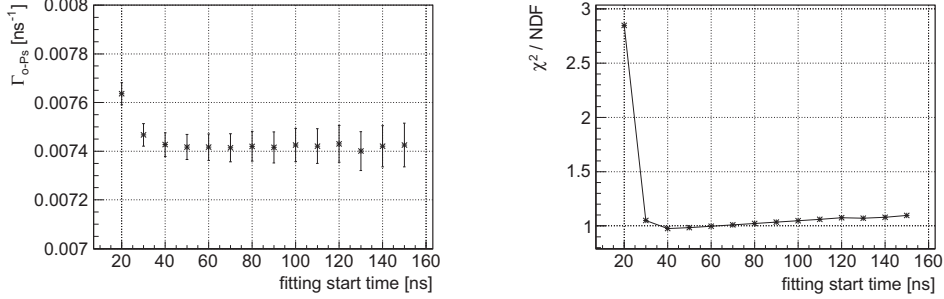


Figure 4.3: Fitted decay rate (RUN I). The fitted decay rate is plotted along the fitting start time in the left figure. The reduced χ^2 along the fitting start time is also shown in the right figure. The accidental rejection and the 511 keV back-to-back selection are performed on the time spectrum used in this fitting.

The output frequency of gyrotron is determined by its cavity size, therefore now we are developing a new gyrotron whose cavity can be quickly replacable while keeping vacuum of the gyrotron.

In addition, the transition measurement is expected to improve. There are two problems in the current optical system. One problem is that the mesh pattern melts when the accumulated power exceeds about 15 kW. Figure 4.4 is a picture of a melted mesh mirror. This is due to local elevation of temperature, but it is difficult to cool mesh with water since the mesh pattern is formed on a SiO_2 substrate, whose heat conductivity is small ($\sim 1.4 \text{ W/m}\cdot\text{K}$). The other problem is the reflection from the Fabry-Pérot resonant cavity. The reflection goes back to the gyrotron and interferes with the oscillation in the gyrotron. The interference makes power estimation difficult and the rapid decrease of reflection when the Fabry-Pérot cavity resonates causes rapid change in the input beam power as shown in Fig. 4.5, which leads to destabilization.

In order to solve these two problems, we plan to replace the Fabry-Pérot cavity with a grating ring cavity. Figure 4.6 is a schematic of a ring cavity. The grating made of Cu corresponds to the Au mesh mirror of the Fabry-Pèrot cavity. The 1st reflection of the grating enters the ring cavity and makes many round-trips in the ring cavity when the ring cavity resonates. The direction of the reflection from the cavity is the same as that of the 0th reflection of the input beam, therefore no beam goes back to the gyrotron. In addition, the grating is easy to chill since it is made of Cu only.

Next, let us estimate the accuracy of the Ps-HFS measurement in 2012. From the result of the transition measurement, we can measure a point at 202.89 GHz with an accuracy of 20 % with 4 days of DAQ. Figure 4.7 is a transition curve assuming $I = 10^8 \text{ [W/m}^2\text{]}$. The transition probability at 202.89 GHz is 75 % of that at the peak of the transition curve, therefore we can measure a point at the

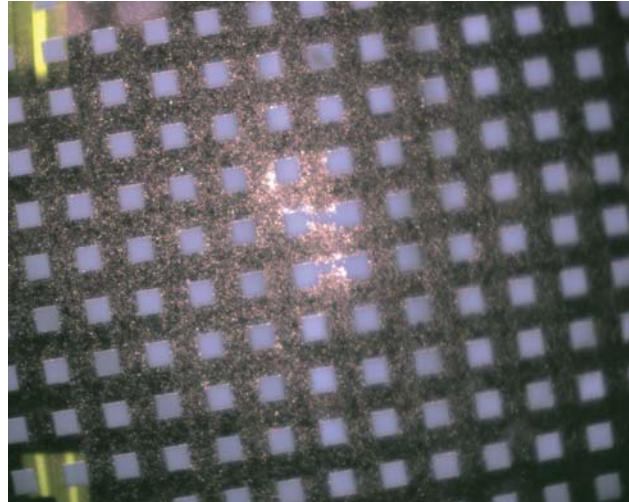


Figure 4.4: A picture of a melted mesh mirror.

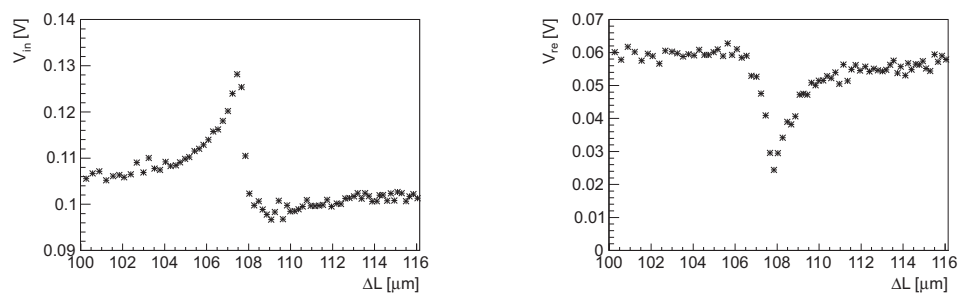


Figure 4.5: Interference between input power and reflected power around resonance peak. The left figure shows input power while changing the cavity length and the right figure is reflected power.

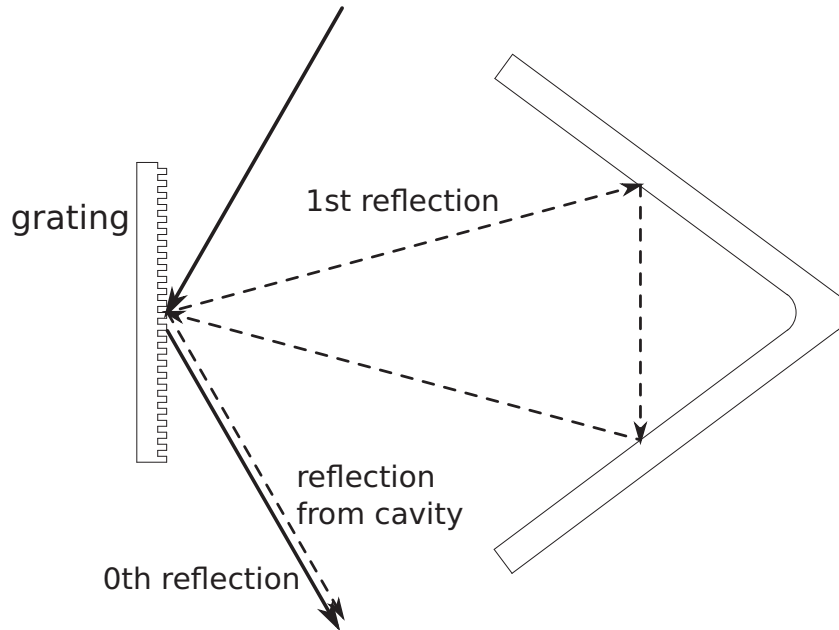


Figure 4.6: A schematic of a grating ring cavity.

peak with 10 % accuracy with 5 days of DAQ. Two points at the half maximum can be measured with an accuracy of 10 % with 20 days of DAQ. Therefore, if we can measure the accumulated power to an accuracy of about 10 % relatively, the Ps-HFS can be determined with an accuracy of about 400 ppm (Fig. 4.8). As for the power estimation, the absolute power estimation is quite difficult as described in this thesis, but what we have to measure in the Ps-HFS measurement is the relative power accumulated in the cavity resonator. One idea of the relative power measurement is that the position of the hole is displaced from the center of the mirror and the hole size is made larger than the half of the wavelength. Then the transmittance of the hole becomes independent of the wavelength, and determined only on the beam size at the Cu mirror, which depends on the wavelength. For example, if we knock four holes per 90 degrees at 10 mm from the center, the fluctuation of the transmittance is smaller than $\pm 5\%$ since the beam size varies only from 11.28 mm to 11.37 mm within the frequency range of 201.5 GHz - 205.0 GHz. Stability of accumulated power is also necessary. Introduction of a grating ring cavity is expected to improve the stability of the gyrotron output power, but we also have to optimize parameters of the feedback control. In addition, we have to chill the gas chamber in order to stabilize the resonance of the Fabry-Pérot cavity.

Finally, we address the precise measurement of the Ps-HFS of $O(\text{ppm})$ level. There are many challenges to the precise measurement of the Ps-HFS with the direct transition method. Of course, we have to improve the relative accuracy of the power estimation to $O(0.1\%)$, which needs further study. Besides, we have to

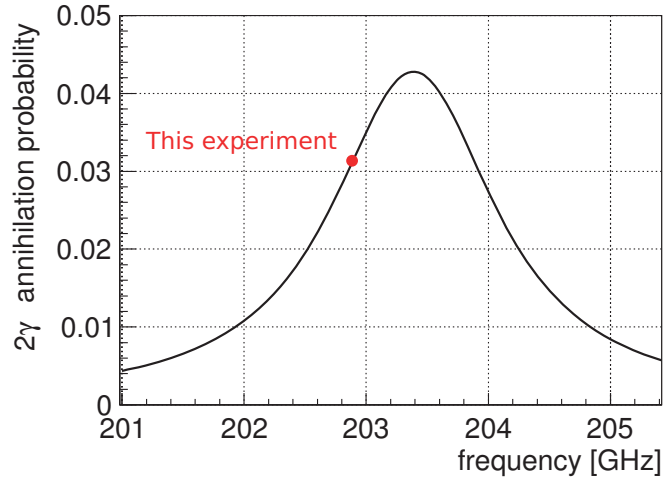


Figure 4.7: Transition curve assuming $I = 10^8 \text{ W/m}^2$. The measurement of the red point is described in this thesis.

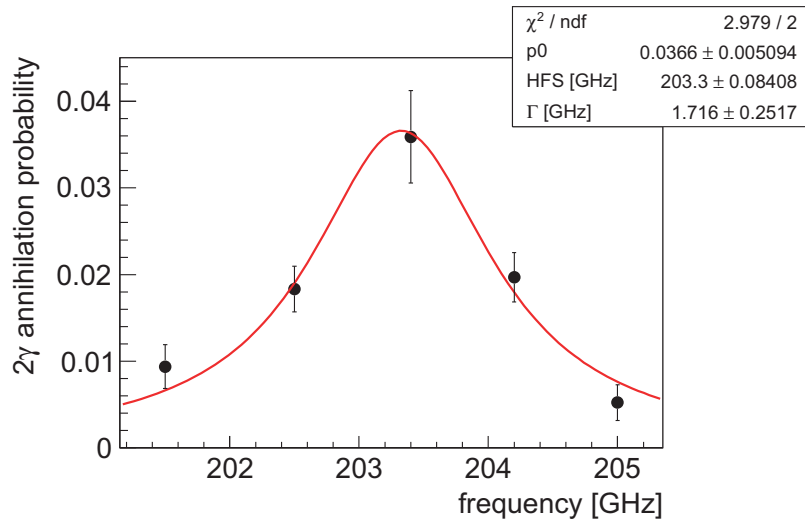


Figure 4.8: Simulation of Ps-HFS measurement assuming statistical accuracy of 10 % and power accuracy of 10 %.

improve statistics and reduce systematic errors of the transition measurement. The error of the transition measurement should be also $O(0.1\%)$. We plan to use the slow positron beam and make positroniums in vacuum using a thin metal foil to achieve this accuracy. Figure 4.9 is a schematic of the setup. The slow positron (~ 1 keV) are injected onto a metal foil [31]. Some of the positrons lose their energies in the foil, diffuse back to the surface, and are emitted as Ps. The kinetic energy of Ps is about 1 eV, then only o-Ps can reach the sub-THz radiation region since the lifetime of o-Ps (142 ns) is 1000 times longer than that of p-Ps (125 ps). The γ rays from p-Ps and e^+ annihilation are shielded by Pb shielding. In addition, the pick-off background also vanishes since the Ps are formed in vacuum. As a result, the energy spectrum of the γ -ray detectors becomes transition signals + 3γ backgrounds only except for few pileup events of the γ -ray detectors. Therefore S/N is expected to be improved as well as the statistics thanks to the high intensity of the positron beam. Besides, there is no absorption of the sub-THz radiation, therefore the main systematic error of the current transition measurement vanishes and, of course, no loss of the beam power in the gas is an improvement itself.

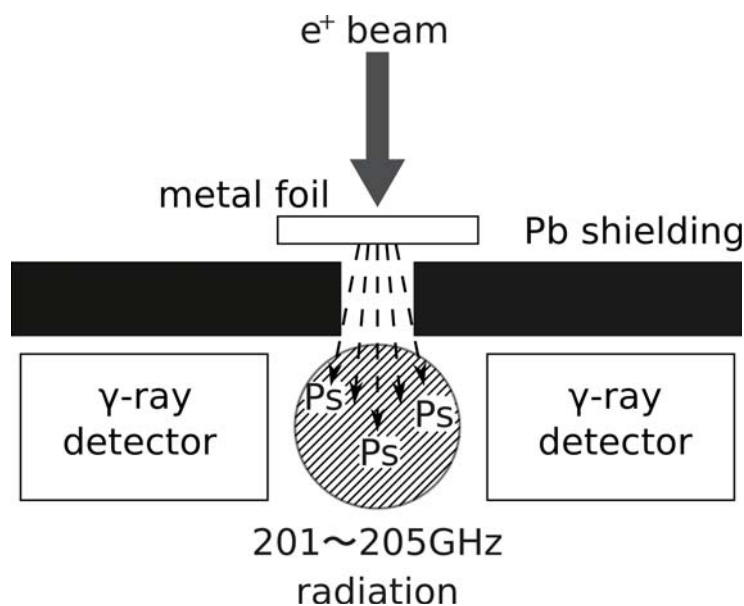


Figure 4.9: A schematic of an experimental setup with a slow positron beam.

Chapter 5

Conclusion

The hyperfine transition of the ground state of positronium has been observed for the first time using high power sub-THz radiation. It is M1 transition between the hyperfine structure of the ground state of positronium (Ps-HFS), which is the energy splitting between the ground state ortho-positronium (o-Ps) and the ground state para-positronium (p-Ps) due to the spin-spin interaction. The Ps-HFS is significantly large (about 203 GHz). Extremely high power sub-THz radiation is necessary to cause observable amount of stimulated emission between the Ps-HFS, since the rate of the spontaneous emission between the Ps-HFS is 14 orders of magnitude smaller than the decay rate of o-Ps. We develop a new optical system which consists of a gyrotron, which is a novel high power radiation source for sub-THz to THz region, a mode converter, and a Fabry-Pérot resonant cavity, in order to accumulate sub-THz radiation of 11 kW (peak intensity $I = 8.3 \times 10^7$ W/m², peak energy density $\epsilon = 0.28$ J/m³) in the Fabry-Pérot cavity. Positroniums are formed in gas and the high power radiation in the Fabry-Pérot cavity causes the hyperfine transition of the ground state of positronium. We have observed clear transition signal, which is observed as the increase of 2γ decay of positronium detected by surrounding γ -ray detectors. The significance of the transition signal is 5.4σ and the amount of the transition signal is consistent with the QED calculation. We have also performed off- and half-power measurements. The amount of the transition signal is proportional to the accumulated power. In addition, there is no excess in off-resonance measurement. As a result, we conclude that we have observed the hyperfine transition of the ground state of positronium.

This measurement is also a great step toward the direct measurement of the Ps-HFS. Precise measurements of the Ps-HFS give the direct information on the bound state Quantum Electrodynamics (QED) and have been performed in 1970's and 1980's, but all of them are indirect measurement using Zeeman splitting caused by static magnetic field. The most significant common systematic uncertainty of the previous measurements is non-uniformity of the static magnetic field, and there is a large discrepancy (3.9σ , 15 ppm) between the measured and the theoretical value of the Ps-HFS. It is necessary to measure the Ps-HFS again with a different

method free from the uncertainty of static magnetic field. We plan to perform the first direct measurement of the Ps-HFS with an accuracy of $O(100 \text{ ppm})$ by the end of 2012. A new gyrotron whose cavity can be quickly replacable is under development since the radiation frequency is determined by the size of the cavity of gyrotron. In the future, we plan to measure the Ps-HFS precisely with an accuracy of $O(\text{ppm})$ by using a slow positron beam and creating positroniums in vacuum.

Acknowledgements

First, I would like to express my gratitude to my supervisor Prof. Tomio Kobayashi (ICEPP, Univ. of Tokyo) for providing me with this work and his continuous encouragement and supports.

I also wish to express my great appreciation to Prof. Shoji Asai (Univ. of Tokyo) for his continuous assistance and guidance at this work.

My special thanks goes to Prof. Toshio Namba (ICEPP, Univ. of Tokyo) for guiding the work in the right direction with his experience.

Of course I did not perform all the work in this thesis alone and, in fact, a lot of it would not have been possible without the support of many other people. First I would like to thank Dr. Taikan Suehara (ICEPP, Univ. of Tokyo) who have been playing a leading role in this experiment from the scratch. Special thanks also goes to Akira Miyazaki (Univ. of Tokyo) for his excellent cooperation.

The work presented in this thesis is a collaboration study with Research Center for Development of Far-Infrared Region, University of Fukui (FIR-FU). Here I would like to express my gratitude to Prof. Toshitaka Idehara for developing the great radiation source Gyrotron FU CW V and for his support during the experiment at FIR-FU. I also wish to express my great appreciation to Prof. Isamu Ogawa for many useful discussions and advises on the development of the mode converter. Special thanks also goes to Prof. Svilen Sabchevski for his great suggestion about our experimental setup.

At this point, I would like to thank all the staffs and students of International Center for Elementary Particle Physics (ICEPP) at University of Tokyo,

Last but not least, I would like to thank my family for supporting my decision to study physics and their constant encouragement.

Bibliography

- [1] A. P. Mills, Phys. Rev. A **27**, 262 (1983).
- [2] M. W. Ritter et al., Phys. Rev. A **30**, 1331 (1984).
- [3] B. A. Kniel and A. A. Penin, Phys. Rev. Lett. **85**, 5094 (2000).
- [4] Y. Kataoka, S. Asai, and T. Kobayashi, Phys. Lett. B **671**, 219 (2009).
- [5] A. H. Al-Ramadhan and D. W. Gidley, Phys. Rev. Lett. **72**, 1632 (1994).
- [6] A. Ishida et al., arXiv:1004.5555 (2010).
- [7] A. Ishida et al., arXiv:1105.4392 (2011).
- [8] A. Schäfer, J. Reinhardt, W. Greiner, and B. Müller, Mod. Phys. Lett. A **1**, 1 (1986).
- [9] S. Asai, S. Orito, K. Yoshimura, and T. Haga, Phys. Rev. Lett. **66**, 2440 (1991).
- [10] H. M. Chang et al., Phys. Rev. D **75**, 052004 (2007).
- [11] A. Konaka et al., Phys. Rev. Lett. **57**, 659 (1986).
- [12] J. D. Bjorken et al., Phys. Rev. D **38**, 3375 (1988).
- [13] A. Bross et al., Phys. Rev. Lett. **67**, 2942 (1991).
- [14] D. Hanneke, S. Fogwell, and G. Gabrielse, Phys. Rev. Lett. **100**, 120801 (2008).
- [15] R. Bouchendira et al., Phys. Rev. Lett. **106**, 080801 (2011).
- [16] J. Reinhardt et al., Phys. Rev. C **33**, 194 (1986).
- [17] J. D. Jackson, *Classical Electrodynamics*, John Wiley & Sons, Inc., third edition, 2001.
- [18] R. Piesiewicz et al., Int J Infrared Milli Waves **28**, 363 (2007).

- [19] O. Wada, Ph.D. thesis, University of Kyoto, 1987.
- [20] Brand et al., *Int. J. Electron* **68**, 1063 (1990).
- [21] C. Winnewisser, F. Lewen, and H. Helm, *Appl. Phys. A* **66**, 593 (1998).
- [22] R. C. Jaeger, *Introduction to Microelectric Fabrication*, Prentice Hall, second edition, 2001.
- [23] T. Weiland, *Electron. Commun. (AEÜ)* **31**, 308 (1977).
- [24] M. Clemens and T. Weiland, *Prog. Electromagn. Res.* **32**, 65 (2001).
- [25] J. Dai, J. Zhang, W. Zhang, and D. Grischkowsky, *J. Opt. Soc. Am. B* **21**, 1379 (2004).
- [26] M. Charlton, *Rep. Prog. Phys.* **48**, 737 (1985).
- [27] K. Iwata et al., *Phys. Rev. A* **51**, 473 (1995).
- [28] D. A. L. Paul and L. Saint-Pierre, *Phys. Rev. Lett.* **11**, 493 (1963).
- [29] A. Agostinelli et al., *Nucl. Instrum. Meth. A* **506**, 250 (2003).
- [30] G. S. Adkins, R. N. Fell, and J. Sapirstein, *Ann. Phys. (N.Y.)* **295**, 136 (2002).
- [31] P. J. Schultz and K. G. Lynn, *Rev. Mod. Phys.* **60**, 701 (1988).